COMPUTATIONAL STUDY OF CATALYZED GROWTH OF SINGLE WALL CARBON NANOTUBES

A Dissertation

by

JIN ZHAO

Submitted to the Office of Graduate Studies of
Texas A&M University
in partial fulfillment of the requirements for the degree of

DOCTOR OF PHILOSOPHY

December 2008

Major Subject: Chemical Engineering

COMPUTATIONAL STUDY OF CATALYZED GROWTH OF SINGLE WALL CARBON NANOTUBES

A Dissertation

by

JIN ZHAO

Submitted to the Office of Graduate Studies of
Texas A&M University
in partial fulfillment of the requirements for the degree of

DOCTOR OF PHILOSOPHY

Approved by:

Chair of Committee,	Perla B. Balbuena
Committee Members,	James Batteas
	Jorge Seminario
	Daniel Shantz
Head of Department,	Michael Pishko

December 2008

Major Subject: Chemical Engineering

ABSTRACT

Computational Study of Catalyzed Growth of Single Wall Carbon

Nanotubes. (December 2008)

Jin Zhao, B.S., Tianjin University, Tianjin, China;

M.S., Tianjin University, Tianjin, China

Chair of Advisory Committee: Dr. Perla B. Balbuena

A recently developed chemical vapor deposition (CVD) synthesis process called CoMoCAT yields single-wall carbon nanotubes (SWCNT)s of controlled diameter and chirality, making them extremely attractive for technological applications. In this dissertation, we use molecular dynamics simulations and density functional theory to study the selective growth mechanisms.

In the CoMoCAT process, growth of SWCNTs happens on Co clusters with diameters of about 1 Å. Effective force fields for Ni-C interactions developed by Yamaguchi and Maruyama for the formation of metallofullerenes and the reactive empirical bond order Brenner potential for C-C interactions are modified to describe interactions in such system. Classical molecular dynamics (MD) simulations using this force field are carried out to study the growth of SWCNT on floating and supported metal clusters. The effect of metal-cluster interactions on the growth process is discussed.

The energy of forming one more ring at the open end of one-end-closed nanotubes with different chiralities, which is believed to be the basic step of nanotube elongation, are studied as a function of tube length. The energy and shape of the frontier highest occupied molecular orbital (HOMO) and lowest unoccupied molecular orbital (LUMO) of armchair nanotubes are studied and used to explain the change of reaction energy with tube length.

Another property, the aromaticity of the rings forming a tube is also studied using Nucleus Independent Chemical Shift (NICS) as probe. NICS of rings in one-end-closed nanotubes with different chirality are studied as a function of tube length. NICS behavior of one-end-closed nanotube is compared with that of two-ends-open nanotube with the same chirality for nanotubes (6, 5) and (9, 1). Also (8, 3) nanotubes with one end open and the other end bonded to three different kinds of cap structures are compared.

Since from both experimental observation and from our MD simulation results, the growth process of SWCNT can be affected by the interaction between Co clusters and their substrate, the performance of a series of Co_N Clusters (N=1-4, 7, 10, 14, 15) adsorbed on MoC surface are studied with density functional theory.

ACKNOWLEDGEMENTS

I would like to express my sincere gratitude to my advisor, Dr. Perla B. Balbuena. It has been my good fortune to have the opportunity to work with Dr. Balbuena for the past five years. Dr. Balbuena continuously enlightened my mind with her broad knowledge and intelligence and encouraged me with her infinite patience whenever I met difficulties. Dr. Balbuena's enthusiasm for science always inspired my working spirit. Besides, not only being a wonderful research advisor with financial support, Dr. Balbuena is also a great mentor for my life and career development.

I would like to thank the other members of the committee, Dr. James Batteas, Dr. Jorge Seminario and Dr. Daniel Shantz, for patiently reading through this dissertation and providing helpful comments.

I would like to thank Dr. Alberto Martinez-Limia for his initial work on force field development and simulation programming. His patience in explaining to me all these stuff and his highly organized documentation made it possible for me to smoothly go on with his work. I am thankful to Dr. Yuguang Ma, Dr. Yingchun Zhang, and Dr. Zhihui Gu for their suggestions and discussions. I would like to thank all members of Dr. Balbuena's group. They created a friendly climate in the office and shared their interesting culture from their own countries.

Computer resources from Artie McFerrin Department of Chemical Engineering, Texas A&M University, U.S. Army Research Laboratory (ARL), and National Energy Research Scientific Computing Center (NERSC) are highly appreciated.

I want to express my sincere appreciation to my family for their unconditional support. My parents-in-law and my parents are always there when I need any help. Their kind help in taking care of my son made it possible for me to finish my research work and dissertation. I have been blessed to have Lijun as my husband. His love, support, and sacrifice for our family are highly appreciated. Finally, I would like to thank my son, Kenneth, who was totally cooperative during the many days and nights that I worked on my dissertation and can't accompany him. What's more, he can always cheer me up with his sunny smile, when I feel frustrated.

TABLE OF CONTENTS

Page

Page

LIST OF FIGURES

FIGURE Page

FIGURE Page

FIGURE Page

LIST OF TABLES

1. INTRODUCTION

1.1 Background

Single wall carbon nanotubes (SWCNTs) were first discovered in 1993 by Iijima and his group at the NEC laboratory[1] and by Bethune and coworkers at the IBM Almaden laboratory[2]. Their novel electronic, optical and mechanical properties have provided great potential for a wide variety of applications and attracted tremendous theoretical and experimental research work in this area. However most of these properties are associated with the chirality of the nanotube while SWCNTs are normally produced with a broad distribution of chirality. Limitation of techniques to separate different chiral nanotubes and tremendous loss in this step is one of the reasons that limit the application of SWCNTs. A recently developed chemical vapor deposition (CVD) synthesis process called CoMoCAT yields SWCNTs of controlled diameter and chirality, making them extremely attractive for technological applications.[3-6]

Due to the lack of knowledge of the mechanisms of the selective growth, experiments could only be carried out by trial and error. Despite tremendous efforts made in this field, five years after the first report of this synthesis technique, nanotube (6, 5) is still the only kind of nanotube that could be produced with high selectivity. Considering the high growth speed of these reactions and small dimensions of the catalysts, theoretical studies are essential to combine with experimental analysis to study

---

This dissertation follows the style of *Journal of Physical Chemistry C.*

the reasons behind the selective growth mechanisms.

1.2 Basic structure of single-wall carbon nanotube

Carbon nanotubes are hollow cylinders of graphite sheets. They can be looked at as single molecules, regarding their small size (~nm in diameter and ~μm in length), or as quasi-one dimensional crystals with translational periodicity along the tube axis. A tube, as shown in Figure1.1(a), made of a single graphite layer rolled up into a hollow cylinder is called a Single Wall Carbon Nanotube (SWCNT); a tube, as shown in Figure 1.1(b), comprising several, concentrically arranged cylinders is referred to as a multiwall carbon nanotube (MWCNT).

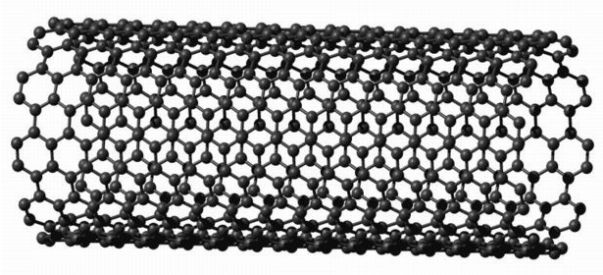

(a)

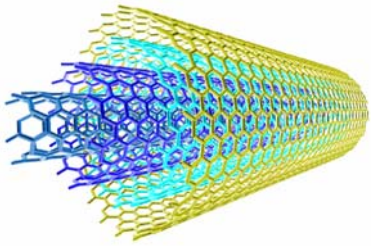

(b)

Figure 1.1. Single wall carbon nanotube (a) and multiwall carbon nanotube (b).

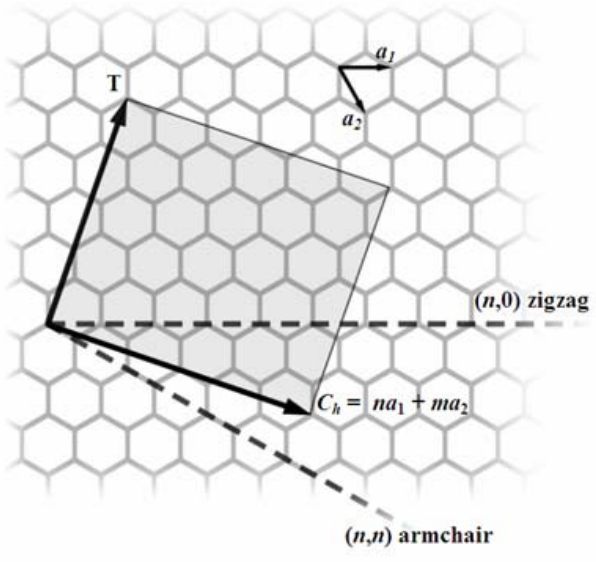

Figure 1.2. Graphene honeycomb lattice.

Figure1.2 shows the graphene honeycomb lattice. The unit cell is spanned by two lattice vectors $\mathbf{a_1}$ and $\mathbf{a_2}$ and contains two carbon atoms at positions $1/3(\mathbf{a_1}+\mathbf{a_2})$ and $2/3(\mathbf{a_1}+\mathbf{a_2})$. In carbon nanotubes the graphite sheet is rolled up in such a way that a vector $\mathbf{c} = m\mathbf{a_1} + n\mathbf{a_2}$ becomes the circumference of the tube. In other words after rolled up, the two ends of the circumference vector overlap with each other. This circumferential vector **c**, which is usually denoted by the pair of integers (m, n), uniquely defines a particular tube. The direction of the chiral vector is measured by the chiral angle θ, which is defined as the angle between **c** and $\mathbf{a_1}$ and can be calculated from equation 1.1

$$\cos\theta = \frac{m + n/2}{\sqrt{m^2 + mn + n^2}} \qquad (1.1)$$

When n =m, the chiral angle is 30°, and the nanotube is called armchair nanotube. When either n or m is zero, the chiral angle is 0° and the nanotube is called zigzag

nanotube. All other nanotubes, with chiral angles intermediate between 0° and 30°, are know as chiral nanotubes.

The diameter of the nanotube can be calculated by equation 1.2

$$d = \frac{a_{c-c}}{\pi}\sqrt{m^2 + mn + n^2} \qquad (1.2)$$

where $a_{c\text{-}c}$ is the distance between neighboring carbon atoms in the flat sheet.

Table 1.1: Number of IPR caps for nanotubes studied in this work

nanotube	diameter (nm)	number of IPR caps
(5, 5)	0.687	1
(6, 5)	0.757	1
(9, 1)	0.757	1
(8, 3)	0.782	3
(6, 6)	0.824	18
(7,5)	0.829	14

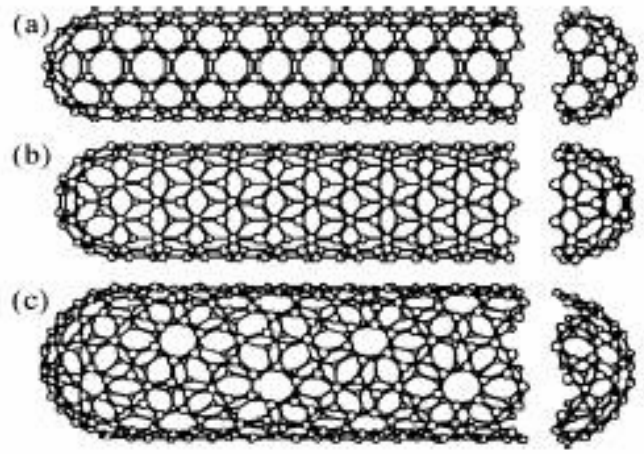

Figure 1.3. Matches between tubes and caps. ((a) nanotube (5, 5), (b) nanotube (9, 0), (c) nanotube (10, 5).)

Depending on the growth mechanism and posterior purifying process, the nanotube end can be open, terminated by a cap structure, or containing other impurity clusters or atoms from the catalyst. The cap is a half fullerene, which is made up of 6 five-member rings distributed in a network of six-member rings.[7]. The more even the five-member rings are distributed, the more stable is the cap structure.[8] According to the isolated pentagon rule (IPR), no neighbored pentagons should exist in the cap in order to have reasonably stable structure and such caps that follow the isolated pentagon rule are called IPR caps. A certain cap can only fit with nanotube of certain chiral vector as shown in Figure 1.3. But it is possible that several cap structures could fit one nanotube. The bigger is the diameter of the nanotube, the higher the number of corresponding possible cap structures. There is only one possible IPR cap structure for nanotubes (5, 5), (6, 5) and (9, 1) respectively.[9,10] Table 1.1 lists diameter and number of possible IPR caps of 6 kinds of nanotube that will be discussed in this work.

1.3 Properties of SWCNTs

The electrical and mechanical properties of carbon nanotubes have captured the attention of researchers worldwide. Understanding these properties and exploring their potential applications have been a main driving force for this area. Since nanotubes usually have very large aspect ratios (from 10^2 to 10^7), they are normally modeled as one dimensional solids.[11] Most of their properties depend very sensitively on the diameter and helicity of the tube.

1.3.1 Mechanical properties of SWCNTs

It is reported that carbon nanotubes have Young's moduli of about 0.9-1.7 TPa[12], comparable to 1.05-1.20 TPa of diamond which is the stiffest material in the world. This strength results from the covalent sp^2 bonds formed between the individual carbon atoms. Since carbon nanotubes have a low density for a solid of 1.3-1.4 g/cm^3, their specific strength of up to 48,000 kN·m/kg is the highest among known materials, compared to high-carbon steel's value of 154 kN·m/kg.

Single wall carbon nanotubes show remarkable flexibility and can bent around small circles or about sharp bends without breaking. When the compression or shear stress is released, the original circular cross section of the nanotube can in many cases be restored.[13]

Under excessive tensile strain, the tubes will undergo plastic deformation, which means the deformation is permanent. This deformation begins at strains of

approximately 5% and can increase the maximum strain the tube undergoes before fracture by releasing strain energy.

1.3.2 Electrical properties of SWCNTs

Because of the symmetry and unique electronic structure of graphene, the structure of a nanotube strongly affects its electrical properties. For a given (n, m) nanotube, if n − m is a multiple of 3, then the nanotube is metallic, otherwise the nanotube is a semiconductor. Thus all armchair (n=m) nanotubes are metallic, and nanotubes like (5, 0), (6, 4), (9, 1), etc. are semiconducting. In theory, metallic nanotubes can have an electrical current density more than 1,000 times greater than metals such as silver and copper.

1.3.3 Properties of nanotubes with finite length

When we study growth process of carbon nanotube, physical and chemical properties associated with the nanotube finite length, especially the structure of the nanotube end becomes more important.

Since the nanotube is made up of carbon rings, the aromaticity of these rings is an important property of the nanotube. Aromaticity is a manifestation of electron delocalization in closed circuits, either in two or three dimensions. This results in energy lowering, often quite substantial and a variety of unusual chemical and physical properties. These include a tendency toward bond length equalization, unusual reactivity, and characteristic spectroscopic features. Since aromaticity is related to induced ring currents, magnetic properties are particularly important for the nanotubes detection and

evaluation.[14,15] The use of absolute magnetic shielding computed at ring centers (defined as a nonweighted mean of the heavy atom coordinates) with quantum mechanical programs is now a new widely accepted aromaticity/antiaromaticity criterion: negative Nucleus Independent Chemical Shift (NICS) denote aromaticity, positive NICSs indicate antiaromaticity. Originally, NICS at the geometry center of a ring is used as aromatic criteria.[14] Later in order to avoid the influence of σ contribution, the NICS value 1.0 Å above the plane of the ring is widely used for planar or nearly planar molecules. For rings that are not totally planar like in nanotube, the average value of 1.0 Å below and above the center of the ring is used.[16] For a very simple molecule, the NICS is dissected into contributions of each molecular orbital (MO) and the contribution of Π orbitals are chosen as aromatic criteria.[17,18] However such calculation is only possible for small systems. It is proposed that even NICS values 1.0 Å above the plane of the ring are sometimes misleading especially in complex systems. In such case the NICS scan method is used to evaluate the aromaticity: negative, NICS scan values showing a relatively deep minimum are found in aromatic systems, highly positive, decreasing with the distance in antiaromatic systems, and small in nonaromatic systems.[19,20] However, there is still debate on the using of NICS as solely aromatic criteria, especially on using it to study local aromatic property of polycyclic systems[19,20] since it is believed that the diamagnetic or paramagnetic ring current is influenced by the neighboring rings. Despite these debates, we believe information about NICS calculations is still important since they could at least reveal the diamagnetic/paramagnetic currents in the ring.

With this probe, it has been found that the chemical structure of finite-length open-end armchair nanotubes can be Kekulé (a benzene structure, all rings are aromatic), incomplete Clar (a p-phenylene network flanked by peripheral double bonds) or complete Clar networks (an array of p-phenylene network that covers the whole tube structure), depending on the length of the tube.[16] Finite-length open-end (m, n) chiral nanotubes are fully benzenoid if m-n = 3k. Otherwise there is a seam of double bonds warp about a benzenoid tube at a certain angle.[21] Nanotubes with two ends bonded to cap structures are quite different from those with open ends. It has been reported that the local aromaticity of rings in a nanotube with two ends closed by cap structures is determined by the arrangement of the five-membered rings in the cap and such behavior is explained by the Pentagon-Proximity model. [22]

1.4 Application of carbon nanotubes

The large aspect ratio, small diameter, low density, high strength and flexibility, and novel electronic properties of carbon nanotubes make them of potential use in many areas. Nanotubes can be utilized individually or as an ensemble to build functional device prototypes, as has been demonstrated by many research groups.

1.4.1 Nanotube-filled composites

The most important application of nanotubes based on their mechanical properties will be as reinforcement in composite materials. In nanotube-filled polymer composites, nanotube reinforcements will increase the toughness of the composites by absorbing energy during their highly flexible elastic behavior. However, the advantage of using

nanotubes as fillers over traditional carbon fibers is not quite obvious and it is believed that the real role of nanotubes as an efficient reinforcing fiber will have to wait until it is known how to chemically manipulate the nanotube surfaces making strong interfaces between individual nanotubes and the matrix materials.[23]

1.4.2 Nanoprobes and sensors

With extremely small sizes, high conductivity, high mechanical strength and flexibility, nanotubes have great potential in being used as nanoprobes. A single MWCNT attached to the end of a scanning probe microscope tip for imaging has already been demonstrated.[23] The advantage of the nanotube tip is its slenderness and the possibility to image features such as very small, deep surface cracks, which are almost impossible to probe using the larger, blunter etched Si or metal tips. MWCNT and SWCNT tips were used in a tapping mode to image biological molecules with resolution never achieved before.[24]

Besides, it is also possible to use nanotubes as active tools for surface manipulations. Ten nanometer lines have been written on oxidized silicon substrates using nanotube tips at relatively high speeds.[24]

Recent research has also shown that nanotubes can be used as advanced miniaturized chemical sensors.[25] The electrical resistivities of SWCNTs were found to change sensitively on exposure to gaseous ambient containing molecules of NO_2, NH_3 and O_2. By monitoring the change in the conductance of nanotubes, the presence of gases could be precisely monitored. The response times of nanotube sensors are at least an order of magnitude faster (a few seconds for a resistance change of one order of magnitude) than

those based on presently available solid state (metal-oxide and polymers) sensors. Besides, the small dimensions and high surface area offer special advantages for nanotube sensors.

1.4.3 Nanotube applications in electrical circuits

Carbon nanotubes have many properties—from their unique dimensions to an unusual current conduction mechanism—that make them ideal components of electrical circuits.

Nanotube based transistors have been made that operate at room temperature and that are capable of digital switching using a single electron.[26]

The first nanotube integrated memory circuit was made in 2004.[27] An alternative way to make transistors out of carbon nanotubes is to use random networks of them. By doing so one can produce devices in large scale at the wafer level.[28]

1.4.4 Obstacles for nanotube applications

Carbon nanotubes have come a long way since their discovery in 1991. There are already some applications as discussed above. However, there are also some challenges that face the application of nanotubes.

The first challenge is the manipulation of nanotubes. Like in any other area of nanotechnology the ability to manipulate structures at the atomic scale is the key challenge.

Although several analytical techniques such as Raman spectroscopy, fluorescent spectroscopy, scanning probe microscopy, and electron diffraction can be used to

provide an average measurement over a large number of nanotubes, so far there is no technique available to accurately and rapidly determine the atomic structure of individual carbon nanotubes [29]

More importantly, there are several aspects needed to be improved in the production technique. Most electronic applications of carbon nanotubes require aligned SWCNTs that are reasonably homogeneous in diameter, length and electronic properties which are determined by the nanotube's chirality. Controlling the diameter and chirality of the nanotube remain challenging in the production of carbon nanotubes. Another current challenge is the inability to create complex nanotube arrays reliably on an industrial scale.

Besides the quantities of nanotubes that can be manufactures still falls far short of what industry would need. There are no available technique that can produce nanotubes of reasonable purity and quantities. The market price of nanotubes is also too high presently (~$200 per gram) for any realistic commercial application.[23]

1.5 Synthesis of carbon nanotubes

In 1991, Iijima of the NEC Laboratory in Japan reported the first observation of multi-walled carbon nanotubes in carbon-soot made by arc discharge.[30] About two years later, he made the observation of SWCNTs. [1,7] Since then, the past decade witnessed significant research efforts in developing efficient and high-yield nanotube growth method. Techniques have been developed to produce nanotubes in sizeable quantities, including arc discharge, laser ablation, and chemical vapor deposition (CVD).

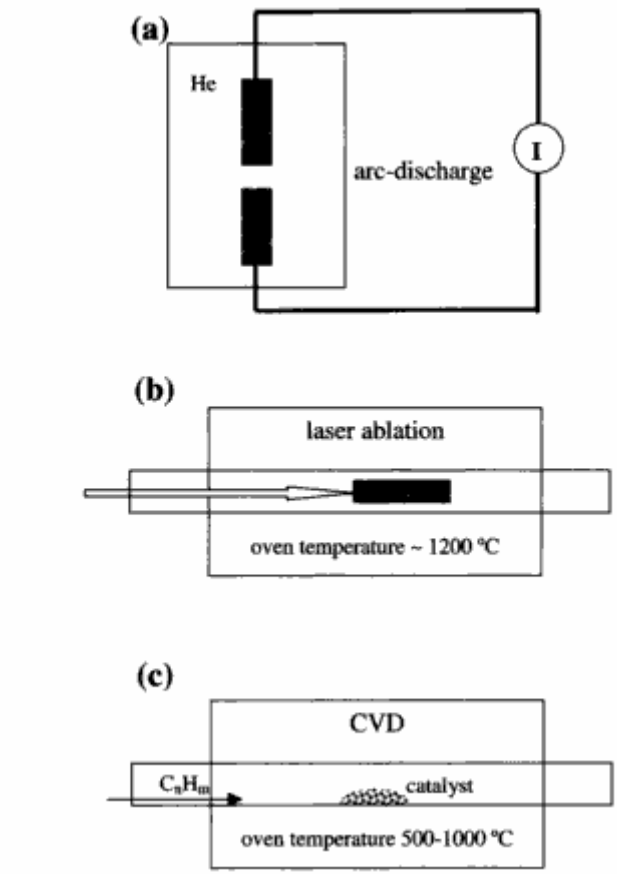

Figure 1.4. Schematic experimental setups for nanotube growth methods.[23]

1.5.1 Arc discharge

Nanotubes were observed in 1991 in the carbon soot of graphite electrodes during an arc discharge, by using a current of 100 amps, that was intended to produce fullerenes.[30]

In arc-discharge, carbon atoms are evaporated by plasma of helium gas ignited by high currents passed through opposing carbon anode and cathode as shown in Figure 1.4(a). Typical operating conditions include the use of carbon rod electrodes of 5-20mm diameter separated by ~1mm with a voltage of 20~25 V across the electrodes and a dc

electric current of 50~120 A flowing between the electrodes. The arc is typically operated in ~500 torr He with a flow rate of 5~15 ml/s for cooling purposes. As the nanotubes form, the length of the positive electrode (anode) decreases and carbon deposit forms on the negative electrode.

For multi-wall carbon nanotube synthesis, no catalyst is needed and nanotubes are found in bundles in the inner region of the cathode deposit where the temperature is a maximum (2500~3000°C), while for the growth of SWCNTs, metal catalyst is needed. Typical catalyst includes transition metals such as Co, Ni, and Fe, rare earths such as Y and Gd, and mixed catalysts such as Fe/Ni, Co/Ni and Co /Pt.

1.5.2 Laser ablation

In the laser ablation process, a pulsed laser vaporizes a graphite target in a high temperature reactor while an inert gas is bled into the chamber as shown in Figure 1.4(b). The nanotubes develop on the cooler surfaces of the reactor, as the vaporized carbon condenses. A water-cooled surface may be included in the system to collect the nanotubes.

This process was invented by Richard Smalley and co-workers at Rice University, who at the time of the discovery of carbon nanotubes, were blasting metals with the laser to produce various metal molecules. When they heard of the discovery they substituted the metals with graphite to create multi-walled carbon nanotubes.[31] Later that year the team used a composite of graphite and metal catalyst particles to synthesis single-walled carbon nanotubes.[32]

This method has a yield of around 70% and produces primarily single-walled carbon nanotubes with a controllable diameter determined by the reaction temperature. However, it is more expensive than either arc discharge or chemical vapor deposition.[26]

1.5.3 Chemical vapor deposition (CVD)

For a long time, arc-discharge and laser-ablation have been the principal methods for obtaining nearly perfect SWCNTs. There are several issues concerning these approaches. First, both methods rely on evaporating carbon atoms from solid carbon sources at more than 3000°C, which is not efficient and limits the scale up of the process. Secondly, the nanotubes synthesized by the evaporation methods are in tangled forms that are difficult to purify, manipulate and assemble for building addressable nanotube structures. Chemical Vapor Deposition (CVD) technique shows great advantage in these aspects.

A schematic experimental setup for CVD growth is depicted in Figure 1.4(c). The process involves heating carbon monoxide or a hydrocarbon gas through the tube reactor for a period of time. Materials grown over the catalyst are collected upon cooling the system to room temperature. The key parameters in nanotube CVD growth are the carbon source, catalysts and growth temperature. The active catalytic species are typically transition-metal nanoparticles formed on a support material such as alumina.

During CVD, a substrate is prepared with a layer of metal catalyst particles, most commonly nickel, cobalt, iron, or a combination. The metal nanoparticles can also be produced by other ways, including reduction of oxides or oxides solid solutions. The diameters of the nanotubes that are to be grown are related to the size of the metal particles. This can be controlled by patterned (or masked) deposition of the metal,

annealing, or by plasma etching of a metal layer. The substrate is heated to approximately 700°C. To initiate the growth of nanotubes, two gases are bled into the reactor: a process gas (such as ammonia, nitrogen, hydrogen, etc.) and a carbon-containing gas (such as acetylene, ethylene, ethanol, methane, etc.). Nanotubes grow at the sites of the metal catalyst: the carbon-containing gas is broken apart at the surface of the catalyst particle, and the carbon is transported to the edges of the particle, where it forms the nanotubes. The catalyst particles can stay at the tips of the growing nanotube during the growth process, or remain at the nanotube base, depending on the adhesion between the catalyst particle and the substrate.

CVD is a common method for the commercial production of carbon nanotubes. For this purpose, the metal nanoparticles will be carefully mixed with a catalyst support (e.g., MgO, Al2O3, etc) to increase the specific surface area for higher yield of the catalytic reaction of the carbon feedstock with the metal particles.

Of the various means for nanotube synthesis, CVD shows the most promise for industrial scale deposition in terms of its price/unit ratio. There are additional advantages to the CVD synthesis of nanotubes. CVD is capable of growing nanotubes directly on a desired substrate, whereas the nanotubes must be collected in the other growth techniques. The growth sites are controllable by careful deposition of the catalyst. A method has been devised to grow suspended SWCNT networks with directionality on substrates containing lithographically patterned silicon pillars.[33]

1.6 Selective growth of SWCNT by CoMoCAT method

A recently developed CVD synthesis process called CoMoCAT because of the use of cobalt-molybdenum based catalysts[3-6], yields SWCNTs of controlled diameter and chiralities, Table 1.2 displays the selectivity characteristics of the SWCNTs produced by this process.

Table 1.2: Estimated population on different catalysts and different reaction conditions from the analysis of the M11, S22 and S11 optical absorption of the samples[6]

	support		SiO_2				MgO
	temp (°C)		700	750	800	850	750
(*n*,*m*) species	semicond	(6,5)	54%	42%	55%	6%	19%
		(8,4)	4%	16%	4%	6%	12%
		(7,5)	8%	8%	6%	10%	26%
		(7,6)	8%	7%	6%	15%	13%
		(8,6)			1%	10%	2%
		(8,7)			2%	13%	2%
	metallic	(6,6)	14%	19%	15%	17%	22%
		(7,7)	13%	10%	10%	14%	3%
		(8,8)				6%	

The reported CoMoCAT data correspond to the use of a silica support (Sigma-Aldrich SiO_2 with 6 nm average pore size and BET surface area of 480 m^2 g^{-1}) and a bimetallic catalyst prepared from cobalt nitrate and ammonium heptamolybdate precursors. The total metallic loading in the catalyst was 2 wt %, with a Co:Mo molar ratio of 1:3. Before exposure to the CO feedstock, the catalyst was heated to 500 °C in a flow of gaseous H_2, and further heated to 750 °C under flowing He. The CO

disproportionation reaction: $2CO \longrightarrow CO_2 + C$ used to produce SWCNTs then run in a fluidized bed reactor under a flow of pure CO at 5 atm total pressure.

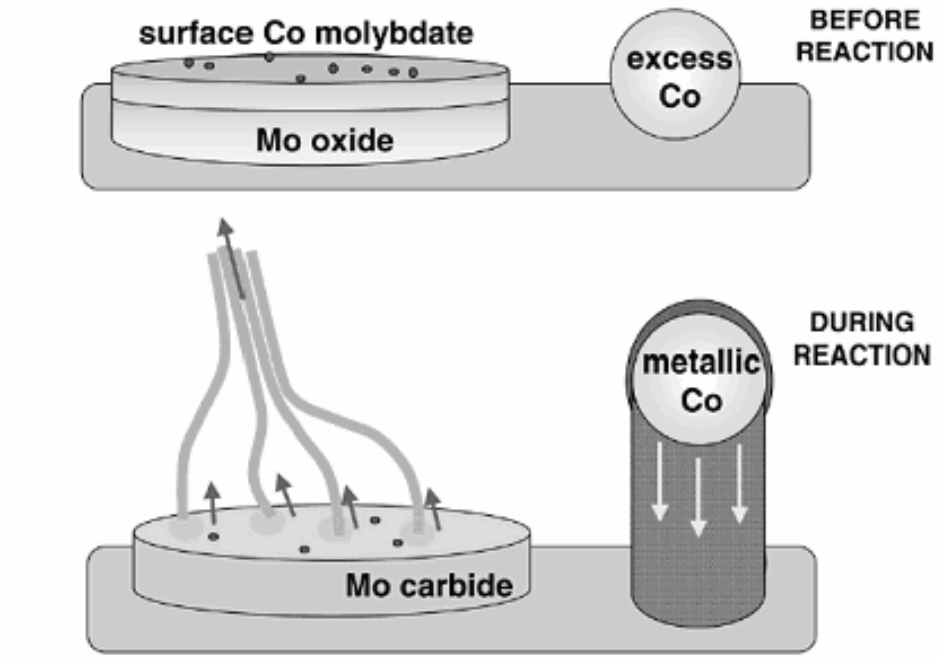

Figure 1.5. Schematic representation of the state of the catalyst components before and during the production of SWCNTs.[PP3] The Co species stabilized by Mo resist reduction and sintering before the reaction. Under CO, Mo becomes carbide while Co becomes metallic and generates the SWCNTs. The excess Co, not stabilized by Mo, produces MWCNTs and carbon fibers.

The initial stage of the CoMoCAT process is as shown in Figure 1.5[3]: interactions between Mo oxides and Co stabilize the Co catalyst against aggregation through high-temperature sintering. It is found that these interactions vary with the Co:Mo ratio and evolve during the subsequent stages of the catalyst life. At the low ratios used here (1:3), catalyst particles contain highly dispersed molybdenum oxide covered by a Co-molybdate layer. With exposure to CO, the Mo oxide is converted into Mo carbide. This

disrupts the molybdate layer, allowing Co to be reduced by CO and migrate on the surface to form small, growing catalytic clusters of metallic Co. Carbon accumulates on these nanoclusters through CO disproportionation, leading to the formation of correspondingly small diameter SWCNTs. But it is still not clear how the SWCNTs grow on these Co clusters and why such a high selectivity could be achieved. Considering the high speed of these reactions and small dimensions of the catalysts, it is very hard to answer these questions based only on the analysis of experimental results.

1.7 Theoretical studies of SWCNT growth

Considerable effort has been dedicated to understanding SWNT growth mechanisms via theoretical studies, such as ab initio,[34-36] as well as classical and quantum molecular dynamics simulations,[36-49] and coarse-grained methods such as kinetic Monte Carlo techniques.[42,43] However, so far, due in part to the complexity of the process involving a wide range of time and length scales, a clear picture regarding nanotubes growth has not yet emerged.

One of the more accepted mechanisms of SWNT growth is the closed end (cap-ended) mechanism, whereby a fullerene-type cap is lifted off from the metal catalyst and its continued growth evolves into a nanotube. The nucleation process of the nanotube given by the formation of the cap and its lifting from the catalyst surface is very crucial for the growth of the nanotube. Supersaturation induced by temperature gradient is often used to explain it, which is very reasonable for large catalyst particles.[50] Others have proved that nucleation of a closed cap over a flat surface is energetically favorable compared to any other structure with dangling bonds or to a fullerene-type structure.[51]

But for catalysts with small diameters, in the order of 1 nm, it is unlikely that a temperature gradient or a density gradient exists across the radial direction. Atomistic simulations illustrated the nanotube nucleation process from small Fe clusters without the need of an applied temperature or density gradient.[48,49] In those simulations, new carbon atoms are added to the center of the cluster, thus one may speculate that keeping a flow of C atoms at the center of the catalyst may be one of the reasons that artificially force the carbon atoms to nucleate outside of the catalyst.

1.8 Objectives

In this project, we use computational techniques, combining with analyses of experimental results to study the selective growth of SWCNTs by MoCoCAT method.

We develop a series of reactive force fields to describe the interactions in SWCNT growth process by CVD method. Then, with this force field, we simulate the growth process of SWCNT both on a floating catalyst cluster and on a cluster attached to substrate.

Though from molecular dynamics simulations, it is possible to observe the basic steps of SWCNT growth, due to time limit and limited accuracies of the force field, it is nearly impossible to get perfect nanotubes with defined chirality, and to find out reasons of selective growth of SWCNT just from MD simulation results will be very hard. So we approach the problem in the opposite way: instead of growing nanotube from MD simulations to see which chiral vector is easier to grow, we study the properties of nanotubes with different chirality to see what property or properties may be the reason that makes certain nanotubes easier to grow.

Since from experimental observations, the substrate that catalyst clusters loaded on has significant effect on the selective growth, we study the interaction between the catalyst cluster and the substrate.

2. MOLECULAR DYNAMICS SIMULATIONS OF SWCNT GROWTH*

2.1 Force field development

2.1.1 Main interatomic interactions present in a SWCNTs catalyzed growth process

Since the focus of this work is to develop the mathematical functions able to describe the metal-C and C-C interactions in a catalyzed synthesis of SWNTs, we first provide some details of what is known about the process from theoretical and experimental investigations. As mentioned in the introduction, one successful synthesis method is based on chemical vapor deposition of a precursor gas on an appropriate catalytic surface, at pressures that vary between a few atm[52] and ~80-100 atm[53] and temperatures in the order of 1000~1300K. The catalyst is usually a nanoparticle (from 0.5 to a few nanometers size) of a transition metal (Co, Fe, Ni, and others) that could be floating in a

---

vapor [54] or supported on a substrate.[3]

Thus, the main interatomic interactions present in this system are: metal-metal interactions in the nanocatalyst particle, metal-C interactions inside the catalyst, metal-C interactions on the surface of the catalyst, C-C interactions inside the metal nanoparticle, C-C interactions on the surface of the metal nanoparticle, and C-C interactions in the carbon nanostructure (cap or nanotube) sufficiently far from the metal atoms.

Metal-metal interaction can be successfully described by the Sutton-Chen many-body potential.[54,55] Carbon-carbon interactions have been successfully modeled using the reactive empirical bond order (REBO) Brenner potential.[56,57] Based on density functional calculations of small clusters NiC_n and Ni_n (n=1~3), metal-C and metal-metal reactive force fields have been developed to simulate catalytic growth of nanotubes and fullerene[39,43,46,47], where the catalysts consist of a few metal atoms. In this work, we have adapted the Ni-C potential functions proposed by Yamaguchi and Maruyama[47] and the Brenner C-C potential,[57] in order to model the main features of the catalyzed SWNT synthesis process. So with the exception of the metal-metal interactions, we consider all the above interatomic forces in the following section to develop appropriate force fields needed to describe the bond breaking and bond forming processes in the synthesis of SWCNTs.

2.1.2 Metal-carbon potential

Yamaguchi and Maruyama[47] introduced many-body potential functions (equations 2.1-2.3) to describe the interaction between metal and C atoms, where E_b, the interaction

energy between two atoms i and j separated a distance r_{ij}, is computed as the combination of Morse-type repulsive and attractive terms, $V^R(r_{ij})$ and $V^A(r_{ij})$ respectively,

$$E_b = V^R(r_{ij}) - V^A(r_{ij}) \tag{2.1}$$

$$V^R(r_{ij}) = f(r_{ij}) \frac{D_e}{S-1} \exp\left\{-\beta\sqrt{2S}\left(r_{ij} - R_e\right)\right\} \tag{2.2}$$

$$V^A(r_{ij}) = f(r_{ij}) \frac{D_e S}{S-1} \exp\left\{-\beta\sqrt{2/S}\left(r_{ij} - R_e\right)\right\} \tag{2.3}$$

$f(r)$ is a cutoff function for the potential, given by:

$$f(r) = \begin{cases} 1 & (r < R_1) \\ \left(1 + \cos\left(\pi \frac{r - R_1}{R_2 - R_1}\right)\right)/2 & (R_1 < r < R_2) \\ 0 & (r > R_2) \end{cases} \tag{2.4}$$

$f(r)$ is also used to determine the coordination number N_i^M of the atom i, and R_1 and R_2 are model parameters, as explained later. D_e and R_e are the equilibrium binding energy and bond distance between i and j, calculated as functions of an average atomic coordination number N_{ij} with equation 2.5 and 2.6

$$D_e = D_{e1} + D_{e2} \exp\left[-C_D(N_{ij})\right] \tag{2.5}$$

$$R_e = R_{e1} - R_{e2} \exp\left[-C_R(N_{ij})\right] \tag{2.6}$$

S and β in equations 2.2 and 2.3 are parameters taken from the original reference.[PP47] Estimation of D_{e1}, D_{e2}, CD, CR, R_{e1}, and R_{e2} for the Ni-C system is discussed at the end of this section.

In metal clusters of more than 20 atoms it is possible that one carbon is bonded to three (when C is on the surface of the metal cluster) or even up to eight metal atoms (when C is inside of the cluster). To account for these interactions, our modified potential includes the dependence that arises from the presence of several metal atoms around a carbon atom *j*. In addition, the effect of different bonding structures such as fullerene and carbon chains interacting with metal atoms are also added to the potential function that describes carbon-metal interactions. Two systems (NiC_2H_4 and $NiC_{16}H_{10}$) were investigated to establish possible differences in the metal-carbon bond of carbon atoms which are also involved in sp^2 carbon-carbon bonds. DFT optimizations at the B3PW91/LANL2DZ level of NiC_2H_4 and $NiC_{16}H_{10}$ (Figure 2.1) provided an estimate for the total C-Ni binding energy of 0.64 and 0.12 eV respectively.[58] This is a remarkable difference compared to the 4.2 eV of binding energy for a single C atom bonded to three metal atoms -the most common case on the surface of a metal cluster.

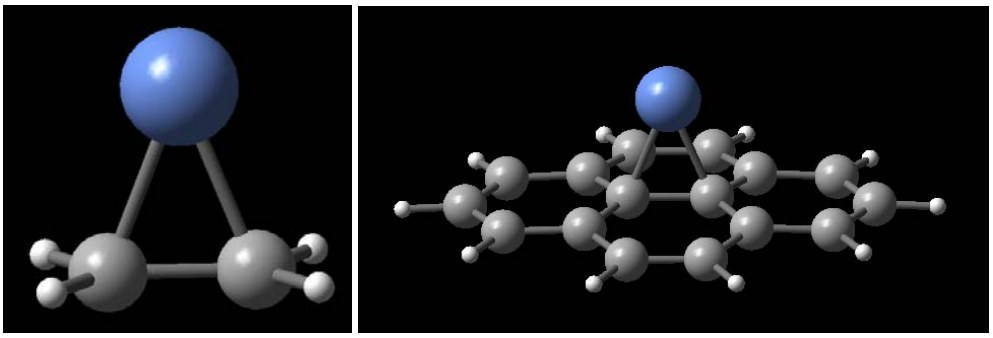

Figure 2.1. Optimized geometries of NiC_2H_4 (left) and NiC_2H_4 (right).[58]

Similar estimations have been made by other authors[51], and led us to assume that the C atoms bonded in graphite-type structures are weakly bonded to the metal surface. To

describe this feature, equation 2.1 is modified so that the energy of the bond between the metal atom i and the carbon atom j is described by equation 2.7[58]:

$$E_{ij}^{MC} = G\left(\alpha_{ij}^{MC}, V^R(r_{ij}), V^A(r_{ij})\right) \qquad (2.7)$$

where a new parameter α_{ij}^{MC} (equation 2.12), which is a function of the bonding status of carbon atom *j*, is introduced in the metal-C potential. α_{ij}^{MC} equals 1 when the carbon atom *j* does not bond to other carbon atoms (C0); α_{ij}^{MC} equal to α_1^{MC}, a value between 0 and 1, when the carbon atom *j* is bonded to two other C atoms (CII), and when the carbon atom *j* is bonded to three other C atoms (CIII), α_{ij}^{MC} equals a value α_2^{MC}, which is still greater than 0, but smaller than α_1^{MC}.

The function *G* in equation 2.7 is designed to modify the attractive and repulsive parts of the potential using varying values of the α_{ij}^{MC} parameter, in the interval $0 < \alpha_{ij}^{MC} < 1$. Such behavior is needed for the description of C-metal interactions in cases when a C atom is bonded to other C atoms and therefore weakly bonded to the metal, while a repulsive core remains in place. The most successful form of $G\left(\alpha_{ij}^{MC}, V^R(r_{ij}), V^A(r_{ij})\right)$ is given by equation 2.8[58]

$$G = \alpha_{ij}^{MC} V^R(r_{ij}) - \left(\alpha_{ij}^{MC}\right)^{1.1} V^A(r_{ij}) \qquad (2.8)$$

To include the effect of several metal atoms surrounding a carbon atom j, instead of defining a repulsive and attractive part as function of carbon coordination number as in Yamaguchi and Maruyama potential,[47] we define them as a function of N_{ij}, which is a

total coordination number including the relative influence of the carbon and metal coordination numbers N_i^C and N_j^M as shown in equations 2.9-2.11[58].

$$N_i^C = \sum_{carbon\, k \neq i} f(r_{ik}) \tag{2.9}$$

$$N_j^M = \sum_{metal\, k \neq j} f(r_{jk}) \tag{2.10}$$

$$N_{ij} = N_j^M + \lambda N_i^C \tag{2.11}$$

The λ parameter weights the contribution of the metal and C coordination numbers.

$$\alpha_{ij}^{MC} = \begin{Bmatrix} 1 & (N_{carbon}^C < N_1^C) \\ \alpha_1^{MC} + \dfrac{(1-\alpha_1^{MC})}{2}\left[1+\cos\left(\pi \dfrac{N_{carbon}^C - N_1^C}{N_2^C - N_1^C}\right)\right] & (N_1^C < N_{carbon}^C < N_2^C) \\ \alpha_1^{MC} & (N_2^C < N_{carbon}^C < N_3^C) \\ \alpha_2^{MC} + \dfrac{(\alpha_1^{MC} - \alpha_2^{MC})}{2}\left[1+\cos\left(\pi \dfrac{N_{carbon}^C - N_3^C}{N_4^C - N_3^C}\right)\right] & (N_3^C < N_{carbon}^C < N_4^C) \\ \alpha_2^{MC} & (N_{carbon}^C > N_4^C) \end{Bmatrix} \tag{2.12}$$

Other $G\left(\alpha_{ij}^{MC}, V^R(r_{ij}), V^A(r_{ij})\right)$ functions were tested, with less satisfying results, for example equation 2.13[58] where the metal-C potential is reduced by $0.0 < \alpha_{ij}^{MC} < 1.0$, while the function $V^{LJ}(r_{ij})$ maintains the necessary repulsive core.

$$G = \alpha_{ij}^{MC}\left(V^R(r_{ij}) - V^A(r_{ij})\right) + (1.0 - \alpha_{ij}^{MC}) V^{LJ}(r_{ij}) \tag{2.13}$$

with

$$V^{LJ}(r_{ij}) = 4\varepsilon\left[\left(\frac{\sigma}{r_{ij}}\right)^{12} - \left(\frac{\sigma}{r_{ij}}\right)^{6}\right] \tag{2.14}$$

An alternative form of G (equation 2.15) where the attractive part is reduced and the repulsive part remains intact was also tested[58].

$$G = V^R(r_{ij}) - \alpha_{ij}^{MC} V^A(r_{ij}) \qquad (2.15)$$

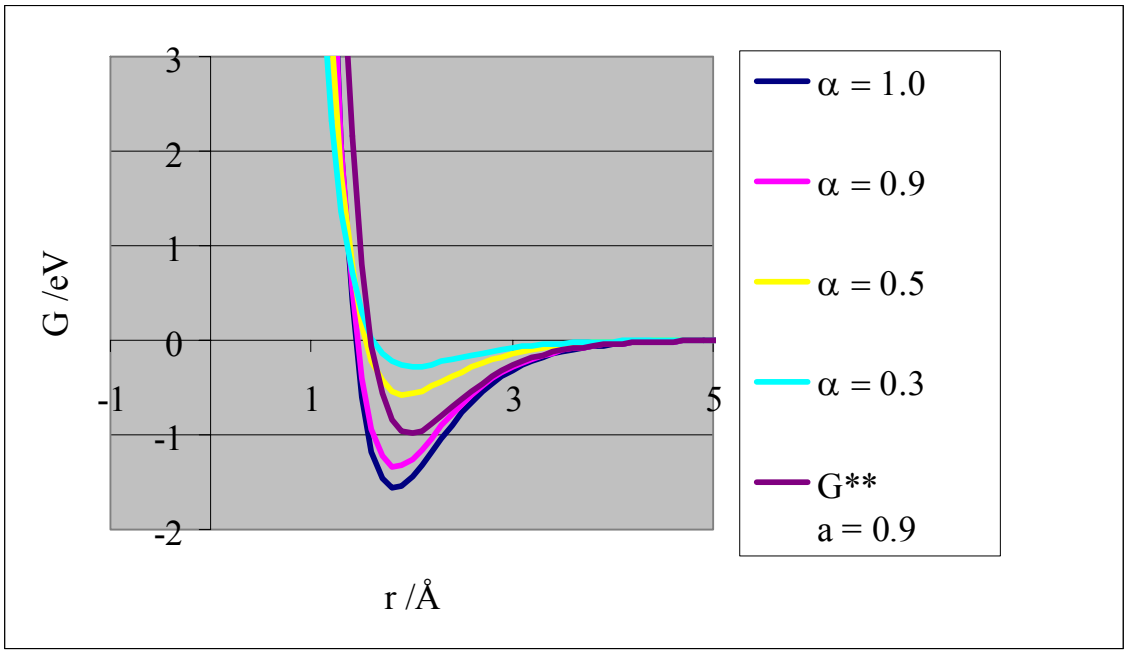

Figure 2.2. Behavior of the G function (equation 2.8) for different values of α_{ij}^{MC} (For comparison, the potential for equation 2.15 (denoted as G**) is shown for α_{ij}^{MC} = 0.9, where a drastic change of the size of the repulsion core is observed).[58]

Analysis of G from equations (2.13) and (2.15) shows that the dimension of their repulsive cores could change very rapidly as a function of time (because α_{ij}^{MC} depends on the position of atoms that are not directly involved on the given bond), thus requiring the use of a very short simulation step (less than 0.1 fs) to avoid instabilities because of strong repulsive forces that can appear from one time step to the next one. Figure 2.2 shows the effect of α_{ij}^{MC} on the function G (equation 2.8) suggesting that changing α_{ij}^{MC}

in a wide range maintains the size of the repulsive core almost intact. Equation 2.8 satisfies the requirement that the repulsive core does not change with α_{ij}^{MC}.

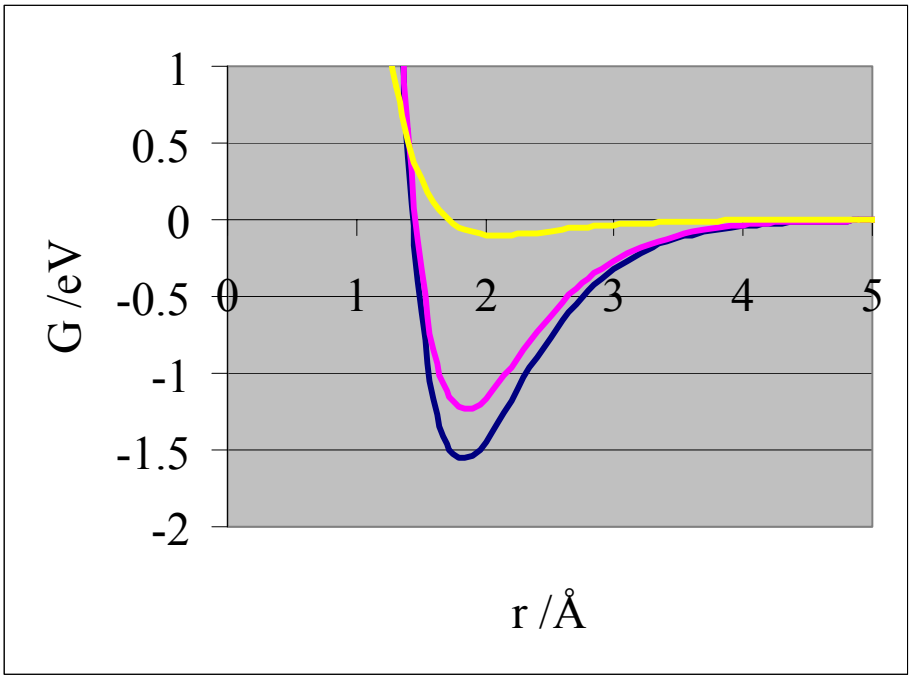

Figure 2.3. Behavior of the G function of Equation 2.8 for values of α_{ij}^{MC} equal 1 (purple line), 0.85 (red line) and 0.15 (black line).[58]

Another requirement for the G function is that it should yield the correct potential shape to account for the case of carbon chains and for carbon bonded to three other carbon atoms.[58] Figures 2.3 and 2.4 show the potential functions (2.8) and (2.16) for α_{ij}^{MC} values of 1, 0.85, and 0.15 corresponding to the cases where the carbon atom j is not bonded to any other carbon atoms, when is bonded to two other carbons, and when is bonded to three other carbon atoms, respectively.

$$G = (\alpha_{ij}^{MC})^{0.8} V^R(r_{ij}) - \left(\alpha_{ij}^{MC}\right)^{1.1} V^A(r_{ij}) \qquad (2.16)$$

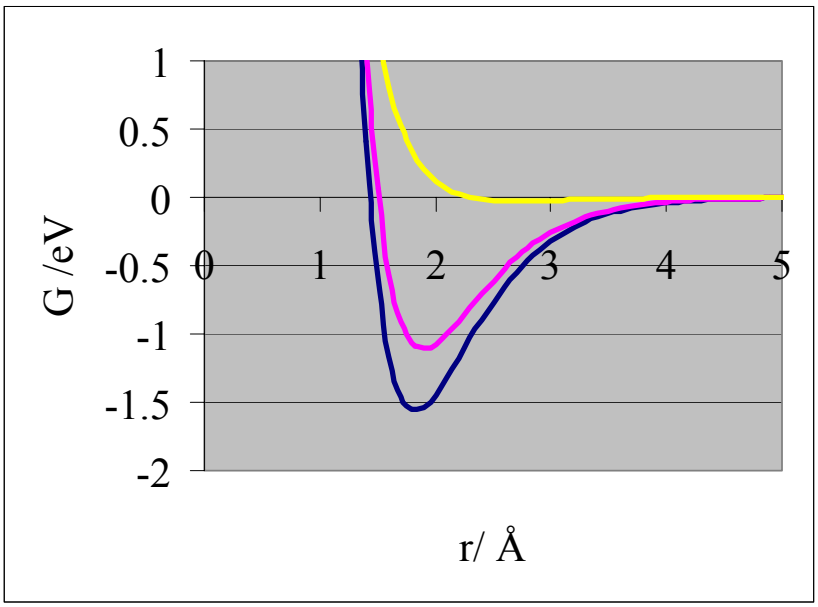

Figure 2.4. Behavior of the G function of Equation 2.16 for values of α_{ij}^{MC} equal 1 (purple line), 0.85 (red line) and 0.15 (black line).[58]

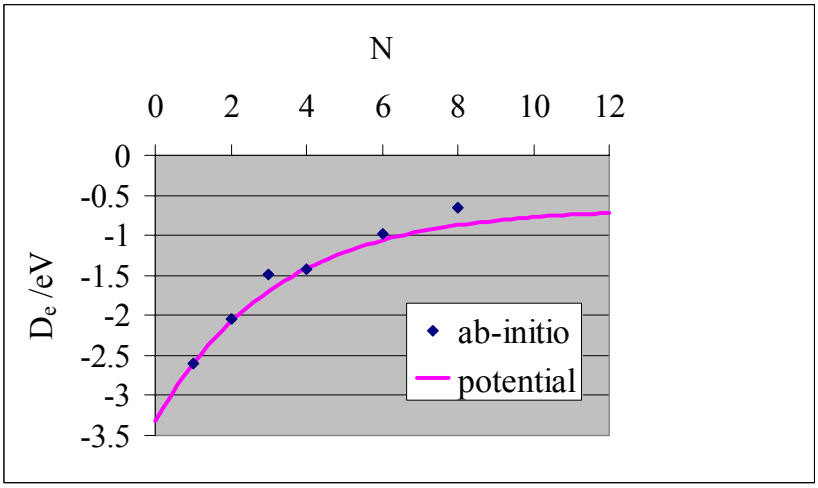

(a)

Figure 2.5. Calculated binding energy (De, in eV) per C-Ni bond (a) and C-Ni bond distance (Re, in Å) (b) as a function of the number of Ni atoms (N) in the clusters CNi_N.[58]

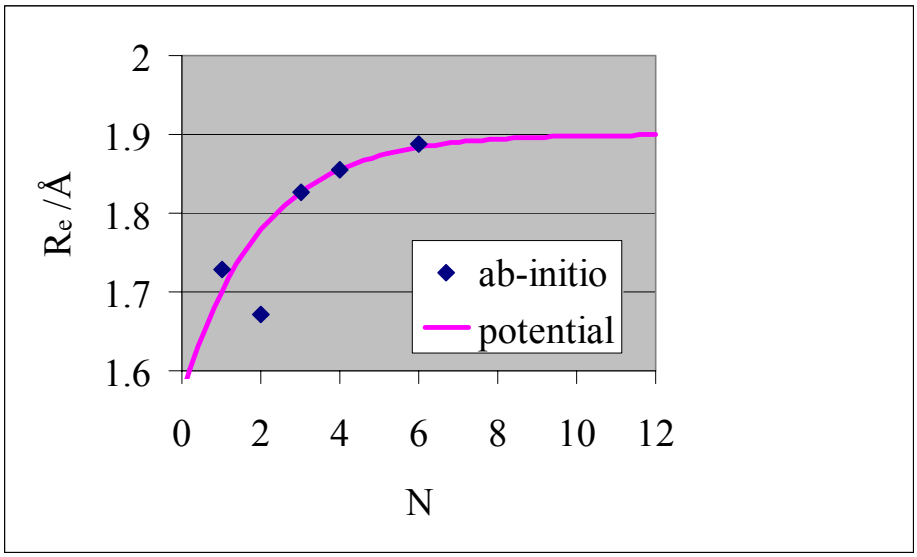

(b)

Figure 2.5. Continued.

At the beginning of the simulation, these functions perform correctly. But after the metal cluster is covered by many carbon chains, these chains do not combine to form fullerene structures as described in the next section when equation 2.16 is used, but it does with equation 2.8. This difference in behavior of the two functions comes from the different equilibrium bond distance of the metal-C bond (the position corresponding to the bottom of the potential well in Figures 2.3 and 2.4) when a carbon atom is bonded to three other carbon atoms. As seen in Figures 2.3 and 2.4, when α_{ij}^{MC} equals 0.85, the equilibrium bond lengths are about 1.8 Å for both functions. But when α_{ij}^{MC} equals 0.15, with equation 2.8 the equilibrium bond length is about 2 Å which is very close to the bond length of 1.95 Å found in the calculated $NiC_{16}H_{10}$ cluster, while with equation 2.16, it is about 2.4 Å.

The potential parameters shown in Table 2.1 were adjusted using equations 2.5 and 2.6 to fit DFT results of several clusters of Ni_N and CNi_N (n=1-4, 6, 8) with high symmetry; the calculated and fitted results are shown in Figure 2.5.[58]

Table 2.1: Parameters for Ni-C potential[58]

β (1/Å)	D_{e1} (eV)	D_{e2} (eV)	C_D	R_{e1} (Å)	R_{e2} (Å)
1.8	0.95	1.65	0.5	1.9	0.2
R_1 (Å)	R_2 (Å)	S	C_R	α_1^{MC}	α_2^{MC}
2.7	3.0	1.3	0.5	~0.8	~0.15
λ	N_1^C	N_2^C	N_3^C	N_4^C	
0.08	~1.5	2.0	~2.5	3.0	

2.1.3 Carbon-carbon potential

For the modeling of the interaction among carbon atoms we start from the reactive empirical bond order (REBO) potential developed by Brenner et al,[57] which is based on the Tersoff[59] and Tersoff-Brenner potentials.[56] Carbon-carbon interactions have been successfully modeled using this potential, defined by a potential function between the C atoms i and j, that includes repulsive and attractive terms V^R and V^A. In our model, we define the C-C energy introducing a function $G\left(\alpha_{ij}^{TB}, V_{ij}^{TB}\right)$ in order to obtain a better description of some particular C-C interactions during the SWCNT growth process in a similar manner as done for the carbon-metal potential.

$$E_{ij}^{CC} = G\left(\alpha_{ij}^{TB}, V_{ij}^{TB}\right) \tag{2.17}$$

$$V_{ij}^{TB} = V^{R}(r_{ij}) - V^{A}(r_{ij}) \tag{2.18}$$

$$V^{R}(r) = f^{c}(r)\left(1 + {}^{Q}\!/_{r}\right)Ae^{-\alpha r} \tag{2.19}$$

$$V^{A}(r) = b_{ij}\left(f^{c}(r)\sum_{n=1,3} B_n e^{-\beta_n r}\right) \tag{2.20}$$

where b_{ij} is an empirical bond order function that depends on the local coordination and bond angles of atoms *i* and *j*.

The weighting factor α_{ij}^{TB} is defined in equations 2.21-2.28[58]

$$\alpha_{ij}^{TB} = \sqrt{\alpha_{1ij}^{TB}\alpha_{2ij}^{TB}} \tag{2.21}$$

$$\alpha_{1ij}^{TB} = \begin{Bmatrix} 1 & (N_{ij}^{M} < N_{1}^{M}) \\ \left(1 + \cos\left(\pi \dfrac{N_{ij}^{M} - N_{1}^{M}}{N_{2}^{M} - N_{1}^{M}}\right)\right)/2 & (N_{1}^{M} < N_{ij}^{M} < N_{2}^{M}) \\ 0.1 & (N_{ij}^{M} > N_{2}^{M}) \end{Bmatrix} \tag{2.22}$$

$$N_{ij}^{M} = \frac{N_{i}^{M} + N_{j}^{M}}{2.0} \tag{2.23}$$

$$N_{i}^{M} = \sum_{metal\ k} f(r_{ik}) \tag{2.24}$$

$$N_{j}^{M} = \sum_{metal\ k} f(r_{jk}) \tag{2.25}$$

$$f(r) = \begin{Bmatrix} 1 & (r < R_1) \\ \left(1 + \cos\left(\pi \dfrac{r - R_1}{R_2 - R_1}\right)\right)/2 & (R_1 < r < R_2) \\ 0 & (r > R_2) \end{Bmatrix} \tag{2.26}$$

$$\alpha_{2ij}^{TB} = \sqrt{\alpha_{2i}^{TB}\alpha_{2j}^{TB}} \tag{2.27}$$

$$\alpha_{2i}^{TB} = \begin{Bmatrix} 1 & (R_i^M < R_1^M) \\ \left(1+\cos\left(\pi\dfrac{R_i^M - R_1^M}{R_2^M - R_1^M}\right)\right)/2 & (R_1^M < R_i^M < R_2^M) \\ 0.1 & (R_i^M > R_2^M) \end{Bmatrix} \tag{2.28}$$

The resulting α_{ij}^{TB} is obtained using the combination rule of Equation 2.21 from the two factors α_{1ij}^{TB} and α_{2ij}^{TB}. α_{1ij}^{TB} describes the fact that the bonding energy between two C atoms inside of the metal cluster is very weak (between 0.05 eV and 0.10 eV [60] or even repulsive), our DFT results on C_2Ni_3 gave a binding energy of 0.44 eV.[58] For comparison the C-C bonding energy according to the original REBO potential is about 6.3 eV. It is clear that the use of the original REBO potential for C atoms inside of the metal cluster would overestimate the strength of such C-C interactions and would yield C structures inside of the metal cluster, that do not exist because of the screening of the C-C interaction by the surrounding metal atoms.

Equation 2.22 describes the transition of α_{1ij}^{TB} from 1.0 to 0.1 when N_{ij}^M (the average number of metal atoms surrounding the two C atoms involved in the C-C interaction) varies from an initial value, N_1^M, to a final value, N_2^M. N_1^M lies between 3 and 4 (3 is the coordination number of a C atom on the surface of the meta cluster; a C atom with coordination number 4 is actually under the surface and has began to feel the screening of the metal atoms over the C-C interactions). N_2^M ranges between 6 and 8 (6 is the

minimum coordination number of C in the bulk metal, 8 is the average coordination number inside a nanoparticle, according to our calculations).[58]

α_{2ij}^{TB} is obtained from the geometric mean of α_{2i}^{TB} and α_{2j}^{TB} (each given by equation 28). α_{2i}^{TB} describes the reactivity of C atoms ranging from $\alpha_{2i}^{TB} = 0.1$ for non reactive C atoms, to $\alpha_{2i}^{TB} = 1.0$ for reactive C atoms. Equation 28 describes the variation of α_{2i}^{TB} with decreasing R_i^M , the distance between the C atom i and its nearest metal atom. α_{2i}^{TB} becomes 1.0 when R_i^M is less than R_1^M (taken as the C-metal bond distance) and in that case the attractive part of the REBO potential is fully activated.

We emphasize that our simulation model for the nanotube growth assumes that the precursor atoms are catalyzed by the metal cluster producing C atoms, and that such reaction is irreversible. In terms of the force field, this means that when α_{2i}^{TB} is equal to 1.0 (i.e. the C atom is "catalyzed") and remains at this value for the rest of the simulation independently of the value of R_i^M . R_2^M , the distance where the C atoms begin to catalyze is approximately the cutoff distance of the C-Metal potential. The actual parameters used in our simulations in Sections 2.2 and 2.3 for equations 2.21-2.28 are given in Table 2.2.

Table 2.2: Parameters for the weighting part of the C-C potential[58]

N_1^M	N_2^M	R_1 (Å)	R_2 (Å)	R_1^M (Å)	R_2^M (Å)
3.5	6.0	2.7	3.0	1.8	2.8

2.2 Molecular dynamics simulations of growth on a floating cluster

2.2.1 Simulation setup

Classical MD simulations are carried out in a periodic box of fixed volume as shown in Figure 2.6, at temperatures in the range of the experimental chemical vapor deposition synthesis,[61] between 800 K and 1300 K. A metal nanoparticle (Ni_{80} or Ni_{48}) is placed in the center of the simulation box. We have chosen Ni as a typical good catalyst for this reaction, to capture the main features of the process. The equations of motion are integrated according to the Verlet algorithm,[62] with a time step of 0.5 fs. The initial configuration of the metal nanoparticle is a local minimum generated via energy minimization of the structure using the Sutton-Chen many-body potential[54,55]. The rest of the volume is occupied with molecules of the precursor gas initially randomly distributed, at a constant density in the range from 0.0001 to 0.0004 molecules/$Å^3$. Assuming ideal gas conditions, such gas densities are equivalent to pressures in the range 14-71 atm for temperatures between 800 and 1300K (much higher than the typical experimental pressures, which are in the range of 1-5 atm).[61] The temperature is kept constant with a simple thermostat where atomic velocities of the precursor phase, the metal cluster, and the catalyzed carbon are separately rescaled to the target temperature at every step of the simulation. It is assumed that as soon as the precursor gas is in contact with the metal particle, it is catalyzed and converted into carbon atoms. The simulation emulates the "non-equilibrium" and "open" state of the synthesis because the metal cluster is under constant gas density, this means that every time one precursor gas

particle is “catalyzed”, i.e., converted into C, one new gas molecule enters into the system.

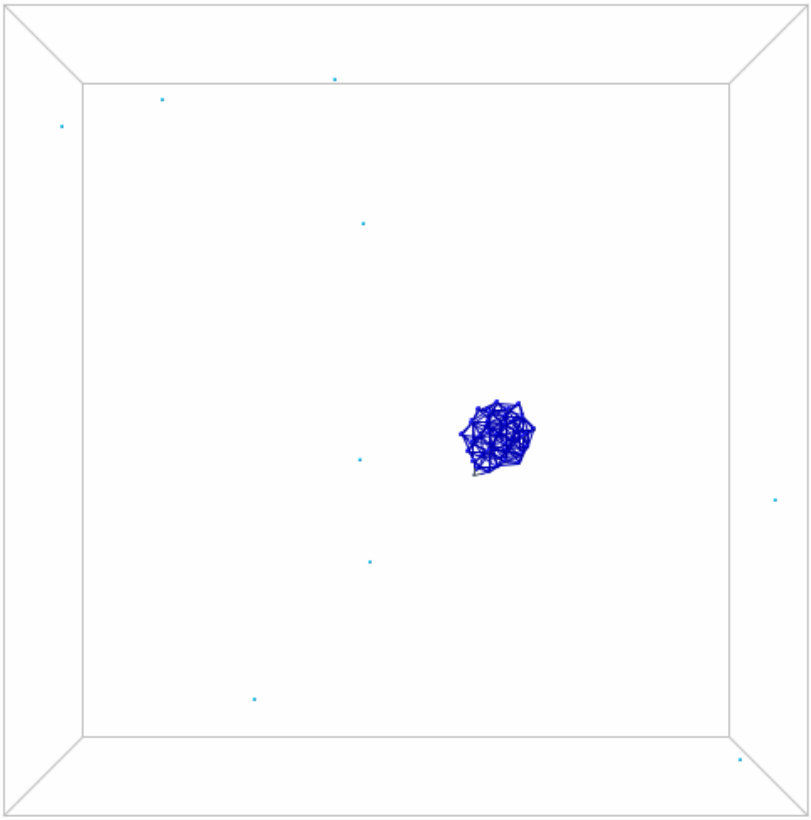

Figure 2.6. Simulation box with floating cluster.[63]

Together with the high density condition, the assumption of instantaneous catalysis greatly accelerates the simulated growth process, making possible to observe the nanotube growth process at the same temperature of the experiment, but in a much shorter time, of only a few nano seconds at the lowest density (0.0001 molecules/Å^3), and even in shorter times at the highest density (0.0004 molecules/Å^3). Possible consequences of this assumption are discussed in Section 2.2.7.

2.2.2 Summary of the observed process

Figure 2.7 shows representative snapshots obtained from the MD trajectories during the growth of the nanotube, which illustrate the main steps: a) Carbon dissolution in the metal cluster, b) Chains appeared on the surface of the metal cluster, c) Fullerene-like structures are formed on the surface, d) A cap develops and a nanotube starts to grow.[63]

Metallic nanoparticles have much lower melting points than bulk. Based on our melting point calculations for transition metal nanoparticles including Pt and Cu-Ni,[64-66] we estimate that the melting point of a Ni particle in the range of 1 nm should be in the order of 1000 K. In addition a gas pressure directed towards its surface has a significant effect on the cluster nanostructure.[67] Thus, in analyzing the process we must consider that the catalyst is a highly mobile and flexible particle. The simulated rate of generation of carbon atoms representing catalysis on the nanocluster surface varies as a function of time and density of the precursor gas, as a consequence of the difficulty for the molecules of the precursor gas to find exposed metal atoms on the increasingly carbon-covered surface of the cluster. At the lowest density (0.0001 molecules/Å^3) C atoms are generated initially at a rate of 1 atom every 6 ps, and the rate is reduced to about 1 atom every 25 ps when a cap is already formed, whereas at the high density (0.0004 molecules/Å^3), a initial steep rate of 1 C atom every 1 ps is reduced to 1 atom every 2 ps when the nanocluster surface becomes about 50% saturated and approximately 1 C atom every 4 ps is generated at the stage of cap growth. In the next sections we expand on each of the steps illustrated in Figure 2.7.

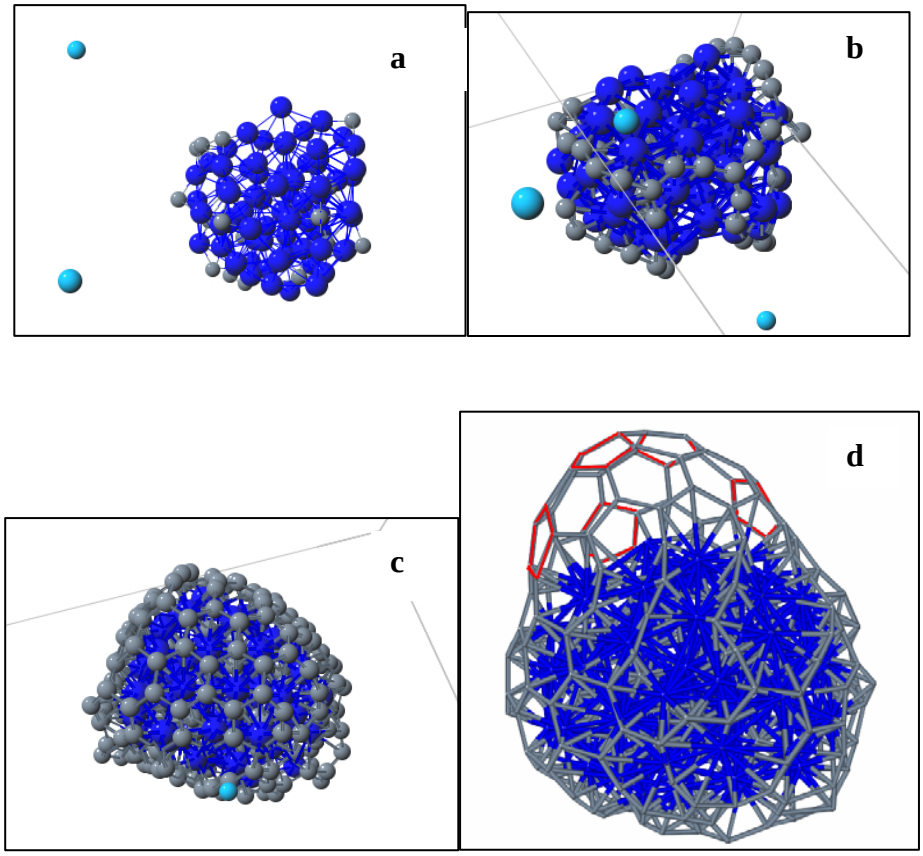

Figure 2.7. Steps of nanotube growth by catalysis of a precursor gas (light blue spheres) on a Ni_{80} nanocluster (dark blue) according to classical MD simulations at 1150 K. [63] After reacting, the precursor gas is transformed into C atoms (grey spheres). (a) Carbon atoms start to dissolve into the metal structure. (b) Chains form on the surface of the metal cluster. (c) Fullerene-type structures appear on the catalyst surface. (d) A cap is formed. Pentagon rings, which are expected to contribute to the cap stability, (see text) are indicated in red.

2.2.3 Carbon dissolution

As shown in Figure 2.7(a), after the precursor atoms are catalyzed, they become C atoms and first dissolve into the metal cluster. Inside the cluster, surrounded by the metal atoms, carbon atoms do not bond to each other, the C-C distances are between 2.0 and 2.8 Å whereas they are 1.4 to 1.6 Å in graphite, and the C-C interaction energy is very weak and slightly repulsive (-0.05 eV to -0.1 eV[63]) in agreement with experimental

results.[60] DFT calculations of C-Ni_n (n = 1-8) clusters yield an average C-Ni energy per bond of ~ 2 eV[63], explaining why carbon atoms prefer to dissolve into the cluster where there is a high probability of coordination with many metal atoms instead of staying on the surface at this stage.[58] But the absorption capacity of the cluster is finite. As shown in Figure 2.8, at the beginning of the simulated process, nearly all the catalyzed carbons dissolve into the cluster (blue curve) while the amount of carbon atoms precipitated on the surface (pink curve) is very small. As the carbon density inside the cluster increases, the rate of dissolution decreases until reaching saturation. Upon saturation no more carbon dissolves, all the new catalyzed carbon precipitates on the surface and the rate of precipitation, estimated by the number of C atoms precipitated per unit time, increases steadily. Inside the cluster, the C atoms are found coordinated to 7~10 Ni atoms on the average[63], which is understood by the liquid state of the metal atoms which act as a solvent under these conditions. [68]

Whether carbon dissolution and deposition on the surface occurs simultaneously or stepwise, is still debated.[69] Precipitation after supersaturation is invoked with reference to temperature-composition bulk phase diagrams for the carbon-metal binary system,[70] but T-composition phase diagrams for C-metal in nanoparticles have not been reported and they should be obviously different since the melting points are much lower and the solubilities of C in metal nanoparticles are higher than in bulk metals. A recent MD simulation study[48] reports supersaturation in nanoparticles as a function of time (Figure 6 in Ding et al's article); however the results are not very convincing because they show

an incorrect temperature dependence: the solubility increases when temperature decreases.

We emphasize that the supersaturation state is a metastable transient state, and therefore it depends on the rate of carbon arrival to the surface. Our results show that: 1) C solubility in the nanoparticle increases as T increases, which is explained by the increase of atomic mobility as the metal particle enters in the proximity of the melting regime, favoring a more open structure which can host a larger amount of C atoms; 2) C dissolution and C deposition on the surface are competing phenomena that for a metal particle floating in the vapor phase are strong functions of density and temperature. At very high densities, C starts depositing on the surface even before the interior of the particle is saturated. As C densities are significantly reduced, C is first dissolved, but after a certain time it starts to be deposited on the surface. The dissolved carbon reaches a saturation value and then remains unchanged; 3) A strong substrate-catalyst interaction can reduce the melting point of the cluster reducing significantly the solubility of C inside the particle (see Section 2.3); 4) Supersaturation is not observed, the reason is our artificially high rate of carbon addition, which is imposed to reduce the computational cost (i.e, to observe nanotube growth in the nanosecond time range, instead of seconds). We do not discard that at a extremely low rate of C addition we might observe the transient supersaturation phenomenon, however, such phenomenon should not be necessarily present in all synthesis processes, and is not a requirement for nanotube growth.

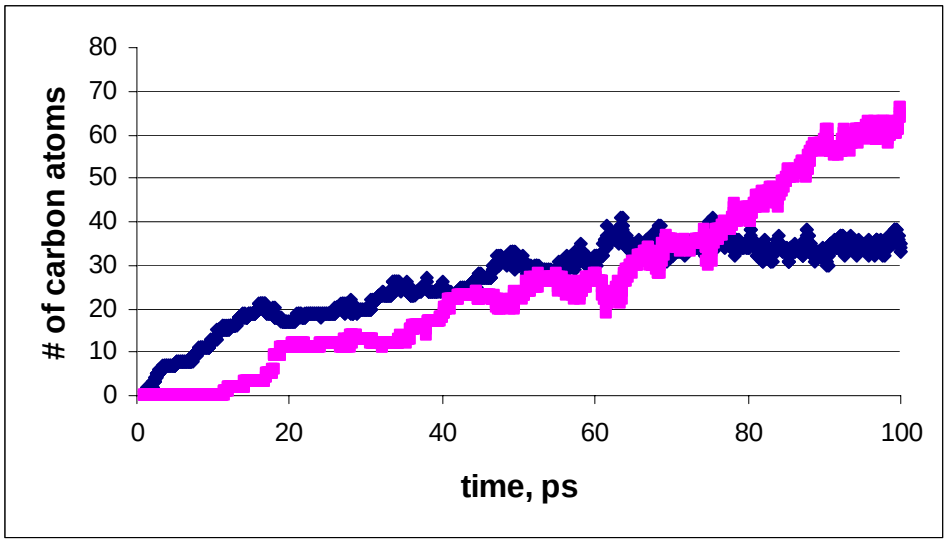

Figure 2.8. Competition between the processes of carbon dissolution (blue) and carbon precipitation (pink).[63] The specific curves correspond to a precursor gas density of 0.0004 molecules/Å^3; qualitatively similar results were obtained at a lower density.

2.2.4 Chains and fullerene formation on the catalyst surface

The C-C interactions on the surface are much stronger than those inside the cluster. After precipitated onto the surface, some carbon atoms form chains as shown in Figure 2.7(b). As time evolves, these chains which are tightly bonded to the metal cluster (~1.0 eV per C-Ni bond),[58] connect to each other forming sp^2 bonds, and fullerene-like structures. The cluster surface (as shown in Figure 2.7(c)), mainly covered by chains and fullerene-like structures, still has some bare areas which ensure that more carbon atoms can be catalyzed. The DFT calculated interaction energy of the fullerene carbon with the metal cluster is about 0.1 eV,[58] much weaker than the interaction between carbon atoms grouped in chains and the metal cluster, explaining the tendency of fullerene to separate from the surface. We note that if the metal particle becomes totally

covered, the nanotube growth stops at this stage. The degree of coverage depends on density and temperature. At sufficiently low densities (0.00001 molecules/Å^3) and temperatures in the order of 1000-1200 K we have observed sustained growth. In such cases, part of the surface is open permitting the catalysis to continue.

2.2.5 Cap formation

Figure 2.7(d) illustrates the lifting of a section of the fullerene-like structure, forming a cap, expected to become a nanotube. This is a complex process because of the fragility of the cap under the given conditions of pressure and temperature and stresses due to geometrical restrictions imposed by the presence of the catalyst. The simulations indicate that a single fault like the presence of two connected pentagonal rings, or one unsaturated carbon in the cap may cause a sustained instability and eventually its breaking.

The next question relates to understanding the description of an ideal stable cap. According to Euler's law, if a cap is composed of five-member and six-member rings only, it should include 6 five-member rings in order to achieve stability.[1] Therefore, how these five-member rings are distributed over the hemisphere may determine the diameter and chirality of the nanotube hence formed. According to the isolated pentagon rule, the maximum possible separation of the five-member rings results in the lowest energy of the structure.[8] It is often assumed that in a stable cap, no two five-member rings should be connected.[9] Because of the presence of the five-member rings, there is a strong stress associated with the cap curvature which makes difficult the process of forming an ideal cap. Thus, caps are highly ordered regions but more difficult to achieve stability when

compared to the straight portion of the nanotube. That is why the process of cap formation and breaking is a frequent event that takes place continuously on the simulated synthesis process. In fact, the formation of an ideal cap is a rare event, and we discuss in a later section the conditions for observing such event in the simulations.

2.2.6 Correlations between metal cluster size and cap diameter

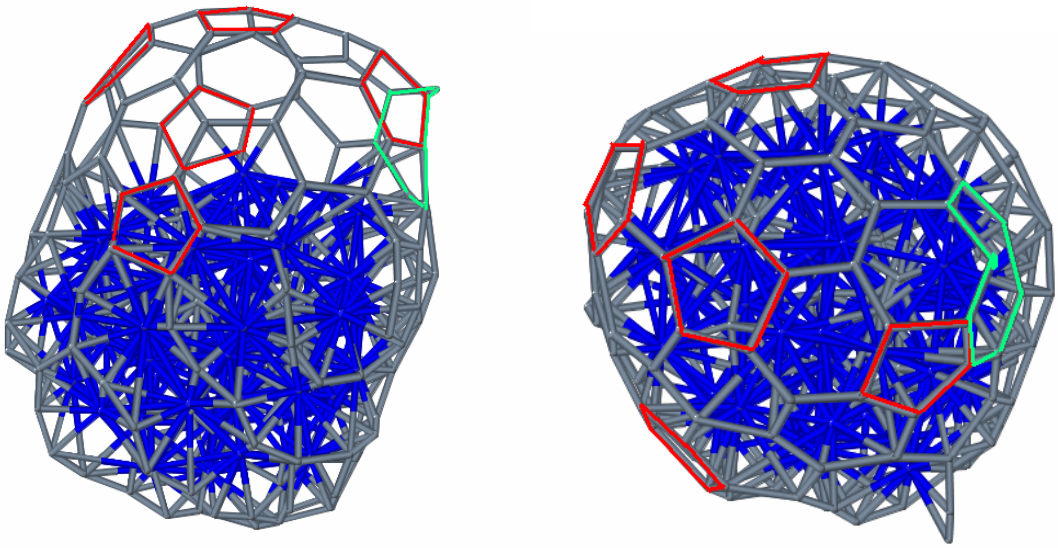

Figure 2.9. Cap formed on Ni_{48} at 1200 K. Five-member rings are indicated in red, and possible failure regions are shown in green (left: Side view, right: Top view).[63]

To investigate the size effect of the nanocatalyst, considering that the range of SWNT diameters is within 0.7 to 1 nm,[4] we tested two cluster sizes: Ni_{48} (~ 0.7 to 0.9 nm diameter) and Ni_{80}(~ 0.9 to 1.2 nm diameter). The caps obtained in two simulations for these clusters are shown in Figures 2.9 and 2.10 respectively. In the case of Ni_{48} (Figure 2.9), the diameters of the cap and that of the cluster are nearly the same, and they

were connected to each other smoothly. In the case shown however, there is a carbon atom with a dangling bond, which eventually causes cap breaking.

Figure 2.10(a) shows a cap formed on a larger cluster, Ni_{80}, containing 5 five-member rings. Geometrically, if a cap approximates a perfect hemisphere (or half of an ellipsoid) the edges on opposite sides of the cap should be nearly parallel to each other. In the simulations, the edges were found strongly attached to the cluster, forcing the cap to grow under an angular stress (Figure 2.10(b)), which eventually causes the rupture of this cap although structurally it was perfect. Hence we propose that more stable caps have a higher probability of formation when their diameter is almost the same of that of the catalyst cluster, reducing the stress at the edges, in agreement with the experimental result[52] that nanotubes produced have nearly the same diameter of the average catalyst cluster.

We have exhaustively explored the temperature range from 1100 K to 1250 K, and in all cases we were able to observe caps forming, breaking, and forming again, such as those illustrated in Figures 2.9 and 2.10, obtained at a density of 0.0004 molecules/$Å^3$ in a time scale shorter than a nanosecond. Similar results were obtained at a density of 0.0001 molecules/$Å^3$, in time frames from 2 to 3 nanoseconds.

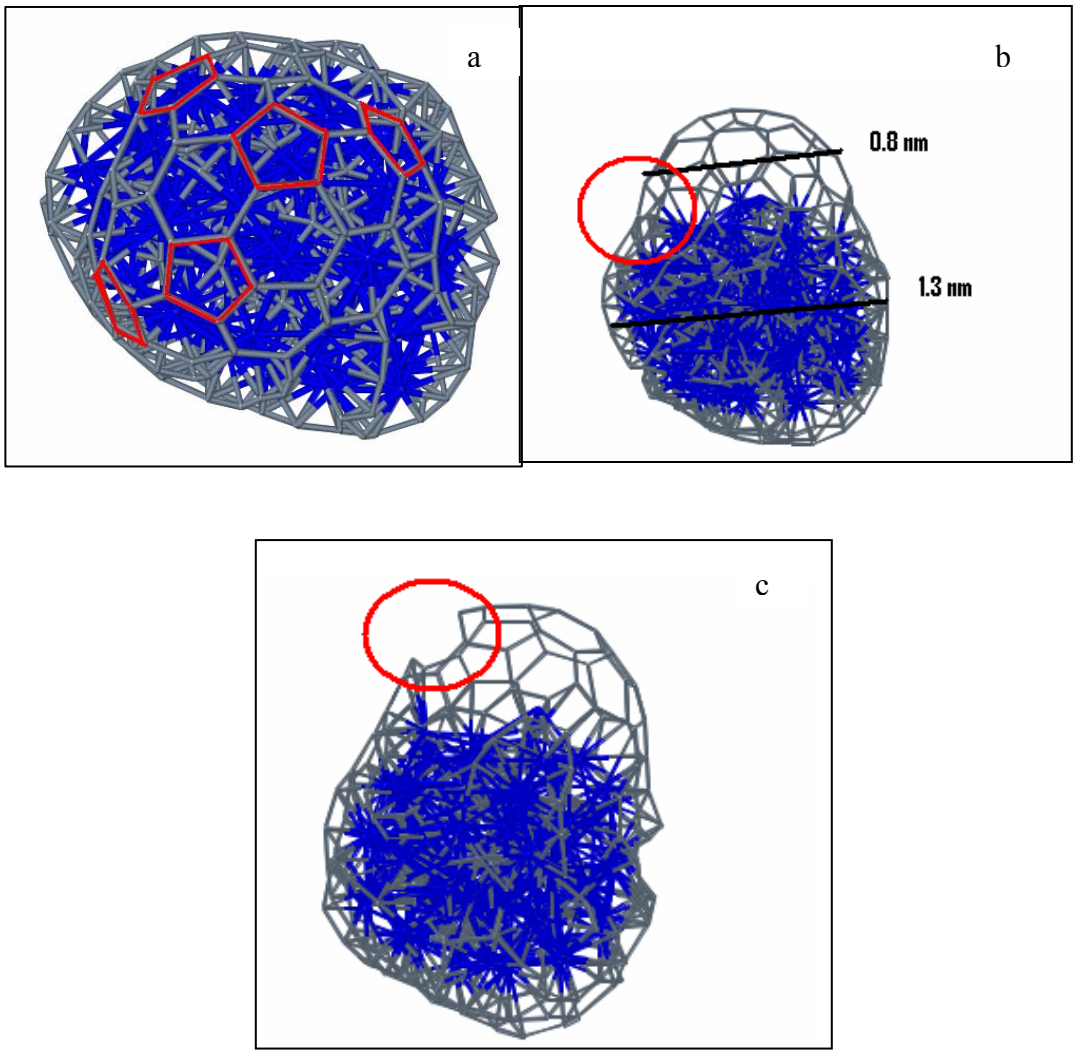

Figure 2.10. Cap formed on Ni_{80} at 1150 K. (a) Side view. (b) Top view. (c) Cap is broken.[63]

2.2.7 Discussion about temperature and time scale

Simulations done at 1023 K, the best working temperature used in the actual experimental synthesis,[52] indicated the formation of very unstable caps, showing many symptoms of failure such as carbon atoms with dangling bonds, and neighboring pentagon rings. But much more stable caps were found at a slightly higher temperature

(1150-1200 K). Taken in absolute terms, this is actually a minor discrepancy with the experiments, the largest one being the vastly different time scales in the actual and the simulated process. Our assumption of instantaneous catalysis makes the growth of the nanotube to be feasible in a nanosecond time scale, whereas it takes seconds in the actual process. Within such a short simulated synthesis time, each of the stages is accelerated. For example, it is known that fullerene structures need long times to acquire their stable structure. To address this problem, a common simulation strategy is to anneal the system starting with a temperature much higher than those used in the experimental synthesis. At such temperature, it is possible to provide a further fictitious acceleration to convert time scale of events from seconds to nanoseconds. For example, imperfect fullerenes annealed at 2500 K for 200 ns become perfect C_{60} structures, whereas they are obtained at ~1000 K in experiments.[71] Such annealing simulation technique is not useful for our system; at that temperature, the metal cluster is totally melted and the high mobility of the metal atoms at those conditions would provide further unwanted distortions.

2.3 Growth of SWCNTs on a supported catalyst nanocluster

In this section, a similar simulation system as described in Section 2.2.1 is used except that here the metal cluster is attached to a substrate. For carbon atoms, this substrate behaves like a hard wall: as soon as carbon atoms approach the substrate, it will be repulsed to the opposite direction. The strength of interactions between the metal atoms and atoms in substrate can be adjusted as needed.

Significant effort has been devoted to study the growth of SWCNTs on metal clusters floating in a vapor of the precursor gas, using classical MD simulations.[39,48,49,63]

In all these simulations it is found that carbon first dissolves into the metal cluster, and after saturation or oversaturation of the C inside the cluster, C precipitates on the surface forming various structures ending with the formation of a cap which evolves separating from the cluster and forming a single-wall carbon nanotube. In all cases, the simulated nanotubes are closed by the cap in one end and attached to the metal cluster in the other end, just like those observed in base growth mode.[4]

We studied the growth of SWCNT on supported catalyst cluster and found that the growth process on a weakly interacting substrate is not significantly altered from that of a nanocatalyst floating in a vapor. However, simulations done for a cluster deposited on a strongly interacting substrate indicate that such interaction modifies the stages of nucleation and growth with respect to those found in identical metal clusters floating in a vapor phase.

The most significant features are illustrated by snapshots shown in Figure 2.11. The strong substrate/cluster interaction favors a more rigid cluster structure which modifies the initial stage of C dissolution. Even though C still dissolves into the cluster, the amount is lower than that obtained when the metal cluster is completely unrestrained.[72]

Note that the effect is similar to a reduction in temperature. The related literature usually discusses the need of an initial supersaturation,[70] defined as the ratio of the actual amount of C dissolved in the metal to the equilibrium concentration. However, both the actual and the equilibrium C concentrations are functions of the metal particle size, temperature, and pressure, and the simultaneous dissolution and deposition of C on the surface cannot be discarded.[69] In fact, supersaturation is a metastable transient

phenomenon, which would be difficult to detect experimentally and also by simulations, especially if the simulated rate of C addition is artificially high. Under the effect of a strong surface-metal cluster interaction, we do not observe supersaturation, and in addition we observe simultaneous C dissolution and deposition on the surface.[72] Thus, C deposits on the surface at the same time that some atoms dissolve in the interior, initially forming chains that then interact with each other forming sp^2 polygons, and finally fullerene-type structures partially cover the surface, and a cap is formed that leads to the nanotube growth. At the conditions of pressure and temperature shown in Figure 2.11, the nanotube formed has several imperfections and those are most likely due to the fast rate of carbon addition artificially imposed by our simulations. [72]

Recently published ab initio molecular dynamics simulations[73] basically agree with our findings. In the ab initio MD study,[73] the metal cluster is kept fixed, and hydrogen atoms are added to the bottom part of the metal structure to emulate the effect of the substrate. It is found that a cap is formed without carbon atoms being dissolved in the cluster interior, as expected from our discussion for a strongly interactive substrate that causes the cluster to adopt a rigid structure avoiding the penetration of C atoms.

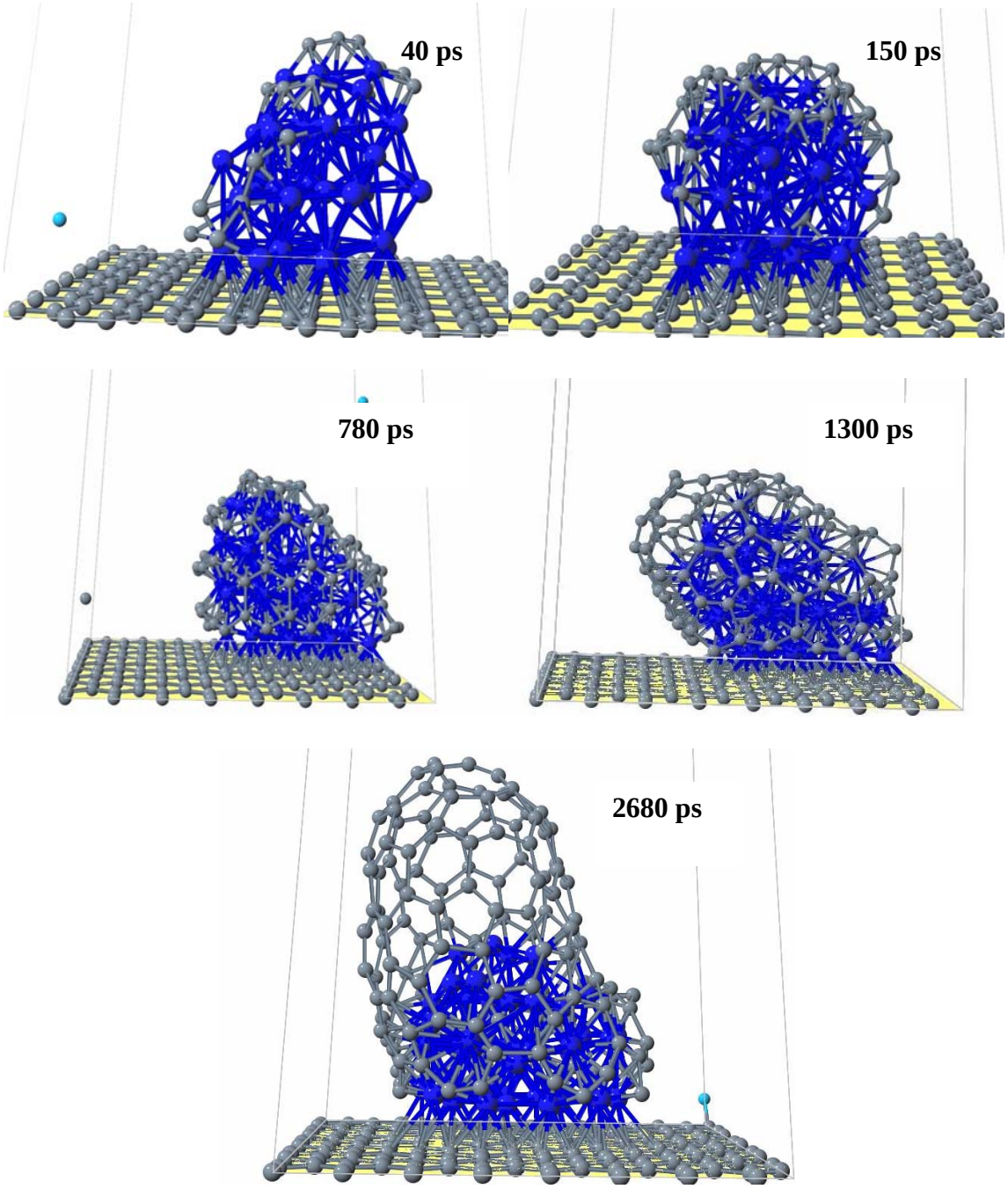

Figure 2.11. Time evolution of nanotube growth calculated by classical MD simulations using a reactive force field.[72] Ni_{48} is interacting with a substrate via a LJ potential, the density of precursor atoms is 0.0002 molecules/Å^3, and the temperature is 1023 K. Initially the C atoms either dissolve in the cluster or deposit on the surface, then chains are formed, followed by fullerene structures, and finally a cap is formed that develops into the nanotube.

2.4 Conclusions

A reactive force field is developed to describe the interactions in SWCNT growth process by CVD methods.

Classical MD simulations are used to emulate a catalyzed synthesis process of SWCNTs. It is assumed that instantaneous catalysis of a precursor gas takes place as this species gets in contact with the nanocatalyst surface. Analyses of the time evolution of the system illustrate that the C atoms product from the catalyzed reaction undergo a series of steps including carbon dissolution inside the metal cluster, carbon precipitation on the surface as chains and fullerene-type structures, and cap growth, ending with formation of a single-wall carbon nanotube.

There is a subtle balance among the C-C, and C-Ni interactions, which determines at each temperature the degree of C dissolution inside the metal nanocluster and also the type of carbon structures formed on the surface. The most crucial stage is the formation of a stable cap that eventually separates from the cluster and growths as a single-wall carbon nanotube. From simulation results indicating that a mismatch between the cap and the cluster diameters would cause additional stresses inducing cap breaking, we infer that SWCNTs produced most likely will have the same diameter as the originating cluster.

When the catalyst cluster is attached to a substrate, the growth process can be affected by the interaction between the cluster and the substrate. Under strong interaction, the shape of the cluster is more rigid and the amount of carbon can be dissolved into the cluster will decrease.

3. DENSITY FUNCTIONAL THEORY CALCULATIONS OF SWCNTS*

According to Molecular Dynamics simulations in Section 2, the selective growth should happen either in step 4, where the formation of certain caps are thermodynamically or kinetically more favorable than the others, or in step 5, where the growth of certain nanotubes are more favorable than the others. If the selective growth happens in step 5, it could be the result of total effects determined by several factors including but not limited to the growth conditions of pressure and temperature, the physical and chemical properties of different nanotubes, the substrate and the metal catalyst, and the interaction of the nanotube with the metal cluster. It is impossible to include all these effects in one single simulation model. In spite of the complexity of the selectivity mechanism, the nanotube physical and chemical properties intrinsic to specific chiralities, which will also determine the interaction of nanotubes with the metal

---

cluster, must at least play an important role on it. In this section we will study properties of nanotubes with different chirality. We will study the shape and energy of the frontier HUMO and LUMO orbitals, the adsorption energy to attach a C_2 radical, as well as local aromatic properties of rings in nanotube.

3.1 Methodology

3.1.1 Geometry of SWCNTs

To design our computational model, we first studied the distribution of electronic charges for a simple cap terminated by hydrogen atoms at its open end, and for a cap where the carbon atoms at the open end are bonded to Ni atoms, as shown in Figure 3.1.

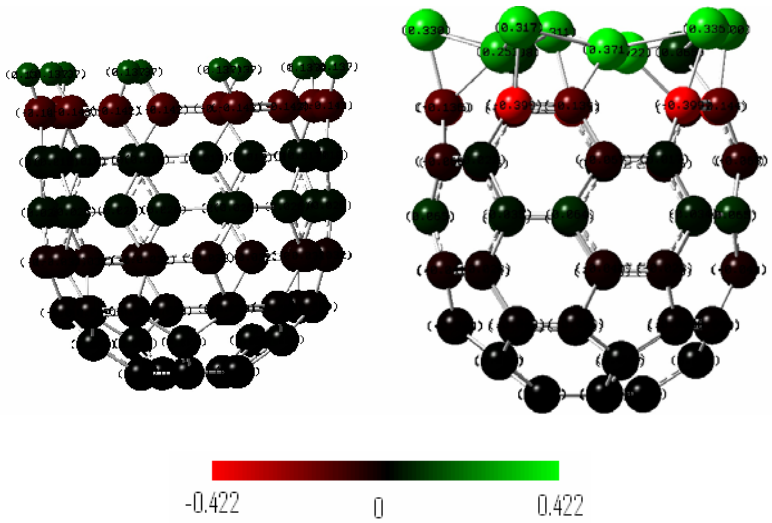

(a) cap(5,5) + 10 H (b) cap(5,5) + 10 Ni

Figure 3.1. Charge distribution in the cap atoms (the color of each atom represents its charge as shown in the scale).[74]

The distribution of electronic charge was determined after geometry optimizations using density functional theory B3LYP method and 6-31G basis set. In both cases it was found that the carbon atoms at the open end are negatively charged, that is to say, both Ni atoms and H atoms act as electron donors.[74]

Although the effect of the catalyst metal cluster on the growth of nanotube is quite complex, here we assume that one of the roles of the metal atoms is to provide electrons to the cap in the same way as hydrogen atoms do.

Based on the above simplification, two kinds of nanotube are studied here. Those with one end open and the other end closed by a cap structure, named one-end-closed nanotube (Figure 3.2(a)) and those with both ends open (Figure 3.2(b)).

The caps are half fullerenes following the isolated pentagon rule[8] and according to this rule, there is only one possible IPR cap structure for nanotubes (5, 5), (6, 5) and (9, 1) respectively, 3 IPR caps for nanotube (8, 3) and 14 IPR caps for nanotube (7, 5).[9,10] All the three kinds of caps for nanotube (8, 3) are studied in this work but only one kind for nanotube (7, 5) is discussed. All these caps studied in this work are shown in Figure 3.3. At the open ends, the dangling bonds of carbon atoms are bonded to hydrogen atoms. We terminated the open ends of nanotubes in a way that fewest carbon atoms are bonded with H atoms. As shown in Figure 3.4, the open ends of nanotube (5, 5), nanotube (6, 5), nanotube (7, 5) and nanotube (8, 3) are parallel or nearly parallel to the vector $\vec{i} + \vec{j}$ while that of nanotube (9, 1) is parallel to vector $\vec{i} - \vec{j}$ where the vectors are defined in Figure 3.5.

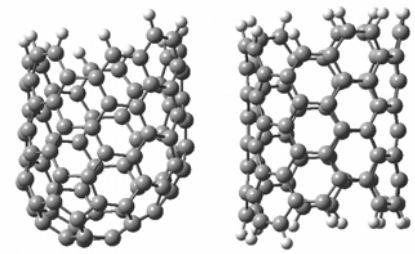

(a) (b)

Figure 3.2. Schematic of two kinds of nanotube studied in this work. ((a): one-end-closed nanotube; (b): two ends open nanotube.)

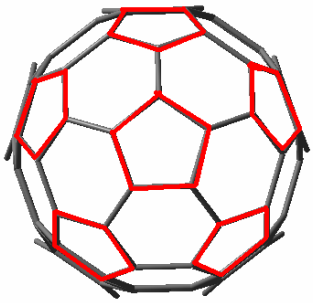

(a) cap (5, 5)

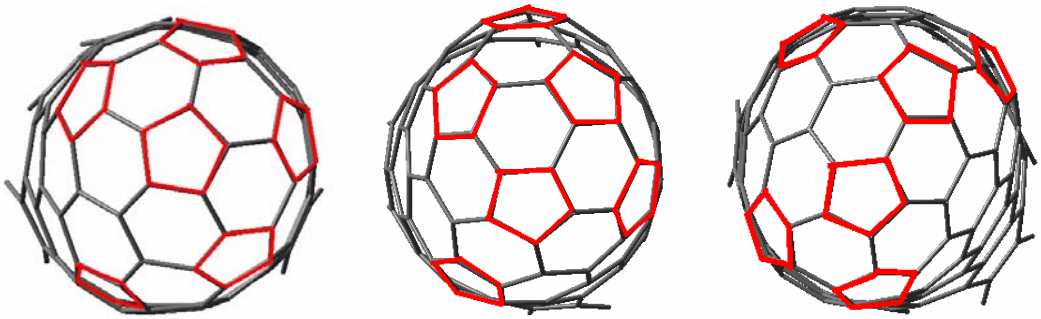

(b) cap (6, 5) (c) cap (9, 1) (d) cap (7, 5)

Figure 3.3. Cap structures studied in this work.

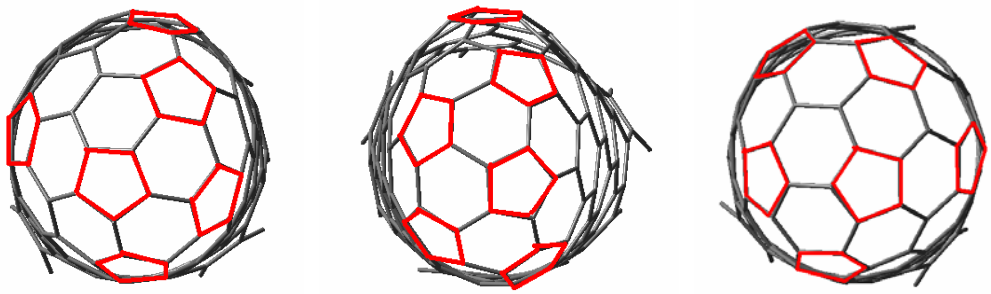

(e) Cap (8, 3) I (f) cap (8, 3) II (g) cap (8, 3) III

Figure 3.3. Continued.

In order to study aromatic properties of the rings in the nanotubes, we have to first label those rings. We use two different ways to label the rings in the nanotube, one way is to label the rings from the open end, namely we label the ring at the furthest end as ring 1 and count along the direction of the open end, $\vec{i}+\vec{j}$ or $\vec{i}-\vec{j}$ as shown in Figure 3.4. For one-end-closed nanotube, we also use another way to label the rings: labeling the rings in the opposite direction, from closed end to open end along the vector $\vec{i}+\vec{j}$ or $\vec{i}-\vec{j}$. Since there is only one series of rings in nanotube (5, 5), (6, 5) and (9, 1), the ring labeled N when labeled from the open end will be labeled N1- N when labeled from the closed end, where N1 is the number of rings in the nanotube and can be directly calculated from the number of carbon atoms (N2) by equation N1=(N2-M)/2 with M equaling 8 for nanotube (5, 5) and nanotube (9, 1), 9 for nanotube (6, 5) and 10 for nanotube (7, 5). The chiral vector of nanotube (7, 5) is not close to $\vec{i}-\vec{j}$ or $\vec{i}+\vec{j}$, it is not possible to label them as one series of rings. So we label the rings in two series, as

shown in Figure 3.4(d). The chiral vector of nanotube (8, 3) is even further away from $\vec{i} + \vec{j}$, so we may need to label the rings in 5 series (first rings of each of these series are labeled blue in Figure 3.4(e)) and in such case, it is very hard to observe any trend in short tubes since rings in each series will be much less than the other nanotubes. So we did not label the rings or discuss the NICS of rings other than the new formed ring at open end for nanotube (8, 3).

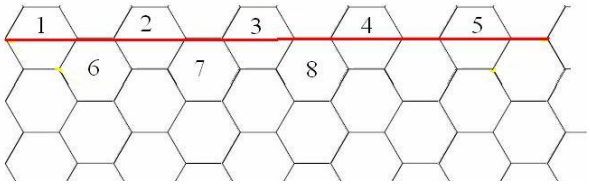

(a) Nanotube (5, 5)

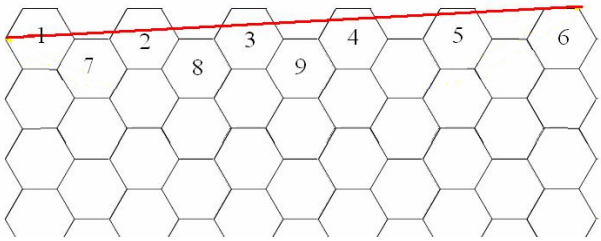

(b) Nanotube (6, 5)

Figure 3.4. Method of cutting the open end of nanotube and labeling rings from open end (red line: roll-up vector).

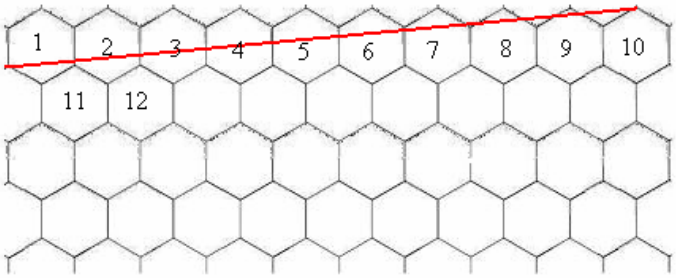

(c) Nanotube (9, 1)

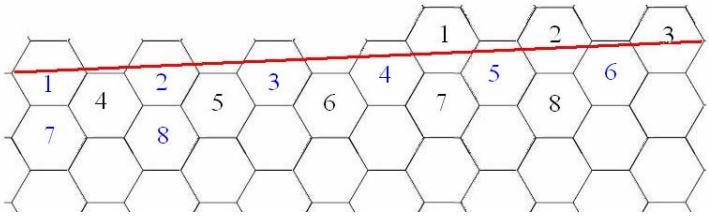

(d) Nanotube (7, 5)
(rings labeled blue: series A, rings labeled black: series B)

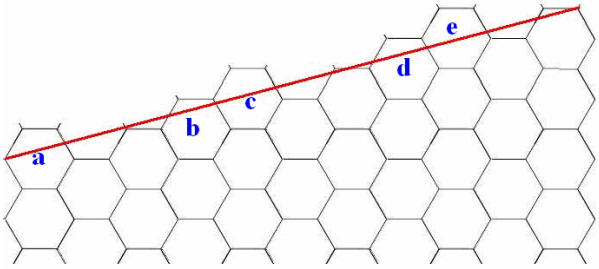

(e) nanotube (8, 3)
(first rings of each of 5 series are labeled by blue letter)

Figure 3.4. Continued.

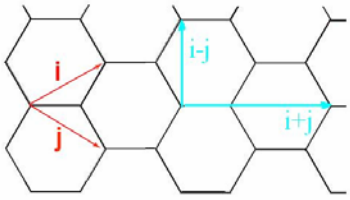

Figure 3.5. Basic lattice vectors.[75]

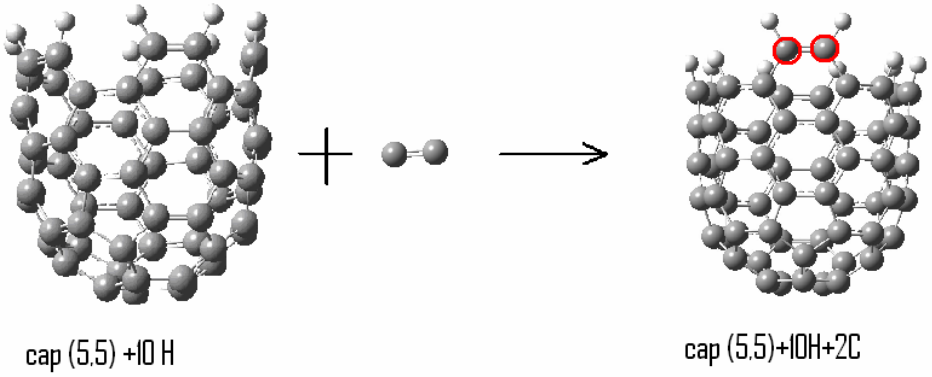

Figure 3.6. Adding C2 to one-end-closed nanotube (5, 5).[74]

We keep adding C_2 at the open end in such a way that the shape of the open end does not change except in armchair nanotubes (Figure 3.6). In nanotube (9, 1) and nanotube (6, 5), new rings are built before the first ring at the open end. In nanotube (7, 5), new rings are built before the first ring of the two series alternatively. In nanotube (8, 3), new rings are built before the first ring of the five series in turn as shown in Figure 3.7.

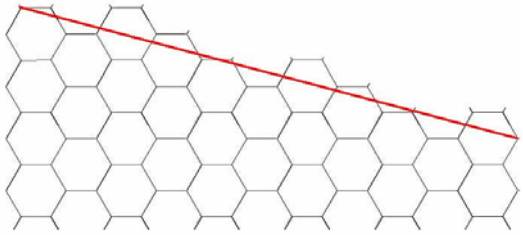

(a)

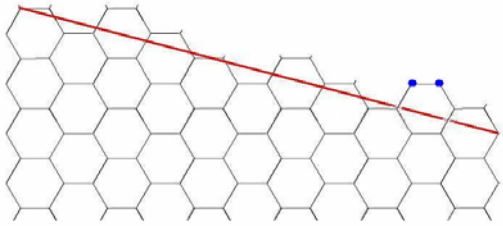

(b)

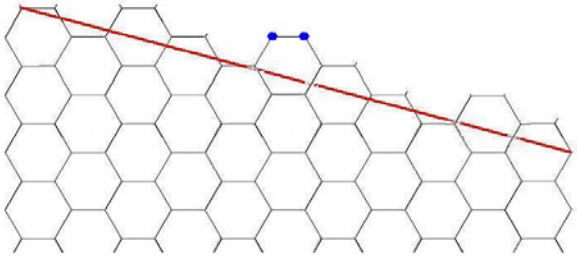

(c)

Figure 3.7. Adding C2 at the open end of nanotube (8, 3) (red line: roll-up vector, new added carbon atoms are marked blue).[76]

The energy change of this reaction for different caps is shown by equation 3.1.

$$\Delta E = E_{new\_cap} - E_{cap} - E_{C_2} \tag{3.1}$$

This equation implies that the H atoms are displaced by the C atoms, but the displacement energy is not included in our calculations. The process is illustrated in Figures 3.6 and 3.7.

3.1.2 Selection of basic set

NICS values are only somewhat sensitive to the basis set and 6-31+g* is recommended where it is possible.[14] We optimized a short one-end-closed nanotube (5, 5) with just 60 carbons atoms with 6-31+g* and calculated the NICS values of the rings with the same basis set and compared the calculation result with 6-31g basis set. Like reported[14,16], even though the NICS values of each of the rings shows some variation, the relative values of the different rings show the same trend which allows us to compare the relative NICS of the rings. Zurek et al have computed the NMR chemical shift of C13 in nanotube (9, 0) showing good agreement to experimental results.[77] Though limited by calculation resources and time, we can not carry out calculation on a big system to mimic the real nanotube like they did, our calculation on a short open end nanotube (9, 0) with 90 carbon atoms (geometry shown in Figure 3.8(a)) with 6-31g basis set have good agreement with their results on the same structure but with a much more expensive basis set, as shown in Figure 3.8(b). Based on all these calculations, we believe the 6-31g is big enough for us to compare NICS of different rings.

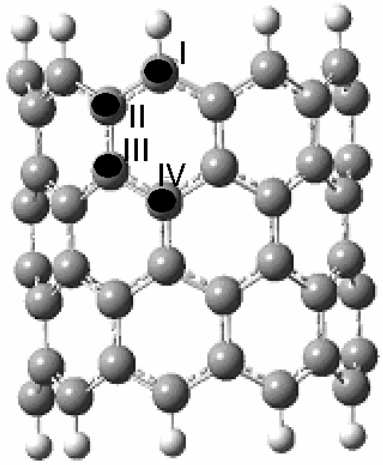

(a) Geometry

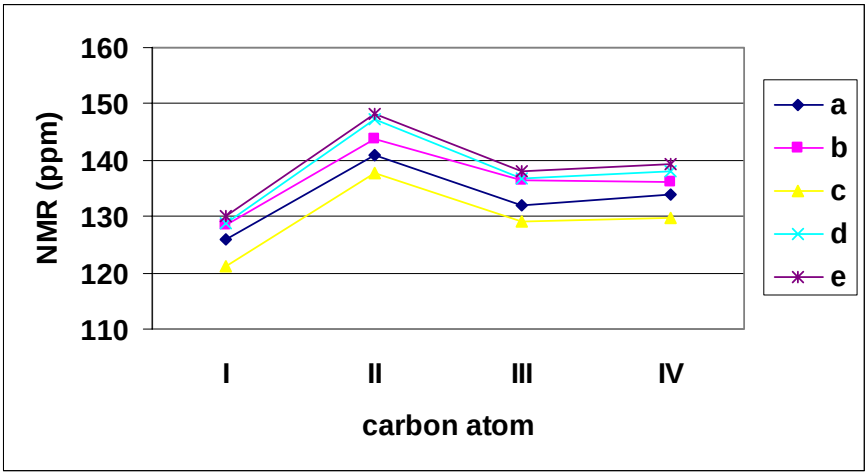

(b) C13 chemical shift

Figure 3.8. Geometry and chemical shift of C13 of open-end nanotube (9, 0) with 90 carbon atoms (basis set used: a: 6-31g[75], b[77]: dz, c[77]:dzp, d[77]:tzp, e[77]:tz2p).

3.1.3 Selection of NICS calculation points

In order to find the best location of NICS points to represent the aromatic properties of a ring, we scanned the NICS value of several rings in a few representative nanotubes

with different chiral vectors and different lengths. The geometry center of each ring is set as the origin. And the normal of the least-squares plane of the ring is set as the scan axes (blue line in Figure 3.9(a)) with the positive direction pointing outside the tube. As shown in Figure 3.9(b), in the negative direction, that is inside the tube, as the distance from the center increases, the NICS value becomes stable. Considering the long distance to the ring, this chemical shift could not result from shielding of the current in the ring, but from shielding of current in the tube. In the positive direction, which is outside the tube, as the distance from the center increases, the NICS value will approach zero, which means the shielding effect vanished there. In this side, the NICS curve can be divided into three kinds: those negative with a minimum at about 1 Å, those positive decreasing with distance and those having a small value, characteristic of aromatic, antiaromatic and nonaromatic rings respectively. So we chose the NICS value at 1 Å away from the center in the positive direction (NICS(+1)) to represent the performance of the ring. And the stable value in the negative direction is chosen to represent the shielding effect of the whole tube.

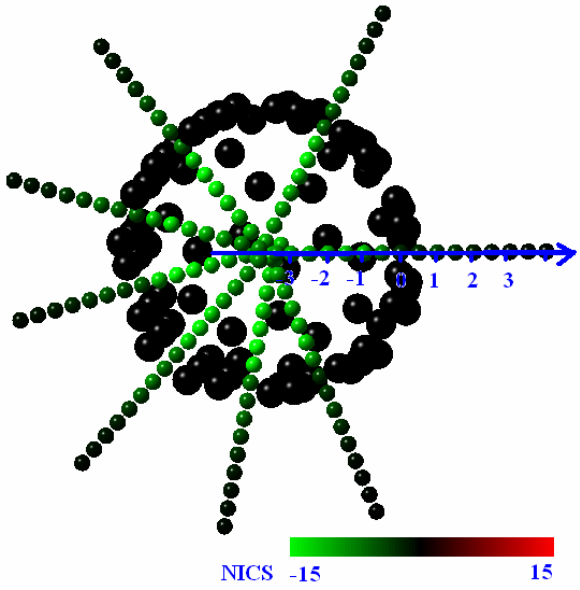

(a)

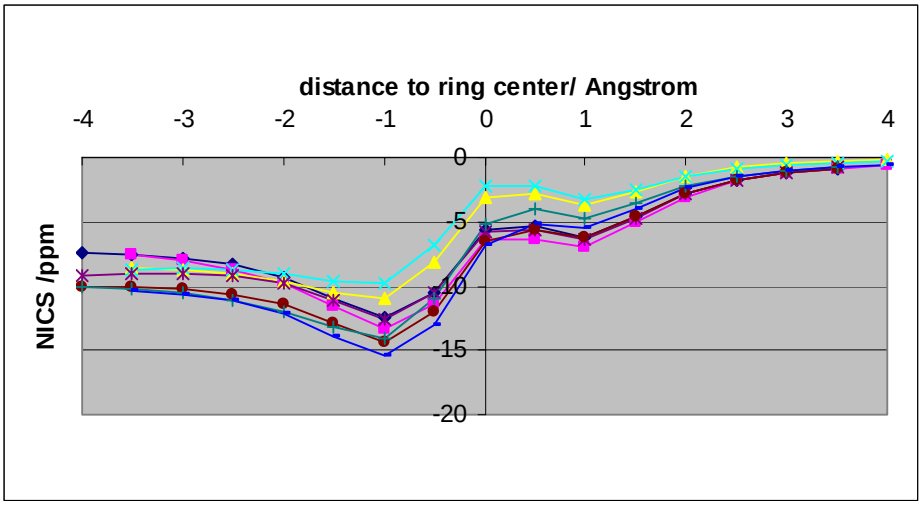

(b)

Figure 3.9. NICS scan. ((a): cross section view of nanotube with NICS of each tested points represented by colors as shown in the scale, (b): NICS value of each point on the scan axis.)

3.2 Properties of one-end-closed nanotubes with different chirality

Classical molecular dynamics simulations in Section 2 suggested that when a cap starts growing into a nanotube, short carbon chains or branched chains react with the open edge of the growing cap, forming carbon rings that would become part of the cap if the cap is stable; otherwise they would break into shorter chains that would try to form new rings again. Thus the growth of the cap is a very complex process with numerous possibilities. Yet in this section we just discuss the simplest reaction path: a carbon diatom reacts with the cap, contributing to the cap growth. We studied the change of this reaction energy with tube length for one-end-closed nanotubes with different chirality. And since armchair nanotubes are highly symmetric, in section 3.2.2, changes of reaction energy of armchair nanotube with tube length are explained with relation to the shape and energy of the HOMO and LUMO orbitals. In section 3.2.3, NICS is used to study the aromatic properties of the rings in one-end-closed nanotube with different chiralities. And the NICS of the new formed rings at the open end is compared with its formation energy.

3.2.1 Reaction energy of forming one more ring at the open end

Changes of the reaction energy with the number of carbon atoms in the tube is studied for one-end-closed nanotube with different chiralities. As shown in Figure 3.10, the reaction energy of nanotubes (5, 5), (6, 6) and (7, 5) changes periodically with increasing the number of carbon atoms. For nanotubes (6, 5) and (9, 1) when the number of carbon atoms is rather small, it changes irregularly, but after the number of carbon

atoms reaches a certain value, the reaction energy also remains constant with the increasing of number of carbon atoms. We choose to ignore the small binding energy occurring in short (6, 5) and (9, 1) tubes because it is a one-time event and it is possible that a fraction of (6, 5) caps with 65 carbon atoms (Figure 3.10) can react with C_2 despite the relatively small reaction energy (-7.9eV).[74] But for caps (5, 5), because the reaction energy changes periodically, the growth limitation will repeat periodically, thus reducing the chances of growing long (5, 5) nanotubes.

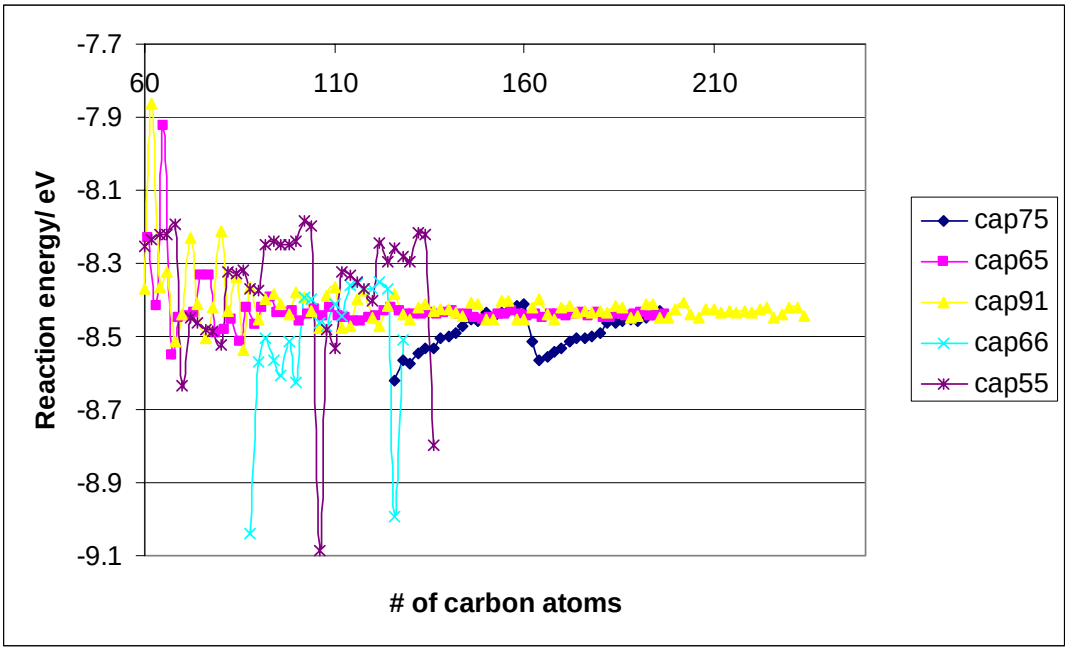

Figure 3.10. Changes of reaction energy with the number of carbon atoms in the tube for one-end-closed nanotube with different chiralities.

In order to estimate the ability to grow of different caps, we compared the reaction energy of one period of cap-ended nanotubes (5, 5) (6, 6) and (7, 5) with the stable reaction energy of nanotube (6, 5) and (9, 1) as shown in Table 3.1. The average value of

the adsorption energy increases with the nanotube diameter which is due to the effect of the reduction of the curvature energy as the diameter increases. However, the adsorption energy of cap-ended nanotubes (5, 5) and (6, 6) shows large variations when the number of carbon atoms in the nanotube increases. Therefore for a particular type of nanotube, the smallest value of the reaction energy (weakest adsorption energy) may be taken as an indicator of the difficulty of the nanotube to grow, since the model reaction to adsorb one C_2 radical could be thought as the rate determining step in a series of possible growth reactions. The weakest adsorption energy of cap (5, 5) is much lower than that of the others, it is suggested that the reasons why nanotube (5, 5) is not found in the experiment product of CoMoCAT process may be related to this.

Table 3.1: Adsorption energy to incorporate a C2 radical to different nanotubes

nanotube	nanotube diameter/nm	average value/ eV	adsorption energy/ eV
(5, 5)	**0.687**	**-8.36**	**-8.23~ -9.08**
(6, 5)	**0.757**	**-8.43**	**-8.39~ -8.44**
(9, 1)	**0.757**	**-8.43**	**-8.38~ -8.44**
(6, 6)	**0.824**	**-8.47**	**-8.35~ -9.03**
(7, 5)	**0.829**	**-8.49**	**-8.41~ -8.56**

3.2.2 Periodic changes in reaction energies of armchair nanotubes

Since armchair nanotubes are highly symmetric, it is possible to explain the changes of reaction energy with the shape and energy of their frontier orbitals. Our calculations

indicate that increasing the number of carbon atoms in the one-end-closed (5, 5) nanotube, the shape of its frontier LUMO and HOMO molecular orbitals changes periodically, as illustrated in Figure 3.11. The HOMO and LUMO orbitals of nanotubes with 60 atoms, 90 atoms, and 120 carbon atoms have identical shapes, and those of the nanotube with 80 C atoms are identical with the one of 110 C atoms, but because of the period shift, the orbitals of the (5, 5) cap-ended nanotube with 70 atoms are not identical to those of the 100 atoms tube.[74]

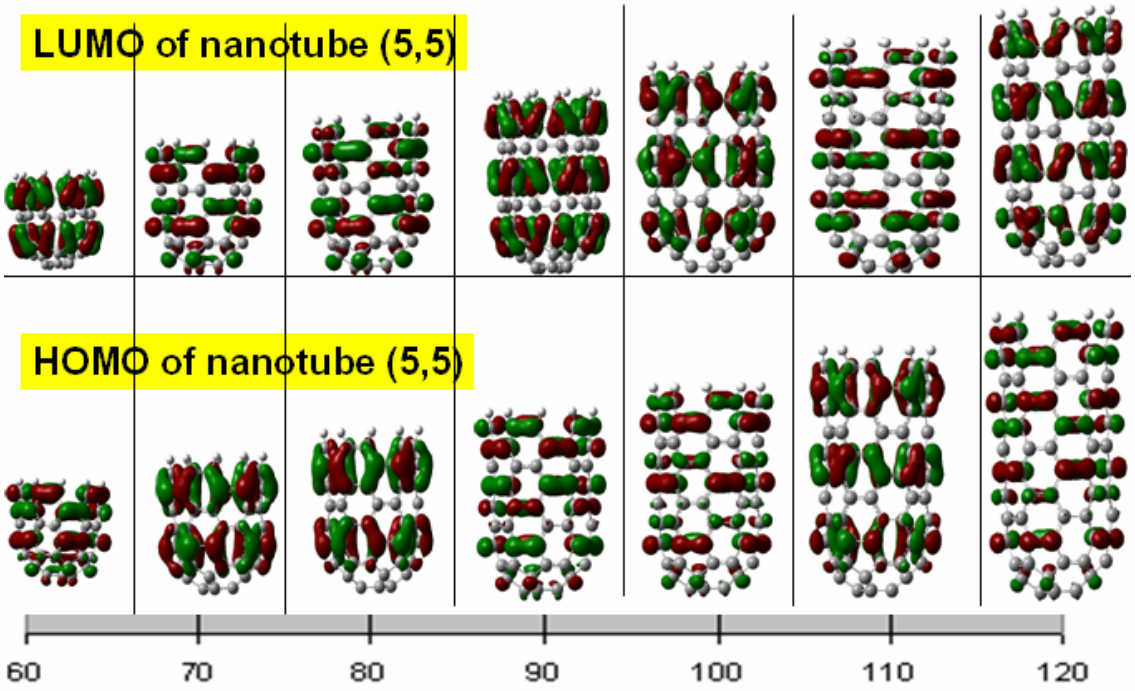

Figure 3.11. HOMO and LUMO of one-end-closed (5, 5) nanotube of increasing number of carbon atoms.[74]

Figure 3.12 illustrates the periodic variation of the energy of the frontier orbitals for the (5, 5) carbon nanotube. Such oscillations in the orbital energies are in qualitative

agreement with those reported by Matsuo et al[21], who calculated the HOMO and LUMO levels in two ends open (5, 5) nanotubes. We have categorized the energetic behavior of the (5, 5) arm-chair cap-ended SWNT into four classes: I, II, II, and IV, which are defined by the symmetry properties of the LUMO and HOMO orbitals, as explained in the following paragraphs. The reaction energy as a function of the number of carbon atoms has also a defined behavior in each region.

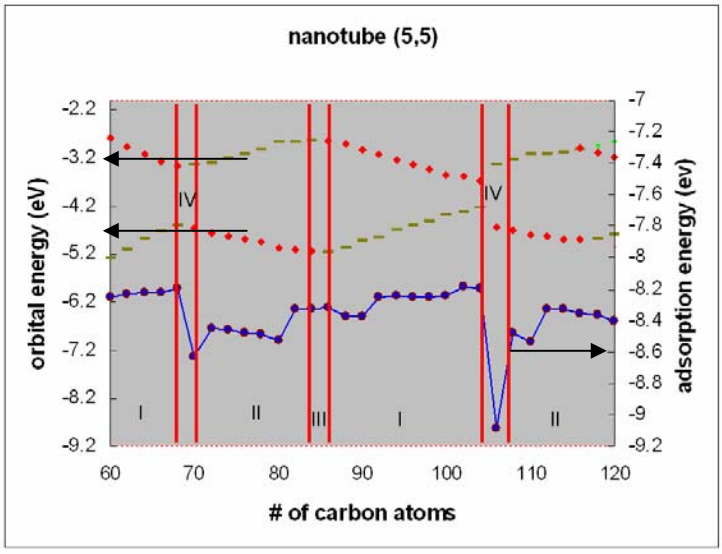

Figure 3.12. Energetic behavior of nanotubes vs. the number of C atoms for one-end-closed nanotube (5, 5).[74] (The upper line corresponds to the LUMO energy and the middle line to the HOMO energy of a (5, 5) nanotube, both measured in the left vertical axis. Red diamonds indicate antisymmetric and green short lines symmetric orbitals. The adsorption energy is given by the solid blue line, measured on the right vertical axis. The vertical lines separate regions of a given type of behavior, as explained in Table 3.2.)

In regions I, the LUMO energy decreases and the HOMO increases, and the opposite behavior takes place in regions II. In region IV, the HOMO energy reaches a maximum, and the LUMO a minimum.

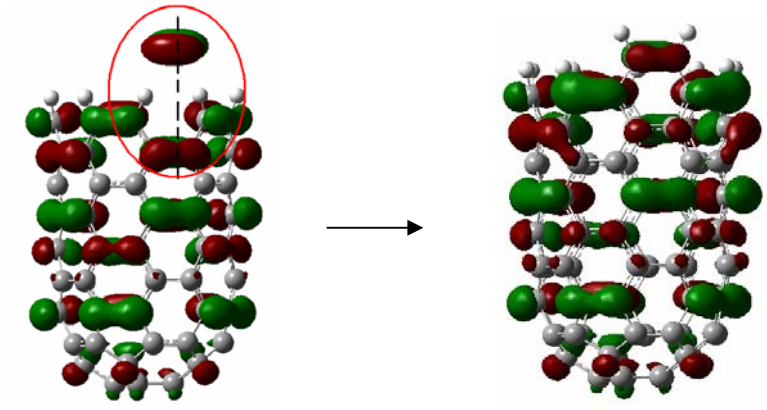

(a) symmetric π orbital of nanotube overlap with π_u of C_2

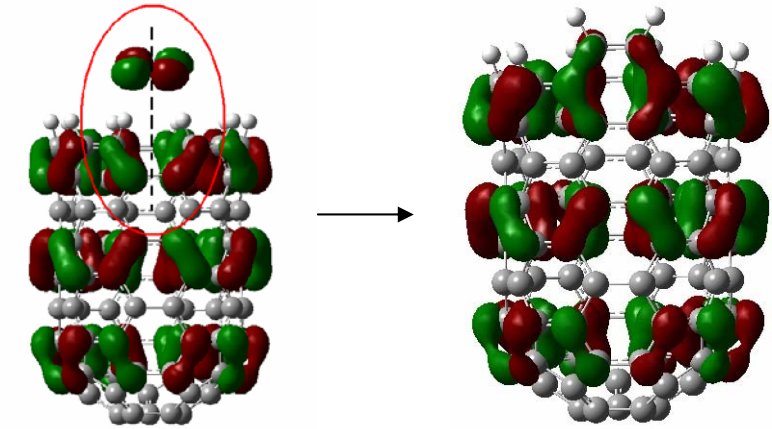

(b) antisymmetric π orbital of nanotube overlap with π_g of C_2

Figure 3.13. Overlap between π orbitals of the nanotube and C_2.[74]

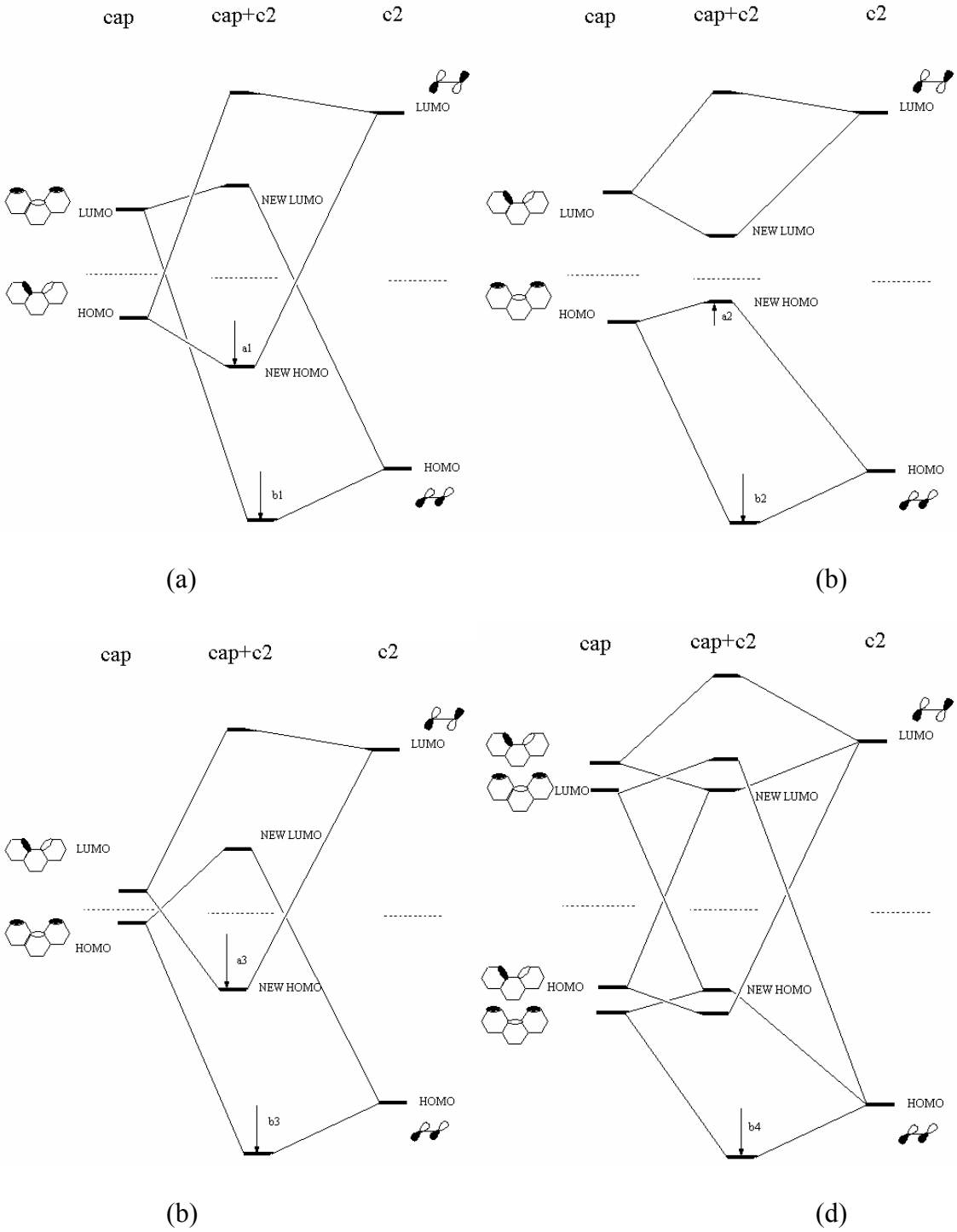

Figure 3.14. Overlap of π orbitals in one-end-closed nanotube (5, 5).[74] Diagrams correspond to symmetry regions indicated in Table 3.2 and Figure 3.12. ((a): Region II; (b): Region I; (c): Region IV;(d): Region III.)

To investigate the details of the reaction, we analyze the orbitals of the reactants and products. C_2 has σ_u, σ_g, π_u, π_g orbitals, which can overlap with the corresponding cap orbitals. Since the cap σ orbitals are all quite low in energy and totally occupied, there is a decrease in the orbital energy because of the σ orbitals overlap which is similar for (5, 5) nanotubes with different number of carbon atoms. On the other hand, the cap π orbital that is symmetric with respect to an axis perpendicular to the C-C bond in C_2, so they can overlap with the π_u of C2, while those that are antisymmetric with respect of the same axis can overlap with the π_g orbital of C_2 as shown in Figure 3.13. As illustrated in Figure 3.14, the energy of the symmetric and antisymmetric π orbitals and their occupancy state changes with increasing number of carbon atoms in the nanotube.

Table 3.2: Correlation between symmetry properties of the HOMO, LUMO orbitals and the reaction energy of the (5, 5) carbon nanotube with C_2.[74] The quantities a1, b1, a2, b2, 13, b3, and b4, are shown in Figure 3.14

Region in Figure 3.12	Symmetry (S: symmetric; A: antisymmetric)				Energy decrease because of overlap of π orbitals	Calculated reaction energy/ eV
	LUMO	HOMO	New LUMO	New HOMO		
II	S	A	S	A	a1 + b1	-8.6~ -8.4
I	A	S	A	S	b2 - a2	-8.3~ -8.2
IV	A	S	S	A	a3 + b3	-9.0~ -8.6
III	S	A	A	S	b4	~ -8.3

Figure 3.14 illustrates the energy decrease due to overlap of the π orbitals as described in Table 3.2.

The periodic behavior shown by the orbital energies explains the corresponding variations of the reaction energy with the increasing number of carbon atoms in the cap-ended (5, 5) nanotube; such oscillatory behavior would make sometimes easier (or more difficult) to add more rings to the cap.

The HOMO and LUMO energies of the larger diameter (6, 6) arm-chair carbon nanotube (Figure 3.15) also display periodic behavior, although with a larger oscillation period.

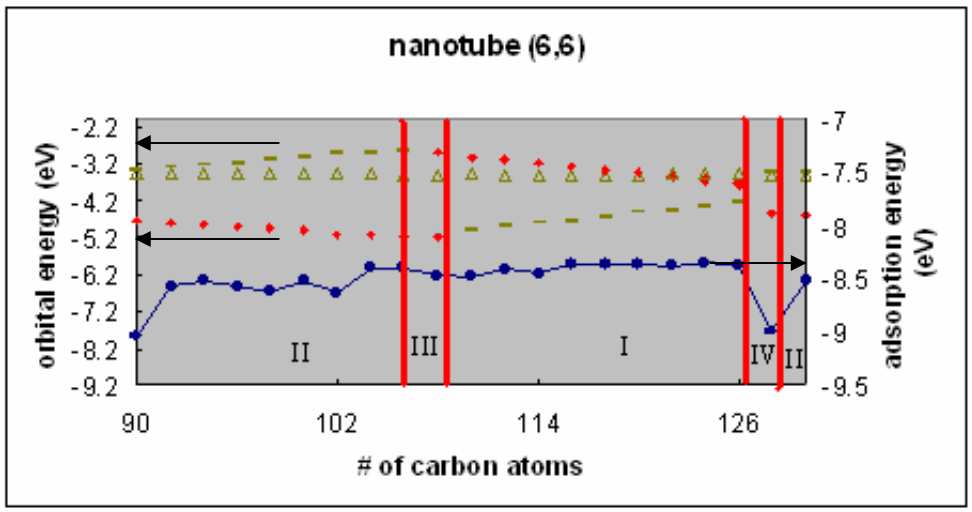

Figure 3.15. Energetic behavior of nanotubes vs. the number of C atoms for one-end-closed nanotube (6, 6).[74] (the top line is the second lowest unoccupied molecular orbital (diamonds and short lines), followed by the LUMO (triangles), HOMO (third line: diamonds and short lines), and adsorption energy (solid blue line))

3.2.3 NICS (+1) of one-end-closed nanotubes with different chirality

Since the nanotube is made up of carbon rings, the aromaticity of these rings is an important property of the nanotube. Aromaticity is a manifestation of electron delocalization in closed circuits, either in two or in three dimensions.[15] This results in energy lowering, often quite substantial and a variety of unusual chemical and physical properties. These include a tendency toward bond length equalization, unusual reactivity, and characteristic spectroscopic features. Since aromaticity is related to induced ring currents, magnetic properties are particularly important for its detection and evaluation.[14] The use of absolute magnetic shielding computed at ring centers (defined as a nonweighted mean of the heavy atom coordinates) with quantum mechanical programs is now a new widely accepted aromaticity/antiaromaticity criterion: negative Nucleus Independent Chemical Shift (NICS) denote aromaticity, positive NICSs indicate antiaromaticity. Considering the specific curved shape of rings in nanotube, we will use NICS(+1) as defined in section 3.1 to study aromatic properties of rings in one-end-closed nanotubes.

We studied one end-closed nanotube (6, 5) with number of carbon atoms from to 81 to 199 with increment of 2. Figure 3.16 shows NICS value of each of the rings in different position of the tubes with each color corresponds to a different nanotube length. To clearly reveal the trend, only a few of the nanotubes are shown though it is observed that all the tubes studied follow the same trend. In Figures 3.16(a) and (b), the curves of nanotube with different length overlap very well at the beginning part which means that the NICS values of the few rings near the open and near the cap do not change with the

number of carbon atoms, but are solely decided by their relative position to the open end or the cap respectively. In other words, increasing number of carbon atoms in the tube is like adding them in the middle part of the tube without changing the NICS of rings near the open end and near the closed end. NICS values of rings near the closed end can be successfully explained by the effect of the five-member rings with the pentagon-proximity model[22].

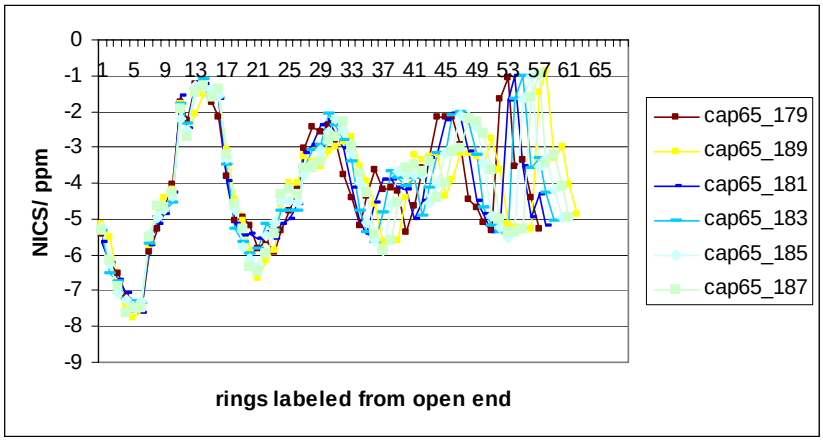

(a)

Figure 3.16. NICS values of rings in one-end-closed chiral (6,5) nanotubes.[75] (a): rings labeled from the open end, (b): rings labeled from the closed end.

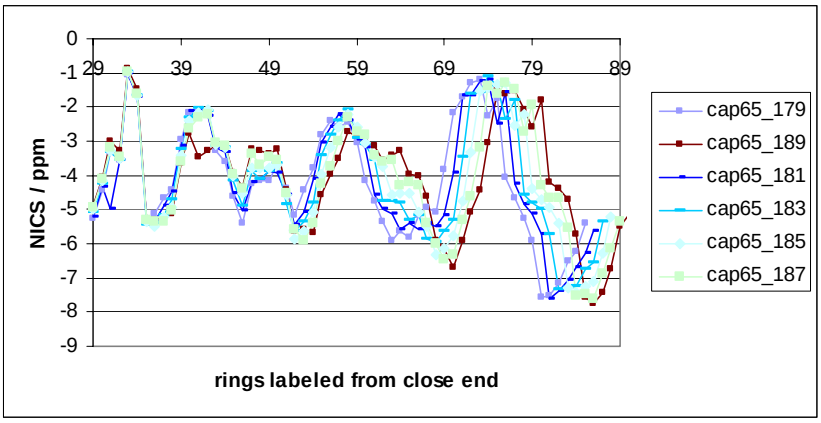

(b)

Figure 3.16. Continued.

We studied one end-closed nanotubes (5, 5) with number of carbon atoms from to 60 to 130 with increments of 10. The NICS values of rings in the one-end-closed (5, 5) nanotube change dramatically depending on the nanotube length. If we ignore the changes of NICS of the rings in the middle part of the tube, the NICS of rings near the open end and near the closed end changes periodically with the increasing of the number of carbon atoms in the ring. Figure 3.17 illustrates the variation of the NICS value for rings belonging to one-end-closed (5, 5) nanotube. The NICS values of first two layers of rings from the open end (Figure 3.17(a), ring 1 to ring 10) show similar performance for nanotube (5, 5) with 60 carbon atoms, 90 carbon atoms and 120 carbon atoms, 80 carbon atoms and 110 atoms, 100 atoms and 130 atoms. The same is that of rings near the cap (ring 17 to ring 27 of Figure 3.17(b)). However nanotube (5, 5) with 70 carbon atoms is quite different from that of 100 carbon atoms and 130 carbon atoms. In Section 3.2.2, we studied the periodic changes of the shape and orbital energies of these

nanotubes and explained the mismatch of nanotube (5, 5) with 70 carbon atoms with corresponding nanotubes as the result of a shift of the switch point. Periodic changes of structure and property has also been observed for open-ended (5, 5) (6, 6) and (7, 7) nanotubes of different lengths and successfully explained with the Clar Valence Bond Model[21].

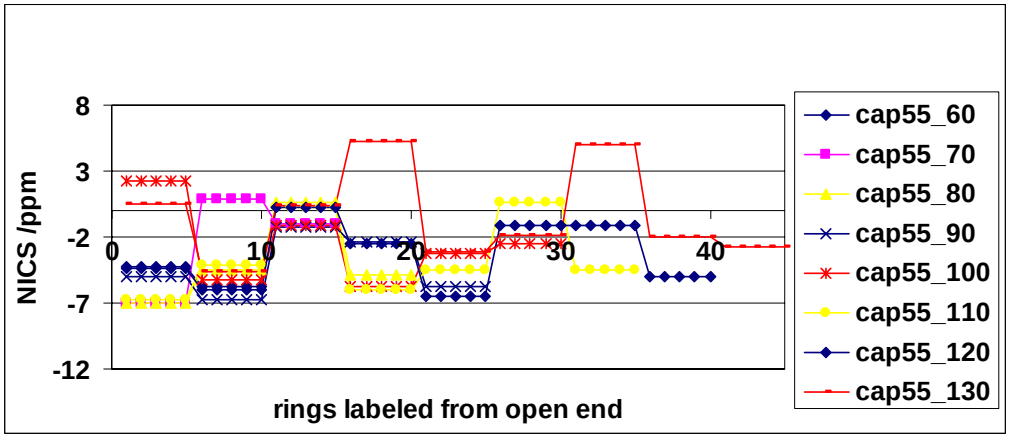

(a)

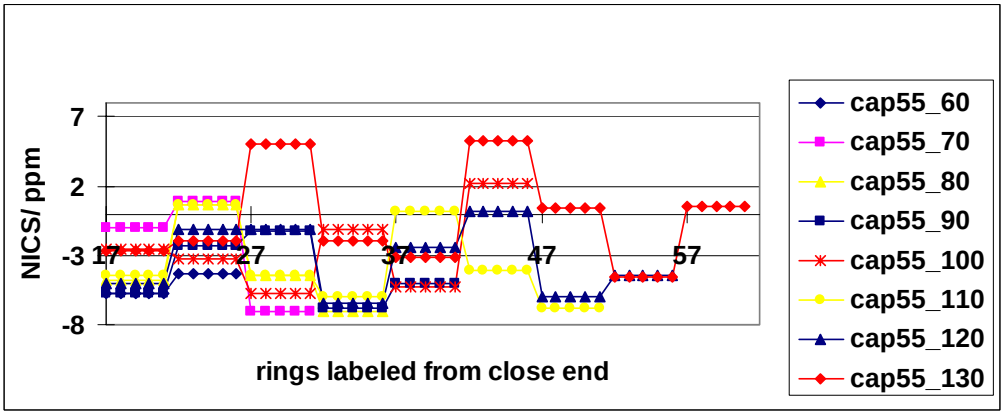

(b)

Figure 3.17. NICS values of rings for one-end-closed (5, 5) nanotubes of various lengths indicated by the number of carbon atoms shown in the legend.[75]

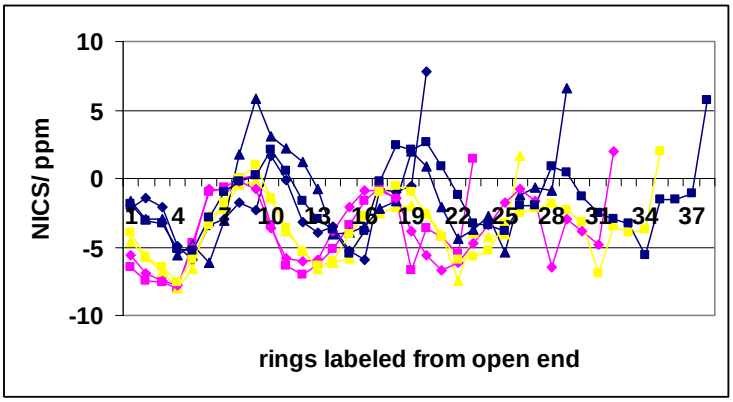

(a)

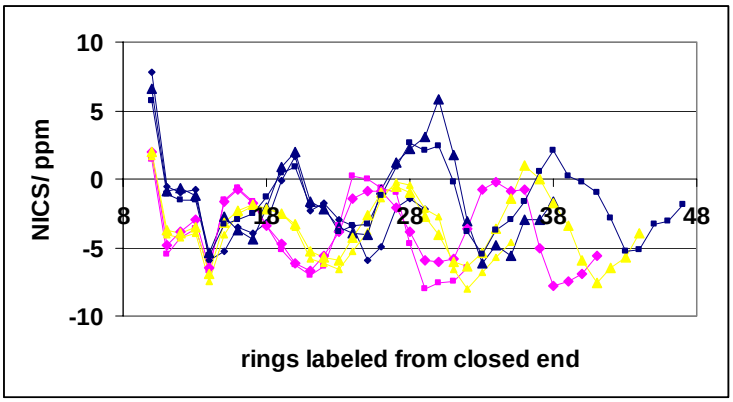

(b)

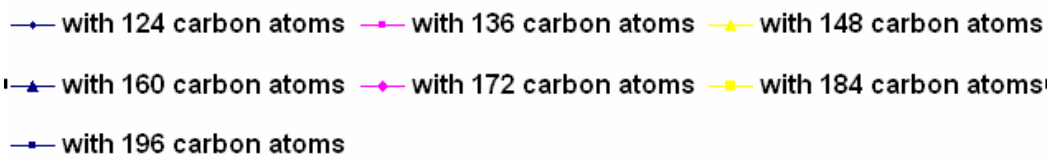

Figure 3.18. NICS values of rings in one-end-closed chiral (7, 5) nanotubes.[75]

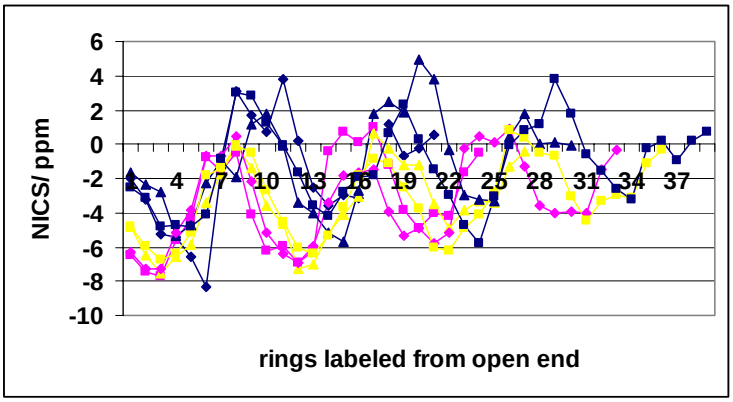

(c)

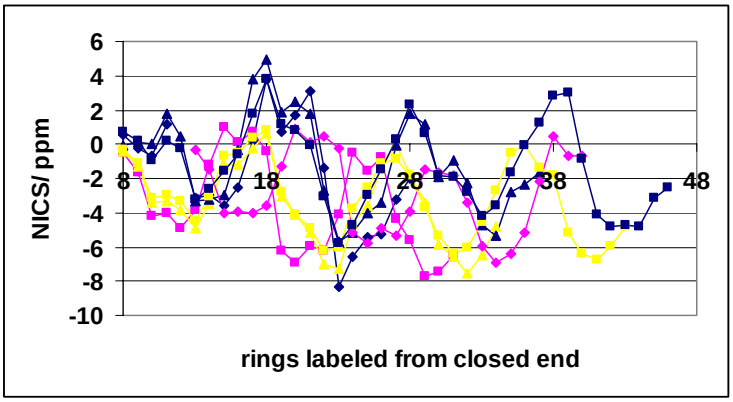

(d)

Figure 3.18. Continued.

We studied nanotubes (7, 5) with number of carbon atoms from to 122 to 196 with increments of 2 and observed NICS of rings changes with the number of carbon atoms in the nanotube with a period of 36, namely, nanotube (7, 5) with 124 carbon atoms shows similar behavior with that with 160 carbon atoms and that with 196 carbon atoms. So it is nanotube with 136 carbon atoms and with 172 carbon atoms, nanotube with 148 carbon atoms and with 184 carbon atoms. As can been seem in Figures 3.18(a) and (b),

the first few rings in the open end have the same value for corresponding nanotube. So it is the rings near the close end in Figures 3.18(c) and 3.18(d).

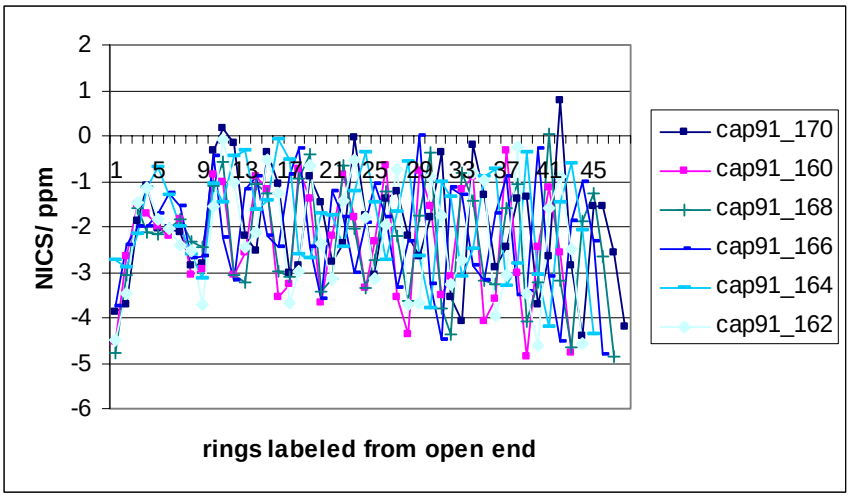

(a)

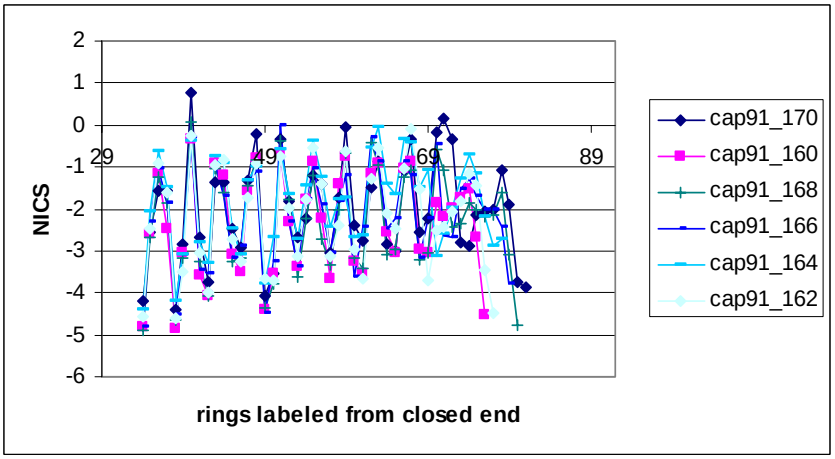

(b)

Figure 3.19. NICS values of rings in one-end-closed (9,1) nanotube with carbon atoms less than 190.[75]

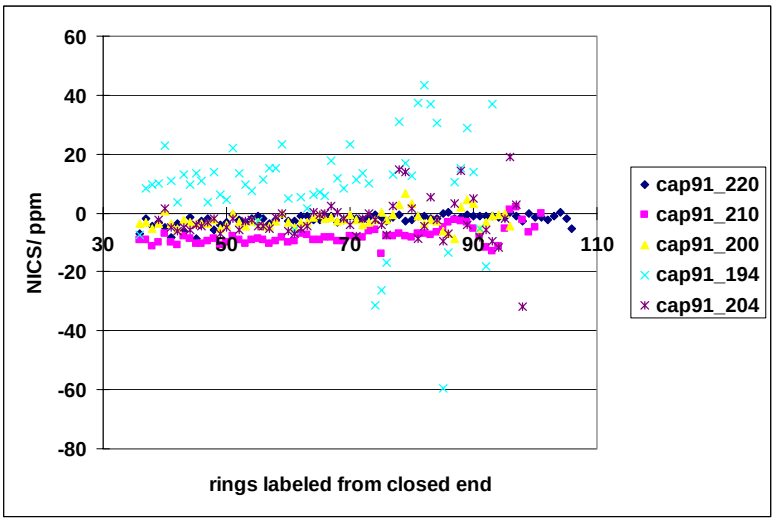

Figure 3.20. NICS values of rings in one-end-closed (9,1) nanotube with carbon atoms from 194 to 220.[75]

NICS values of nanotubes (9, 1) with number of carbon atoms from 82 to 190 with increments of 2 are studied. When the number of carbon atoms is less than 190, NICS values of most of the rings in the tube are determined by their relative position with respect to the five-member rings in the cap except that the first 9 rings at the open end are decided by their relative position with respect to the open end. In Figure 3.19(b), the curves overlap very well except for the last few points of each curve, while in Figure 3.19(a) it is very hard to see any overlap except for the first 9 points which represent the first layer of rings at the open end. When the number of carbon atoms is bigger than 190, some of rings shows abnormally big (~ 40) or small value (~ -30), as shown in Figure 3.20. No obvious trend is found is this part.

Summarizing, Figure 3.21 illustrates the variation of the NICS value of the first ring at the open end of the nanotube as a function of the nanotube length for (6, 5) (5, 5) (7, 5) and (9, 1) nanotubes. The NICS value of first ring in (6, 5) nanotube does not change

much while increasing the nanotube length. The NICS values of the ring at the beginning of the open end of the (7, 5) and (5, 5) nanotubes change periodically with period of 30 carbon atoms and 36 carbon atoms respectfully, while that of nanotube (9, 1) also changes with the number of carbon atoms in the tube and no obvious periodic change is observed.

The NICS values of the first ring at the open end of nanotube with different lengths are compared with that of the formation energies of that ring which are calculated with equation 3.1. For nanotube (5, 5), nanotube (7, 5) and nanotube (6, 5), the bigger the NICS value, the higher the formation energy since the NICS value is an index of the stability of the ring. But such correlation is not quite obvious in the nanotube (9, 1).

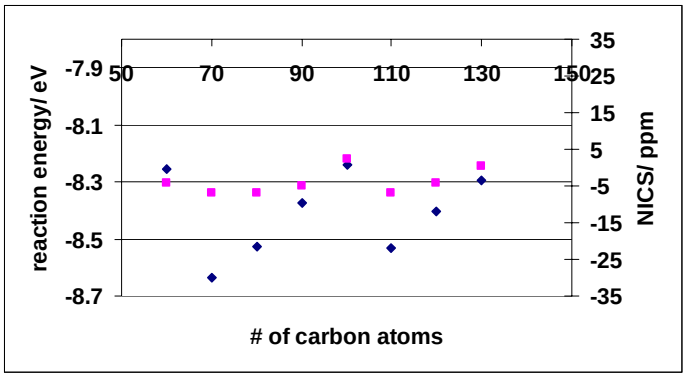

(a) nanotube (5, 5)

Figure 3.21. NICS of the first ring at the open end v.s. reaction energy (purple lines and yellow lines: NICS value of the first ring at the open end, blue lines: reaction energy of forming that ring).[75]

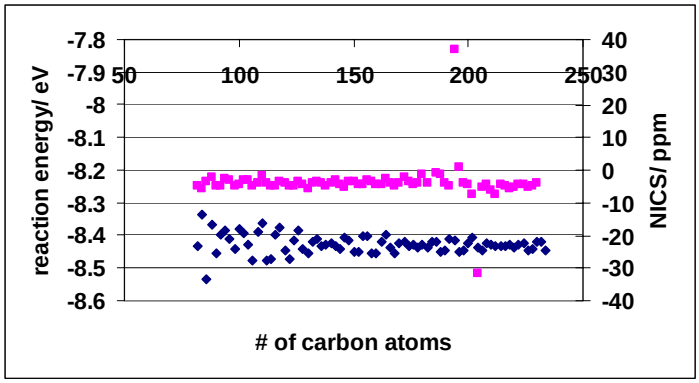

(b) nanotube (9, 1)

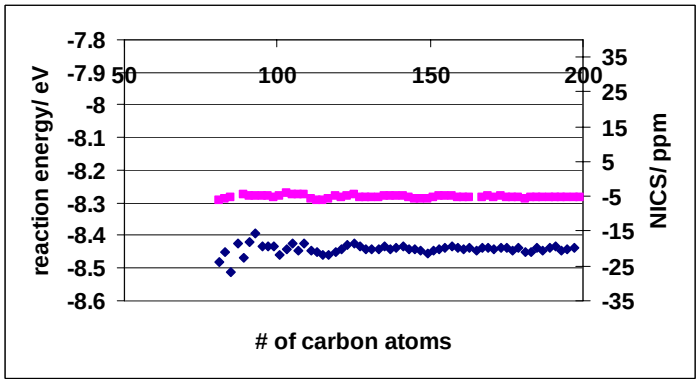

(c) nanotube (6, 5)

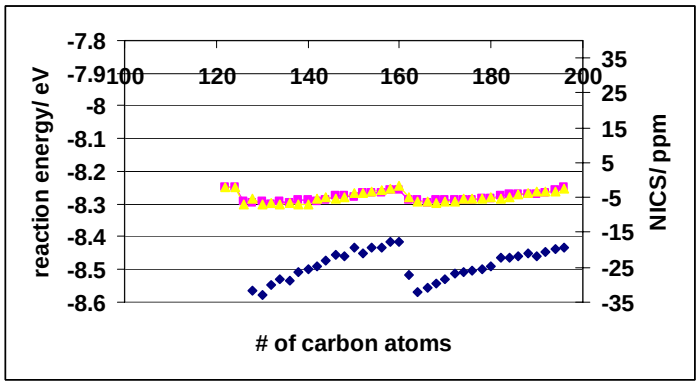

(d) nanotube (7, 5)

Figure 3.21. Continued.

3.3 Nanotubes with and without cap

Considering the broad spectra of working synthesis conditions, it is likely that growth of SWCNTs by different techniques might follow different mechanisms. The cap-ended nanotube growth mechanism is widely used to describe the growth by CVD methods carried out in the temperature range that metal atoms can form clusters.[48,50,51] In contrast, for synthesis techniques working at much higher temperatures metal atoms may exist as isolated atoms, and a two-stage growth model has been proposed to describe growth of single wall carbon nanotubes where in the nucleation step ring carbon clusters, instead of caps, are formed and the nanotubes produced are open-ended[78,79].

Numerous reports have analyzed these two mechanisms but we are not aware of any comparison. Here we study the effect of cap structure on the aromatic properties of SWCNTs as given by the evaluation of their NICS values. Basically we compare nanotubes with both ends open and those with the same chirality but with one-end-closed by a cap structure and the other end open. This will allow us to provide new insights for comparing cap-ended growth mechanisms with those of open ended mechanisms from a new prospect.

3.3.1 NICS(axis)

NICS scan carried out in section 3.1.3 shown that there is an obvious chemical shift at the axis of the nanotube, which reveals the shielding effect of π orbitals all over the tube. Figure 3.22 shows how NICS values measured on different positions of the nanotube axis change with different lengths, chirality and open end/closed end tube

structure. The x coordinate corresponds to the tube axis and the zero point is located at one of the tube ends. For one-end-closed nanotubes, x equals zero corresponds to the open end of the tube while the other end of the curve correspond to the axis where the half fullerene connects with the cylinder. So we expect that the NICS values at this end would reveal the effect of the cap (Figures 3.22(a) and(c)). For two-ends-open nanotubes, there is symmetry with respect to the two ends of the curve, as shown in Figures 3.22(b) and (d).

Figures 3.22 (a) and (c) illustrate that for one-end closed nanotubes, the NICS value on the axis decreases from the open end to tube interior, suggesting that the shielding effect is stronger inside the tube than at the open end. But for nanotube (6, 5), in most cases (except for the shortest nanotube) there is a minimum value close to the center of the tube, and then the NICS values increase reaching a value at the closed end which is lower (in about 5 ppm) than that at the open end. Such NICS value at the closed end is the same for all the tubes except for the shortest one. On the other hand, NICS values for the one-end-closed (9, 1) nanotube decrease from the open to closed end along the tube axis (Figure 3.22(c)).

Significant differences are also observed in the NICS (axis) behavior of the two-ends-open (6, 5) and (9, 1) nanotubes. The minimum NICS values observed at the tube center in the (6, 5) nanotube decrease as the tube length increases (Figure 3.22(b)), whereas in the (9, 1) the NICS (axis) values does not follow a monotonic trend with the tube length, and for the lengths shown in Figure 3.22(d) the minimum values follow the opposite trend to the (6, 5), increasing as the tube length increases.

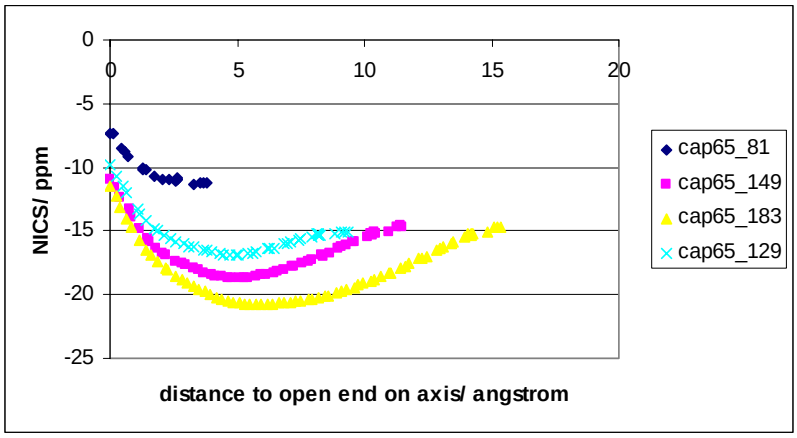

(a) one-end-closed nanotube (6, 5)

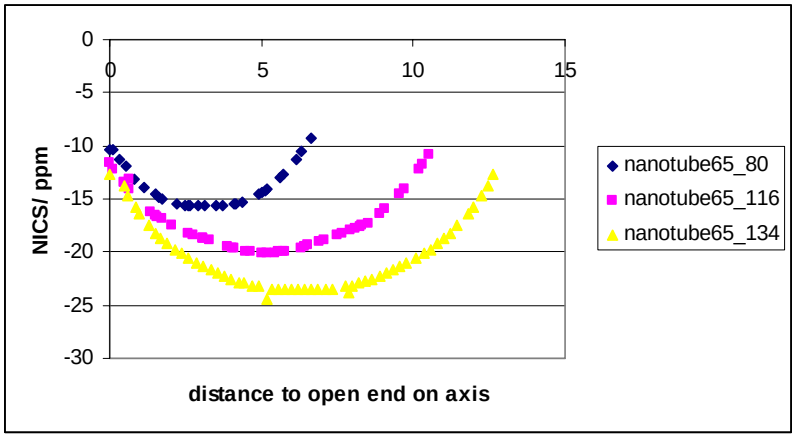

(b) two ends open nanotube (6, 5)

Figure 3.22. NICS values evaluated at the nanotube axis.[76]

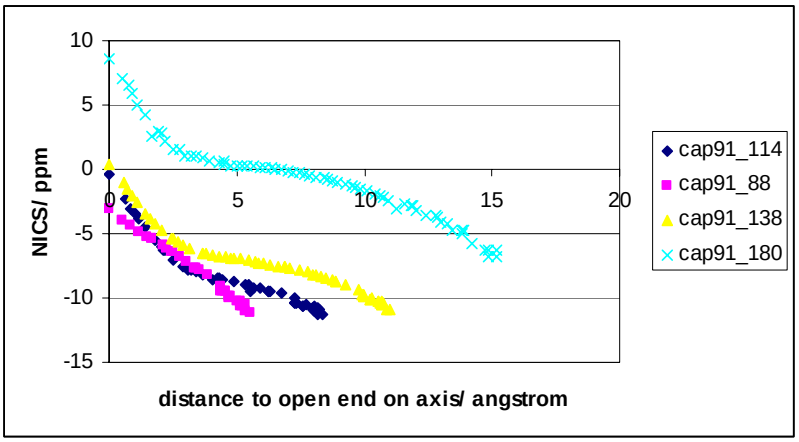

(c) one-end-closed nanotube (9, 1)

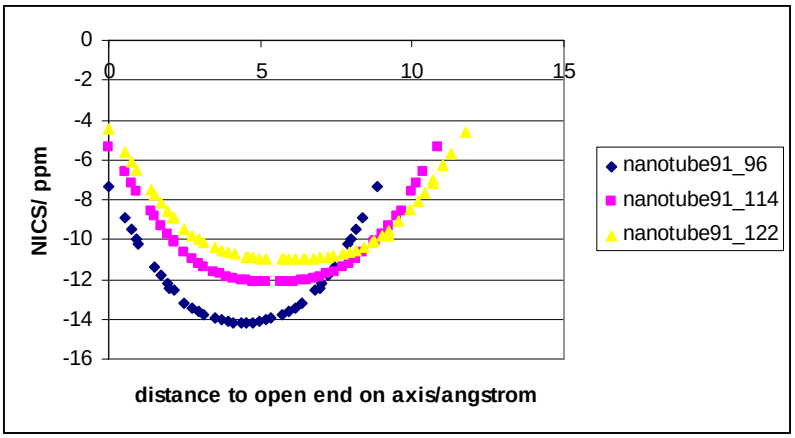

(d) two ends open nanotube (9, 1)

Figure 3.22. Continued.

3.3.2 NICS (+1)

NICS (+1) of the first ring at the open end of one-end-closed nanotubes (6, 5) and (9, 1) have been discussed in section 3.2.3. In this section, these results are compared with those with two ends open nanotubes (6, 5) and (9, 1) as shown in Figure 2.23. Since most curves in Figure 3.22 are nearly parallel to each other, values of NICS (axis) at x

equal zero of each curve may be used to represent the tube's total shielding effect; these values are also shown as a function of tube length(yellow lines) in Figure 3.23. For two-ends-open (6, 5) nanotube (Figure 3.23(a)), the NICS (axis) of the open end (yellow curve) is lower than that of the NICS (+1) by about 5 ppm, for all tube lengths. However, for nanotube (6, 5) with one-end-closed (Figure 3.23(b)), the difference between NICS(+1) and NICS(axis) increases increasing the tube length, until it reaches nearly the same value of 5 ppm as in the two-ends-open nanotube (6, 5). This is because the cap structure has an effect on the tube shielding that decreases as the distance from the cap increases. When the tube is long enough, the effect at the open end disappears. For the two-ends-open (9, 1) nanotube, the NICS (axis) value at the open end is lower than that of the NICS (+1) and the difference decreases as the tube length increases. The values of the NICS (axis) for the two-ends-open (9,1) nanotube range between -7 and -4 ppm are much higher than those of the corresponding nanotube (6 ,5) (-10~-14 ppm). As for the one-end-closed nanotube (9, 1), the NICS (axis) value is higher than the NICS (+1) and even if the two abnormal points that do not agree with the energy criteria were not considered, there are still several nanotubes with positive NICS values which means that in that case, there is deshielding instead of shielding effect.

Both one-end-closed and two-ends-open nanotube (9, 1) have abnormally big or small NICS values at certain lenghts as shown by purple lines in Figures 3.23(c) and (d) and they do no correspond to big or small reaction energy.

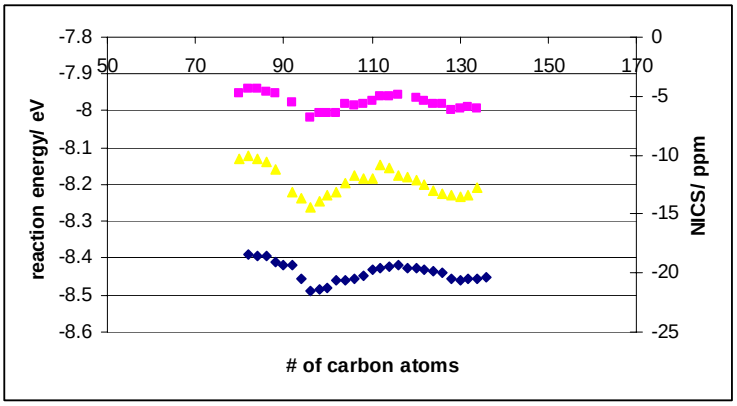

(a) nanotube (6, 5) with two ends open

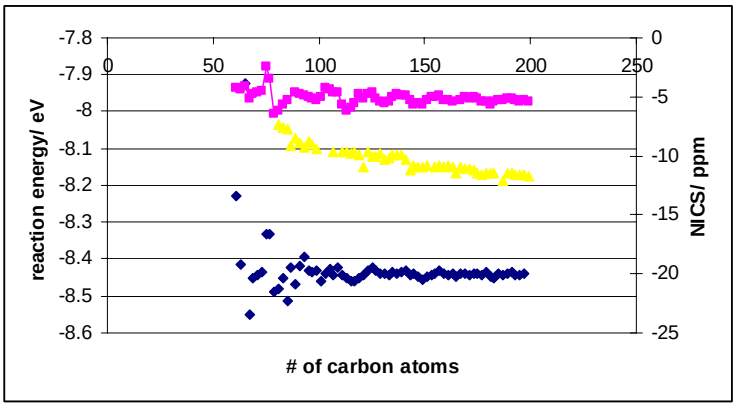

(b) one-end-closed nanotube (6, 5)

Figure 3.23. NICS values and reaction energy (purple lines: NICS value of the first ring at the open end, blue lines: reaction energy of forming that ring, yellow line: NICS at axis of the open end).[76]

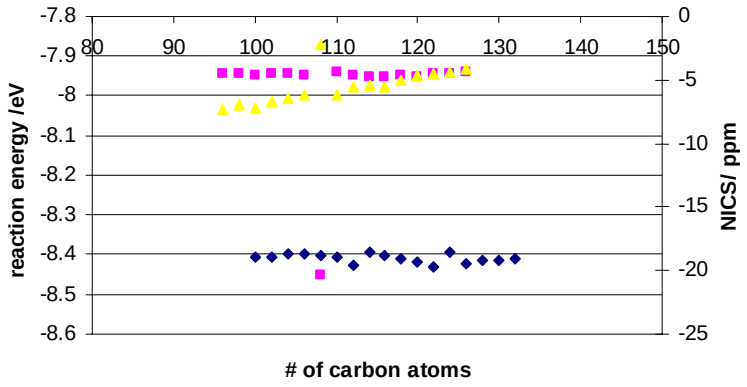

(c) nanotube (9, 1) with two ends open

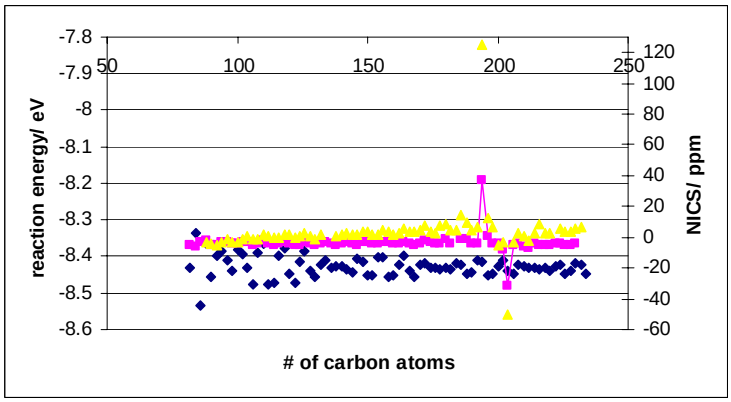

(d) one-end-closed nanotube (9, 1)

Figure 3.23. Continued.

3.4 (8, 3) nanotubes with one-end-closed by different cap structures

For a nanotube with a given chirality, there may be several possible cap structures that could fit it, and the number of possible compatible cap structures increases with the nanotube diameter[9,10]. High selectivity regarding chirality in the CoMoCAT method only

happens in nanotubes with small diameter where most nanotubes have just one or few possible cap structures. It is interesting to find out whether these cap structures play an important role in the selectivity mechanism. Here we compare properties of (8, 3) nanotubes that are bonded to all the three kinds of caps compatible with the (8, 3) structure. The (8, 3) nanotube has a diameter of 7.82Å, which is intermediate between those of the (6, 5) and (7, 5) that have been found as abundant products in the CoMoCAT process.

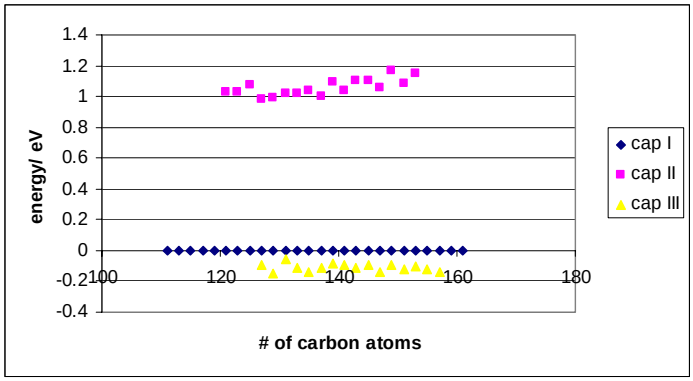

Figure 3.24. Energies of (8, 3) nanotubes bonded to three kinds of caps relative to those of nanotube bonded to cap I (structures of these caps are shown in Figures 3.3 (e)-(g)).[76]

Figure 3.24 illustrates the energetic differences between the (8, 3) nanotubes with different caps. Energies are calculated relative to that of the nanotube bonded to cap I with the same number of carbon atoms. Energies of nanotubes bonded to cap I are a little bit higher than those bonded to cap III and much lower than those bonded to cap II. This can be explained by the uneven distribution of pentagons in cap II (as shown in Figure

3.3(f)), since according to isolated pentagon rule the more even the pentagons distributed, the lower the energy.[8]

It is reported that the NICS values of rings in fullerene are determined by their relative positions to those pentagons.[22] Here we study aromatic properties of rings at the open end to see if it is also related to the pentagons' distribution because we believe the structure at the open end is more important for understanding of growth of single wall carbon nanotubes.[75] As shown in Figure 3.25, (8, 3) nanotubes closed with these three different kinds of cap shows similar reaction energies and NICS values. For each kind of nanotube, both the reaction energy and NICS shows a little variation with increasing number of carbon atoms in the nanotube while lower reaction energy corresponds to lower NICS value which both indicate the presence of aromatic rings.

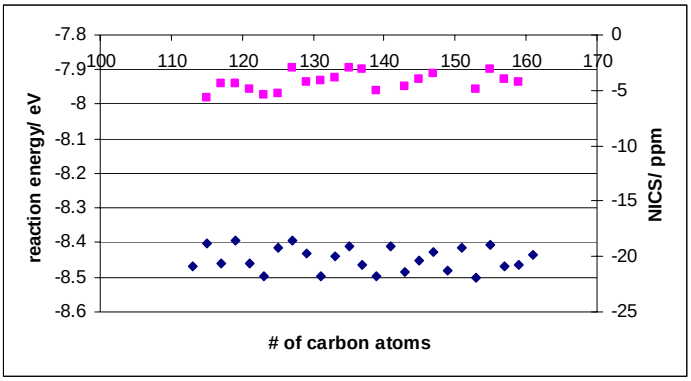

(a) cap I

Figure 3.25. NICS of the new formed ring at the open end and formation energy of that ring in nanotube (8, 3) bonded to three different kinds of cap (purple lines: NICS value of the first ring at the open end, blue lines: reaction energy of forming that ring).[76]

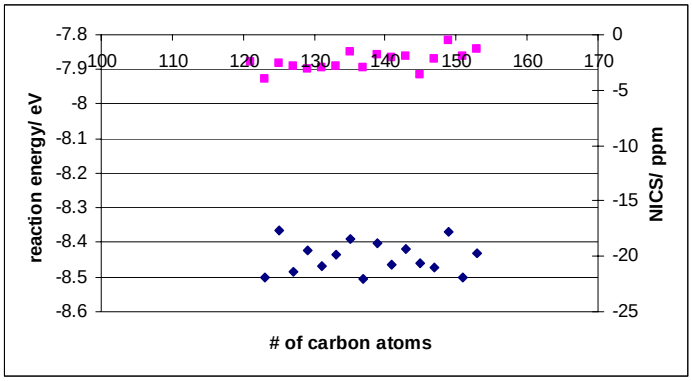

(b) cap II

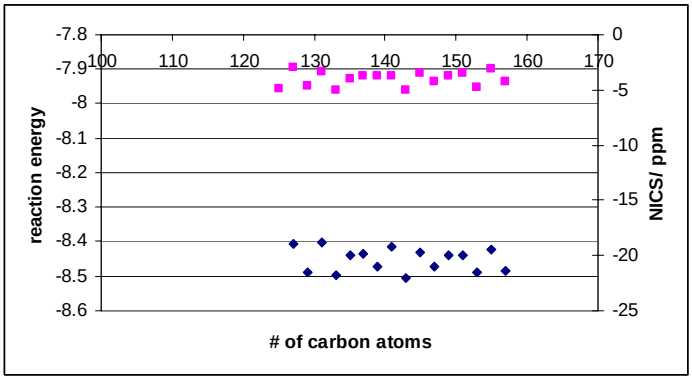

(c) cap III

Figure 3.25. Continued

3.5 Conclusions

An oscillatory behavior as a function of the number of carbon atoms is observed in the orbital energies of the arm-chair cap-ended SWNTs, which is reflected in oscillations in the reaction energy. In contrast reaction energy of chiral nanotube (9, 1) and (6, 5) is stable when the number of carbon atoms in the tube reaches a certain value, and that of nanotube (7, 5) also change periodically with increasing number of carbon atoms but

with much smaller vibration amplitude. The smallest value of the reaction energy of nanotube (5, 5) is slightly lower than other nanotubes with nearly the same diameter.

The NICS values of rings in one-end-closed nanotubes (5, 5) and (7, 5) vary periodically with the nanotube length, while those of nanotubes (6, 5) do not vary with the tube length. The NICS values of rings in nanotube (9, 1) do not change much with the tube length when the number of carbon atoms is less than 190. Above that value, there are rings with abnormally big or small NICS values. For most of the nanotubes studied, the lower the NICS value of the first ring at the open end, the lower the reaction energy of forming that ring, both indicating an aromatic ring except that the two abnormally low and high NICS values of nanotube (9, 1) do not correspond to substantial low or high formation energy. The NICS behavior of nanotube (6, 5) is quite different from that of nanotube (5, 5), (7, 5), or (9, 1) in that the first ring at the open end remains constant suggesting a stable aromatic property despite of the change of length of the tube. However, it is still too premature to draw any correlation between these observations and the reasons that nanotube (6, 5) is abundant in synthesis processes while nanotubes (9, 1), and (5, 5) are not found in large amounts or not found at all. More calculations are needed to reveal the physical and chemical properties intrinsic to nanotubes with different chiralities. Also, more studies on the growth mechanism are needed.

NICS of the first ring in two-ends-open nanotube (6, 5) varies slightly with increasing of nanotube length while that of one-end-closed nanotube (6, 5) shows no variation. Shielding effect at the nanotube axis near the open end is stronger than at the

first ring in nanotube (6, 5), the difference between NICS (axis) and NICS (+1) being nearly constant for the two-ends-open nanotube (6 ,5) whereas that for one-end-closed nanotube (6, 5) increases with tube length until reaching nearly the same value as that of the two-ends-open nanotube (6 ,5).

Both one-end-closed and two-ends-open (9, 1) nanotubes show some abnormally big or small NICS values. In the two-ends-open nanotube (9, 1) the shielding effect at the axis near the open end is stronger than that of the first ring, and the difference between NICS (axis) and NICS (+1) decreases while increasing tube length. In the one-end-closed nanotube (9, 1) the shielding at the axis is weaker than at the first ring, in some cases, there is deshielding effect instead of shielding effect at the axis near the open end.

Although nanotubes with and without cap show significant differences in the aromaticity properties, the detailed structure of cap does not have a noteworthy effect on NICS behavior, at least for nanotube (8, 3). Although nanotubes bonded to one kind of cap have higher energy than those bonded to the other two kinds of cap, in (8, 3) nanotubes that bonded to these three different kinds of cap, the energy of forming one more ring at the open end and the corresponding NICS value showed similar behavior.

Thus, this study confirms that the presence of the cap and the specific chirality provide distinct aromaticity and reactivity properties to SWCNTs, whereas the particular nature of the cap seems to be of no relevance for these properties.

4. INTERACTIONS BETWEEN COBALT CLUSTERS AND MoC SUBSTRATE

From analyses of the CoMoCAT experimental process, it is pretty clear that SWCNTs are grown from Co clusters attached on Mo carbide surfaces and that the selective growth of SWCNTs may be highly related to the substrate.[6] Also as shown in section 2, the shape of the cluster and the initial steps of the growth of the nanotube highly depend on the interaction between the Co cluster and substrate. So in this section, a series of Co clusters loaded on a MoC surface are studied.

4.1 Methodology

4.1.1 MoC crystal structures

From the bulk phase diagram of Mo carbide[80], β'-Mo_2C and WC structured MoC are the only two stable phases of Mo carbide in the temperature range of 800~1200K and since under the experimental synthesis conditions, carbon is abundant because of the decomposition reaction of CO, we suggest that the Mo carbide phase formed may be the WC structured MoC.

WC-MoC crystal cell is shown in Figure 4.1. There are two atoms in the cell, one Mo atom at origin and one C atoms at 2/3**a1**+1/3**a1**+1/2**c** where **a1**, **a2** and **c** are the basic lattice vectors defined by the three edges of the crystal cell that start from the origin as shown in Figure 4.1. Lengths of the crystal parameters are a1=a2=2.92 Å, c/a1=0.97.

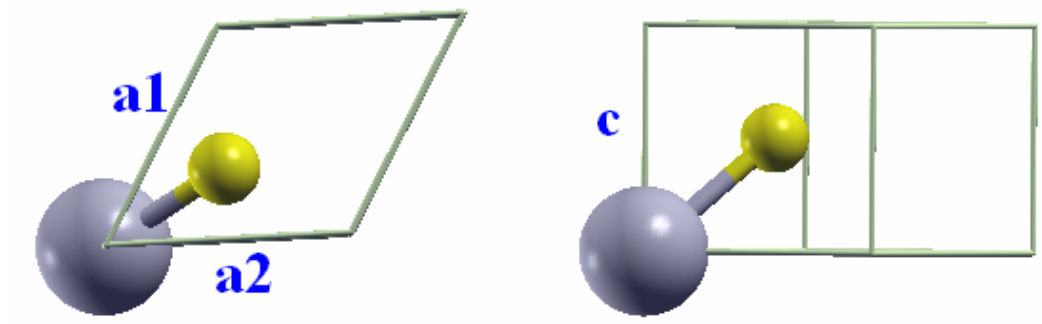

(a) top view (b) side view

Figure 4.1. WC-MoC crystal cell (silver atom: Mo, yellow atom: C).

4.1.2 Computational details

Our calculations were performed with the projector augmented wave (PAW) method[81] in the formalism of density functional theory as implemented in the VASP package[82-86]. The exchange correlation functional with the generalized gradient approximation (GGA) in the PBE form was employed[87]. A plane-wave energy cutoff of 400 eV and meshes of (5 x 5 x 1) k points are used.

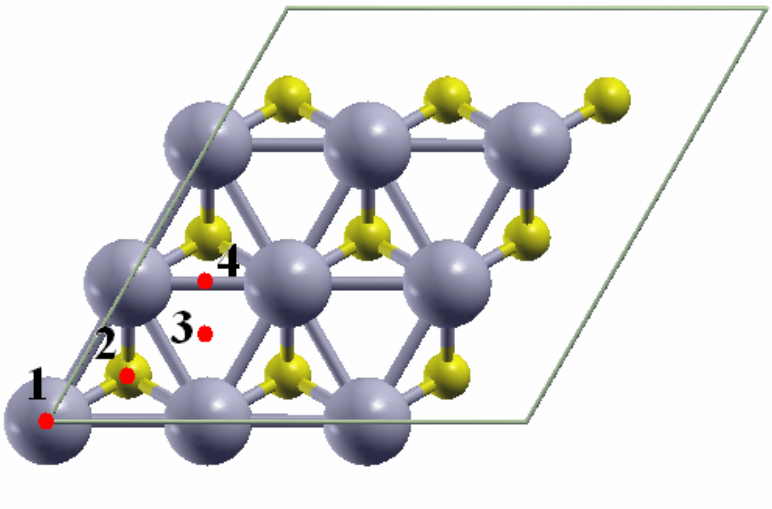

(a) top view

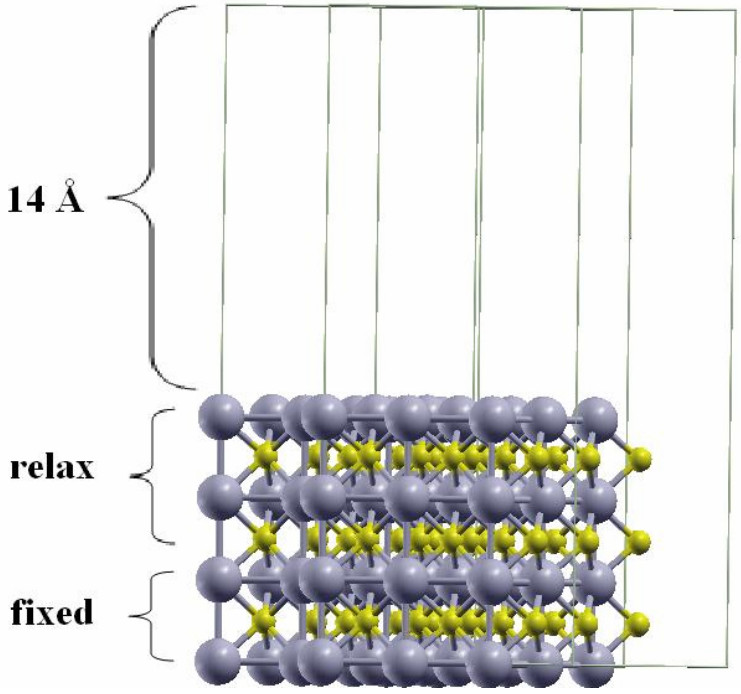

(b) side view

Figure 4.2. Seven layered MoC slab. (1: top position, 2: hcp hollow position, 3: fcc hollow position, 4: bridge position)

Two different simulation cells are used in this work. For adsorption of Co clusters containing less than or equal to 4 Co atoms, the MoC surface is represented by a slab made up of four layers of Mo atoms and three layers of C atoms with the bottom two layers of Mo atoms and one layer of C atoms fixed and the rest of the atoms free to optimize as shown in Figure 4.2.

For adsorption of Co clusters having more than or equal to 7 atoms, in order to avoid the interactions of Co clusters between adjacent cells due to periodic boundary conditions, the x and y directions of the cell should be enlarged. In that case, to save computational time, a totally fixed three layers slab (two layers of Mo atoms and one layer of C atoms) as shown in Figure 4.3 is used to represent the cell. This model is valid since our calculations showed that the relaxed layers in Figure 4.2 actually do not normally deviate a lot from their original positions both before and after adsorption of Co_N clusters when N is less or equal to 4.

In most cases, when a cluster with certain number of Co atoms is adsorbed on the MoC surface, there are several possible shapes and the adsorption sites occupied by these atoms could also be different. The one with lowest energy (E0) is taken as reference while all the systems' energies relative to this one (E-E0) are compared.

Besides, for N=1-3, the geometries of free Co clusters have high symmetry and can be easily optimized. Adsorption energy of these clusters is also calculated, which is defined by:

$$E_{ads} = E(Co_N - MoC\,complex) - E(MoC\,slab) - E(Co_N) \quad (4.1)$$

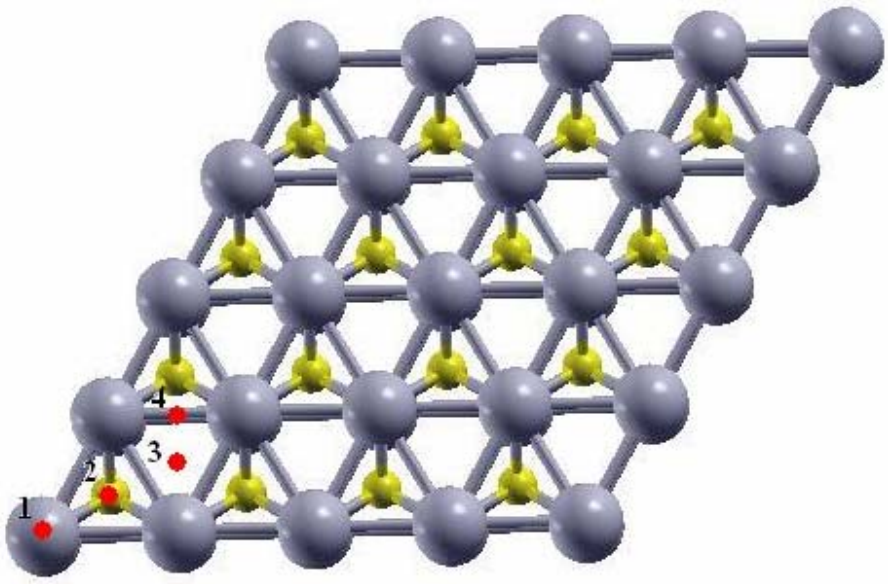

(a) top view

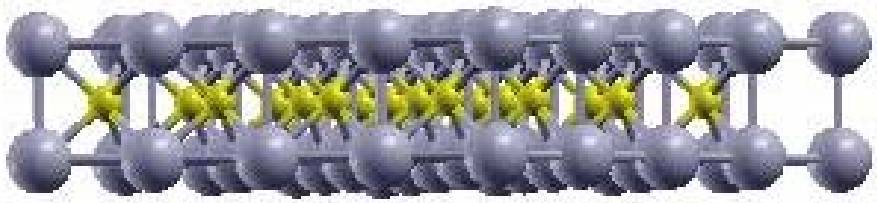

(b) side view

Figure 4.3. Three layered MoC slab (1: top position, 2: hcp hollow position, 3: fcc hollow position, 4: bridge position).

For N=4, 7, 10, 14, 15, the geometries of free Co_N clusters are too complex to be discussed, so adsorption energies are not calculated. To better describe the shape of the

clusters, two diameters D1 and D2 of the attached Co_N clusters are introduced, which are defined the largest and smallest diameter of the first layer as shown in Figure 4.4.

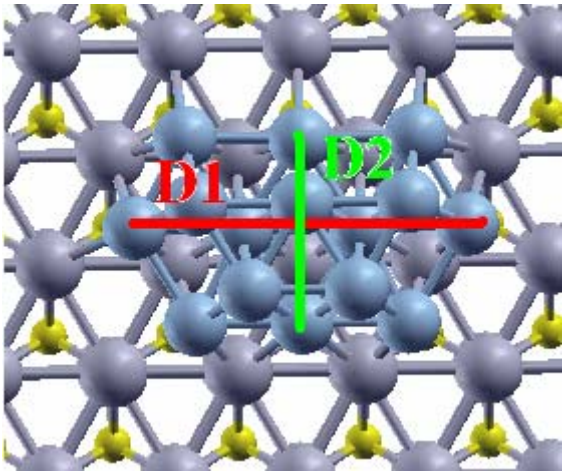

Figure 4.4. Definition of diameters of Co_N cluster (red and green line represent diameters D1 and D2 respectively).

4.2 Adsorption of Co_N cluster on MoC surfaces

Adsorption of one cobalt atom on top, hcp hollow, fcc hollow, and bridge position of the WC-MoC surface as represented by red dots in Figure 4.2 are studied. It is found that the cobalt atom can not be stably adsorbed on top or bridge position. Though the Co-Mo bond lengths are nearly the same (~2.40 Å), the adsorption energy on the hcp hollow site (-4.446 eV) is 0.467 eV lower than that on fcc hollow site (-3.979 eV).

We also studied adsorption of Co diatom on the MoC surface. It is found that despite the initial position of the Co atoms, after optimization, two Co atoms will move to two adjacent hcp hollow sites as shown in Figure 4.5.

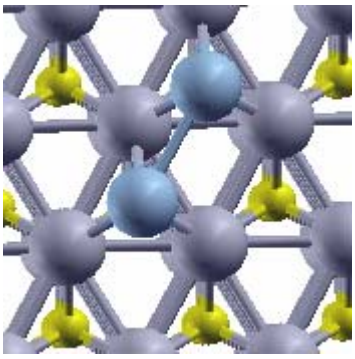

Figure 4.5. Optimized structure of Co_2 on MoC surface.

There are two stable adsorption positions for Co_3: one is that all three Co atoms are adsorbed on adjacent hcp hollow sites (Figure 4.6(a)) and the other is that all three Co atoms locate on adjacent fcc hollow sites (Figure 4.6(b)) while the adsorption energy of the former case is 1.1 eV lower than that of the later case.

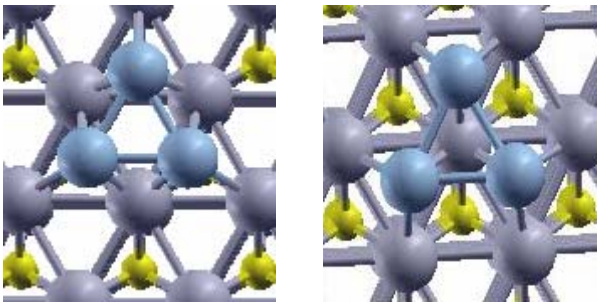

(a) (b)

Figure 4.6. Adsorption of Co_3 on MoC surface.

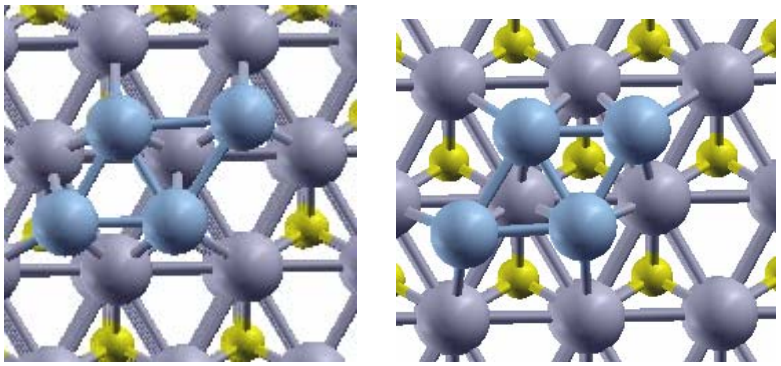

(a) (b)

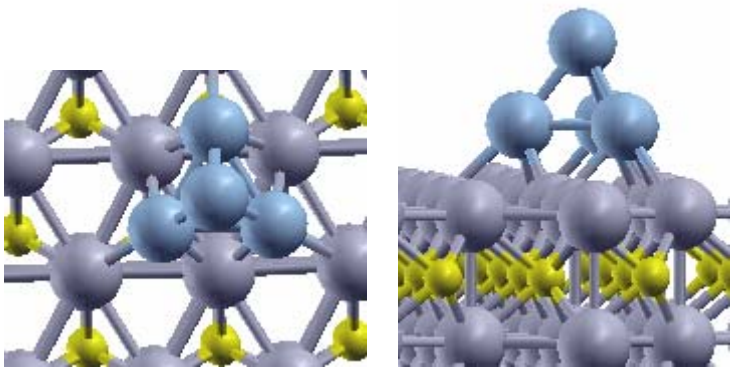

(c)

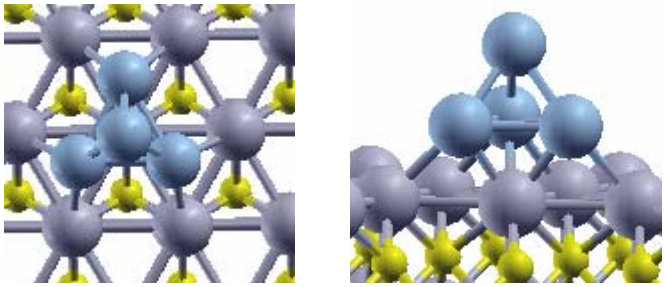

(d)

Figure 4.7. Adsorption of Co_4 on MoC surface. ((a): rhombus with all four Co atoms on hcp hollow sites, (b): rhombus with all four Co atoms on fcc hollow sites, (c): pyramid with three Co atoms on first layer adsorbed on hcp hollow sites, (d): pyramid with three Co atoms on first layer adsorbed on fcc hollow sites)

Four kinds of adsorbed Co_4 clusters are considered: one layered rhombus structure, with the four Co atoms adsorbed on 4 adjacent hcp hollow sites (Figure 4.7(a)) or with the four atoms adsorbed on adjacent fcc hollow sites (Figure 4.7(b)), and two layered pyramid structures with three Co atoms on the first layer adsorbed on hcp hollow sites or fcc hollow sites as shown in Figures 4.7 (c) and (d). It is found that the system has lower energy when the 4 cobalt atoms are in one layer compared to the case in two layers when the adsorption sites are the same for the first layer atoms (either all on fcc hollow positions or all on hcp hollow positions). While when the clusters have the same shape (both pyramid or both rhombus), the system has lower energy when all atoms in first layer are on hcp hollow positions. That is to say, among the four cases studied, the system with four Co atoms in one layer, occupying four hcp hollow positions in rhombus structure (Figure 4.7(a)) has the lowest energy.

Like Co_4 clusters, four cases are studied for Co_7 cluster adsorption (Figure 4.8) and similar result is found: when all seven Co atoms are in one layer, occupying seven adjacent hcp hollow positions (Figure 4.8(a)), the system has lowest energy.

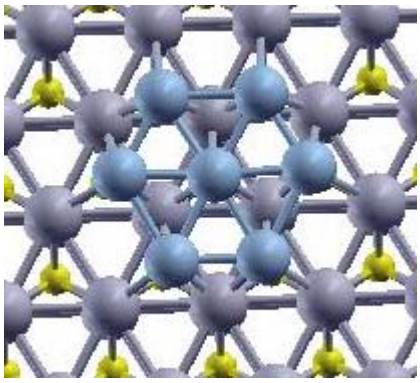

(a) all Co atoms on hcp hollow sites

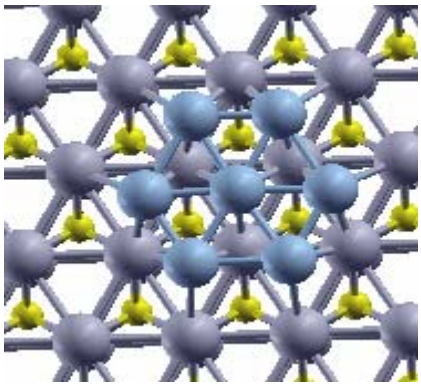

(b) all Co atoms on fcc hollow sites

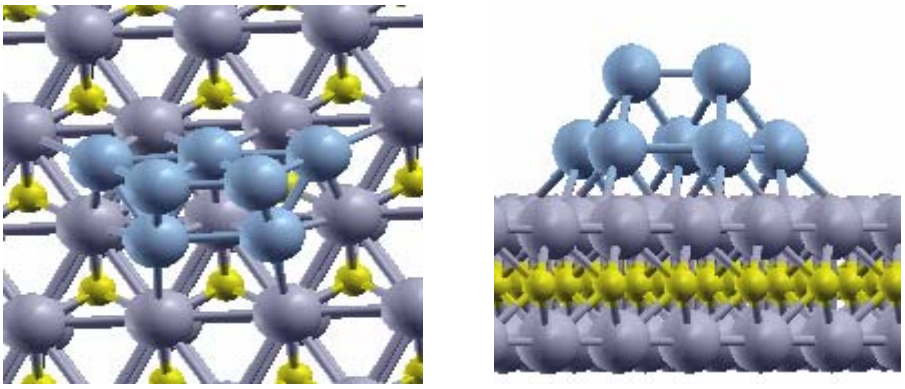

(c) 5 Co atoms on fcc hollow sites, 2 on second layer

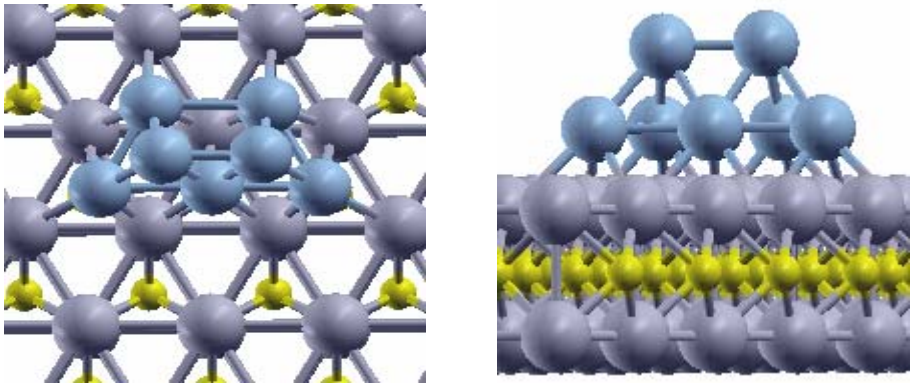

(d) 5 Co atoms on hcp hollow sites, 2 on second layer

Figure 4.8. Adsorption of Co_7 on MoC surface.

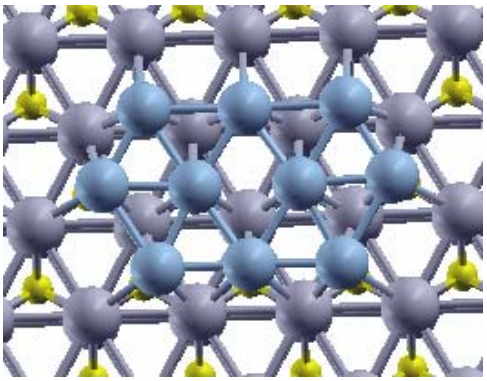

(a) all Co atoms on hcp hollow sites

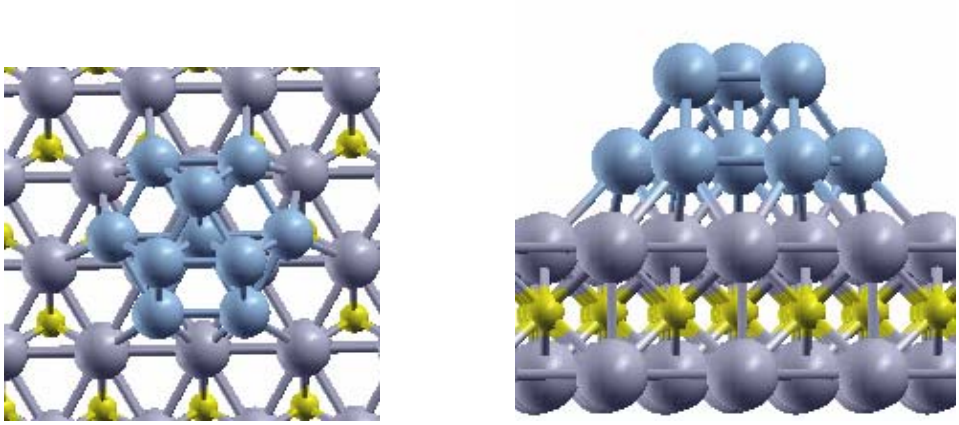

(b) 7 Co atoms on first layer hcp hollow sites, 3 on second layer top sites

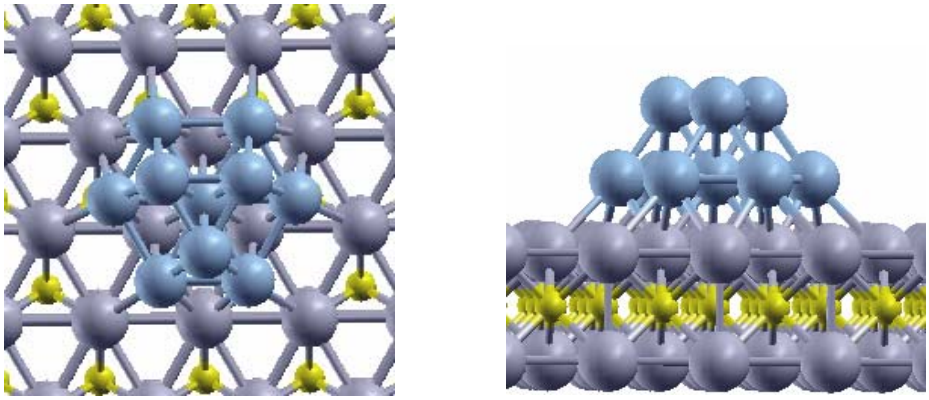

(c) 7 on hcp hollow sites, 3 on second layer, fcc hollow sites

Figure 4.9. Adsorption of Co_{10} on MoC surface.

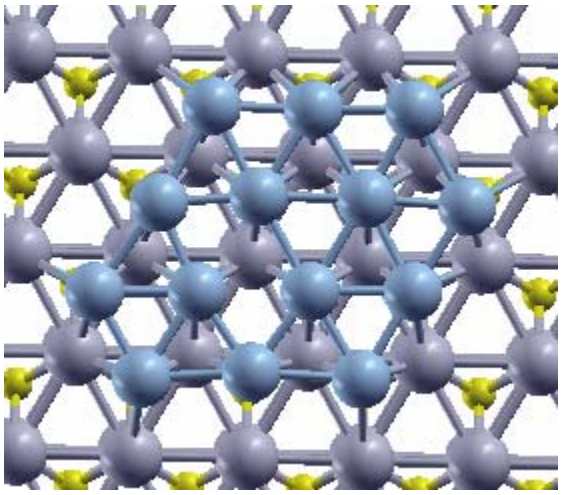

(a) all 14 Co atoms on hcp hollow sites

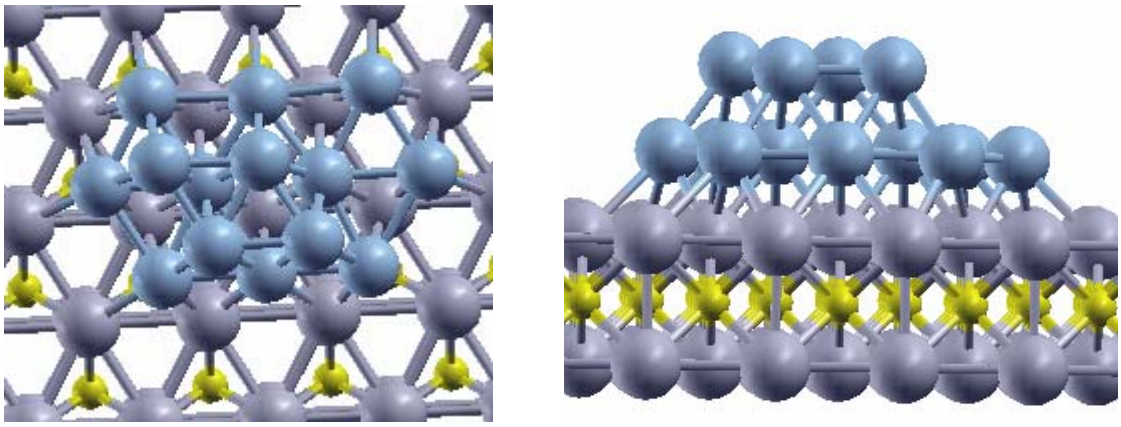

(b) 10 Co atoms on hcp hollow sites, 4 on second layer, fcc hollow sites

Figure 4.10. Adsorption of Co_{14} on MoC surface.

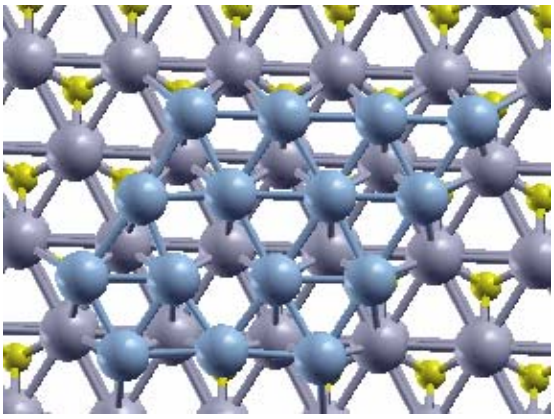

(a) all 14 Co atoms on hcp hollow sites

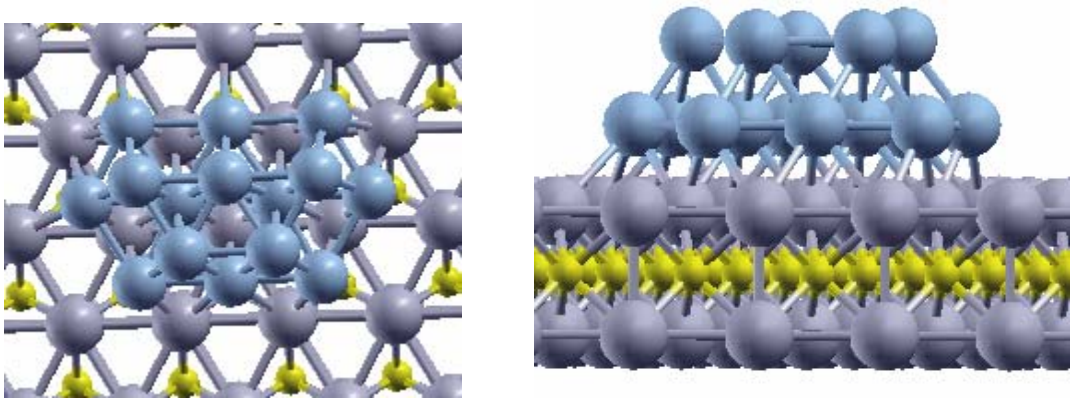

(b) 10 Co atoms on hcp hollow sites, 5 on second layer, fcc hollow sites

Figure 4.11. Adsorption of Co_{15} on MoC surface.

Up to now it is pretty clear that Co atoms tend to occupy hcp hollow sites. So to save time, for larger Co_N clusters (N=10, 14, 15), only the cases where Co atoms are adsorbed on hcp hollow sites with the Co atoms forming one or two layer structures as shown in Figures 4.9-4.11 are studied. For N=10, 14 and 15, same trend is observed: the system with all Co atoms in one layer has lower energy than those of in two layers.

Besides, for Co clusters with 10 Co atoms, two cases both having 7 Co atoms adsorbed on hcp hollow site of first layer are studied. In one of them, three Co atoms are adsorbed on top positions of second layer (Figure 4.9(b)) while in the other one these three Co atoms are adsorbed on fcc hollow positions of second layer (Figure 4.9(c)). Bond lengths of these two cases are nearly the same, and the energy difference of these two cases is quite small (0.02 eV).

Table 4.1: Optimized adsorption sites of Co_N (N=1-3) on MoC

cluster	site	E-E_0/ eV	E_{ads}/ eV	Co-Mo bond/ Å	Co-Co bond/ Å	Co-Co bond before adsorption/ Å
Co	fcc hollow site	0.487	-3.979	2.41		
	hcp hollow site	0	-4.466	2.40		
Co_2	Both on hcp hollow sites		-5.860	2.37~2.54	2.76	1.96
Co_3	All on hcp hollow sites	0	-8.286	2.42~2.71	2.45	2.11~2.18
	All on fcc hollow sites	1.106	-7.180	2.38~2.56	2.64~2.66	

From Table 4.1 it is obvious that for Co_N clusters (N=2, 3), the Co-Co bond length in adsorbed clusters are much longer than the corresponding bond lengths in the free cluster.

This is because Co atoms have lower energy when they are adsorbed on hcp hollow positions and the distance between adjacent hcp hollow positions is 2.92 Å, much larger than the Co-Co bond length in free clusters (1.9~2.2 Å), so the Co-Co bond length in adsorbed clusters are smaller than the distance between adjacent hcp hollow positions but larger than the bond length in the corresponding free clusters. For the same reason,

the Co-Co bond lengths in the first layer of the adsorbed cluster Co_N (N=4, 7, 10, 14, 15) are longer than the other Co-Co bonds. As shown Table 4.2, the Co-Co bond lengths between Co atoms in the first layer of adsorbed clusters Co_N (N=4, 7, 10, 14, 15) are much longer than those between Co atoms in the second layer or those between the first layer and second layer Co atoms.

As shown in Table 4.1, though the adsorption energy on hcp hollow site is much lower than that on fcc hollow site, the Co-Mo bond lengths are nearly the same (2.40 Å on hcp hollow site vs. 2.41 Å on fcc hollow site). For adsorption of Co_N clusters with N greater than 1, because of the mismatch of the Co-Co bond length with adjacent adsorption sites on the surface, the Co-Mo bonds length varies in a certain range. The bigger the cluster, the larger the variation range (from 2.37~2.54 Å for Co_2, to 2.38~2.86 Å for Co_7 , to 2.34~3.00 Å for Co_{15}). For clusters of the same number of Co atoms, N, those that form one layer shows larger variations in their bond lengths than those form two layers. But no general trend of the effect of the adsorption site (hcp hollow or fcc hollow) on the bond length is observed.

Table 4.2: Optimized adsorption geometries of Co_N (N=4, 7, 10, 14, 15) on MoC

cluster	geometry and adsorption position	E-E_0/ eV	cluster diameter /Å		Co-Mo bond length/ Å	first layer Co-Co bond length /Å	second layer Co-Co bond length / Å	Co-Co bond between first layer and second layer/ Å
			D1	D2				
Co_4	all on hcp hollow sites	0			2.35~2.74	2.44~2.77		
	3 co atoms on hcp hollow sites, 1 co atom on the second layer	1.569			2.42~2.72	2.44~2.46		2.28~2.31
	all on fcc hollow sites	0.836			2.43~2.84	2.38~2.59		
	3 co atoms on fcc hollow sites, 1 co atom on the second layer	2.706			2.38~2.62	2.55~2.56		2.34~2.36
Co_7	all on fcc hollow sites	1.083	4.99	4.99	2.38~2.86	2.36~2.63		
	5 on fcc hollow sites, 2 on second layer	3.053	4.35	2.53	2.38~2.87	2.33~2.66	2.27	2.29~2.45
	all on hcp hollow sites	0	5.15	5.12	2.31~2.80	2.40~2.72		
	5 on hcp hollow sites, 2 on second layer	1.907	4.51	2.48	2.36~2.76	2.44~2.76	2.34	2.29~2.47

Table 4.2: Continued

cluster	geometry and adsorption position	$E-E_0$/ eV	cluster diameter /Å		Co-Mo bond length/ Å	first layer Co-Co bond length /Å	second layer Co-Co bond length / Å	Co-Co bond between first layer and second layer/ Å
Co_{10}	all on hcp hollow sites	0	7.98	4.28	2.32~2.89	2.38~2.88		
	7 on hcp hollow sites, 3 on second layer, top sites	1.730	5.06	5.06	2.39~2.82	2.50~2.59	2.36	2.34~2.44
	7 on hcp hollow sites, 3 on second layer, fcc hollow sites	1.775	5.09	5.09	2.39~2.83	2.44~2.62	2.36~2.37	2.34~2.44
Co_{14}	all on hcp hollow sites	0	9.63	7.84	2.31~2.91	2.48~2.86		
	10 on hcp hollow sites, 4 on second layer, fcc hollow sites	1.954	7.90	4.27	2.36~2.92	2.41~2.75	2.33~2.44	2.36~2.49
Co_{15}	all on hcp hollow sites	0	11.83	7.78	2.34~3.00	2.43~2.87		
	10 on hcp hollow sites, 5 on second layer, fcc hollow sites	2.186	7.76	4.29	2.40~2.96	2.40~2.70	2.37~2.51	2.31~2.49

4.3 Conclusions

Adsorption of a series of Co_N clusters (N=1-4, 7, 10, 14, 15) on MoC surfaces are studied. Co atom can be adsorbed on hcp hollow position or fcc hollow position of the MoC surface with the adsorption energy on hcp hollow position being much lower than that on fcc hollow position. The adsorption energy of Co_N clusters on adjacent hcp hollow positions of the MoC surface is lower than that on fcc hollow positions. For Co_N clusters (N=4, 7, 10, 14, 15), the system has lower energy when all the Co atoms are adsorbed on the MoC surface, forming one layer compared to the case the Co atoms forming two-layer structures. In Co_2 and Co_3 clusters the Co-Co bond length between two adsorbed Co atoms are longer than that in corresponding free clusters. In two-layer clusters, the Co-Co bond lengths between the Co atoms in the first layer are longer than those between atoms in the second layer or between atoms in the first and second layer.

5. CONCLUSIONS AND RECOMMENDATIONS

5.1 Conclusions

The following conclusions are drawn from the above work and discussions:

- Under experimental conditions of the CoMoCAT synthesis method, the growth of SWCNTs follows a root growth according to the sequence: carbon atoms dissolve in the metal cluster and then precipitate on its surface, evolving into various carbon structures finally forming a cap which eventually grows to a single-wall nanotube.
- Nanotube (6, 5), the most abundant product of the CoMoCAT synthesis process is quite different from any other nanotube studied in this project in that its reaction energy of forming one more ring at the open end of one-end-closed nanotube does not change much with the tube length and the aromatic properties of these new formed rings at the open end remain the same despite the change of tube length, i.e., as the growth proceeds.
- Nanotubes with and without cap structure have quite different aromatic properties although specific structures of these caps do not have significant effects on tube aromatic properties.
- The growth process of SWCNTs can be affected by the interaction between the cluster and the substrate. When this interaction is strong, the shape of the cluster is more rigid and the amount of carbon that can be dissolved into the cluster will decrease. The interaction between Co atoms and MoC surface is so

strong that small Co Clusters have lower energy when they form one layered structures on MoC surface with all the Co atoms occupying adjacent hcp sites. The Co-Co bond lengths are longer than those in free Co clusters. However more calculations should be carried out to study how this performance could affect the growth process of SWCNTs.

5.2 Recommendations for further work

5.2.1 MD simulation of growth of SWCNTs on clusters attached to MoC surface

Experimental observations have shown that selective growth could be controlled by varying the type of substrate. We have already studied the effect of the strength of substrate/cluster interaction on the growth process of SWCNT by adjusting the weakness of a simple LJ potential. An accurate force field should be developed to describe the interaction between Co atoms and MoC substrate. MD calculations should be carried out with such force field.

5.2.2 Interaction between catalyst cluster and nanotube with different chiralities

So far we have studied properties of nanotube with different chirality, length and open end/close end structure and proposed that the selective growth mechanism could be related to differences in aromatic properties between nanotubes with different chiralities. To truly understand the selective growth mechanism, calculations should be done to study how the properties of these nanotubes could affect their interactions with a metal

catalyst cluster and what would be the resultant effect on the catalytic growth process of SWCNT.

REFERENCES

(1) Iijima, S. *Mat. Sci. and Eng. B- Sol. St. Mat. for Adv. Tech.* **1993**, *19*, 172.

(2) Bethune, D. S.; Kiang, C. H.; de Vries, M. S.; Gorman, G.; Savoy, R.; Vazquez, J.; Beyers, R. *Nature* **1993**, *363*, 605.

(3) Resasco, D. E.; Alvarez, W. E.; Pompeo, F.; Balzano, L.; Herrera, J. E.; Kitiyanan, B.; Borgna, A. *J. Nanoparticle Res.* **2002**, *4*, 131.

(4) Bachilo, S. M.; Balzano, L.; Herrera, J. E.; Pompeo, F.; Resasco, D. E.; Weisman, R. B. *J. Am. Chem. Soc.* **2003**, *125*, 11186.

(5) Zhang, L.; Balzano, L.; Resasco, D. E. *J. Phys. Chem. B* **2005**, *109*, 14375.

(6) Lolli, G.; Zhang, L.; Balzano, L.; Sakulchaicharoen, N.; Tan, Y.; Resasco Daniel, E. *J Phys Chem B* **2006**, *110*, 2108.

(7) Iijima, S.; Ichihashi, T. *Nature* **1993**, *363*, 603.

(8) Kroto, H. W. *Nature* **1987**, *329*, 529.

(9) Brinkmann, G.; Fowler, P. W.; Manolopoulos, D. E.; Palser, A. H. R. *Chem. Phys. Lett.* **1999**, *315*, 335.

(10) Brinkmann, G.; von Nathusius, U.; Palser, A. H. R. *Discrete Applied Mathematics* **2002**, *116*, 55.

(11) S. Reich, C. T., J. Maultzsch. *Carbon Nanotubes: Basic Concepts and Physical Properties*; Weinheim ; Cambridge : Wiley-VCH, 2004.

(12) Krishnan, A.; Dujardin, E.; Ebbesen, T. W.; Yianilos, P. N.; Treacy, M. M. J. *Physical Review B: Condensed Matter and Materials Physics* **1998**, *58*, 14013.

(13) Yakobson, B. I.; Brabec, C. J.; Bernholc, J. *Physical Review Letters* **1996**, *76*, 2511.

(14) Schleyer, P.; Marker, C. *J. Am. Chem. Soc.* **1996**, *118*, 6317.

(15) Chen, Z.; Wannere, C. S.; Corminboeuf, C.; Puchta, R.; Schleyer, P. V. *Chem. Rev.* **2005**, *105*, 3842.

(16) Ormsby, J. L.; King, B. T. *J. Org. Chem.* **2004**, *69*, 4287.

(17) Schleyer, P. v. R.; Jiao, H.; van Eikema Hommes, N. J. R.; Malkin, V. G.; Malkina, O. *J. Am. Chem. Soc.* **1997**, *119*, 12669.

(18) Schleyer, P. v. R.; Manoharan, M.; Wang, Z.-X.; Kiran, B.; Jiao, H.; Puchta, R.; van Eikema Hommes, N. J. R. *Org. Lett.* **2001**, *3*, 2465.

(19) Katritzky, A. R.; Jug, K.; Oniciu, D. C. *Chemical Reviews* **2001**, *101*, 1421.

(20) Stanger, A. *Journal of Organic Chemistry* **2006**, *71*, 883.

(21) Matsuo, Y.; Tahara, K.; Nakamura, E. *Org. Lett.* **2003**, *5*, 3181.

(22) VanLier, G.; Fowler, P. W.; DeProft, F.; Geerlings, P. *J. Phys. Chem. A* **2002**, *106*, 5128.

(23) Dresselhaus, M. S., Dresselhaus, G., Avouris, Phaedon *Carbon nanotubes : synthesis, structure, properties, and applications* Springer: Berlin ; New York 2001; Vol. 80.

(24) Wong, S. S.; Harper, J. D.; Lansbury, P. T., Jr.; Lieber, C. M. *J. Am. Chem. Soc.* **1998**, *120*, 603.

(25) Kong, J.; Franklin, N. R.; Zhou, C.; Chapline, M. G.; Peng, S.; Cho, K.; Dailt, H. *Science* **2000**, *287*, 622.

(26) Collins, P. G.; Avouris, P. *Scientific American* **2000**, *283*, 62.

(27) Tseng, Y.-C.; Xuan, P.; Javey, A.; Malloy, R.; Wang, Q.; Bokor, J.; Dai, H. *Nano Letters* **2004**, *4*, 123.

(28) Gabriel, J.-c. P. *Materials Research Society Symposium Proceedings* **2003**, *776*, 271.

(29) Dinadayalane, T. C.; Leszczynski, J. *Theoretical and Computational Chemistry* **2007**, *18*, 167.

(30) Iijima, S. *Nature* **1991**, *354*, 56.

(31) Guo, T.; Nikolaev, P.; Rinzler, A. G.; Tomanek, D.; Colbert, D. T.; Smalley, R. E. *Journal of Physical Chemistry* **1995**, *99*, 10694.

(32) Guo, T.; Nikolaev, P.; Thess, A.; Colbert, D. T.; Smalley, R. E. *Chemical Physics Letters* **1995**, *243*, 49.

(33) Cassell, A. M.; Franklin, N. R.; Tombler, T. W.; Chan, E. M.; Han, J.; Dai, H. *J. Am. Chem. Soc.* **1999**, *121*, 7975.

(34) Li, Y.; Kim, W.; Zhang, Y.; Rolandi, M.; Wang, D.; Dai, H. *J. Phys. Chem. B* **2001**, *105*, 11424.

(35) Vinciguerra, V.; Buonocore, F.; Panzera, G.; Occhipinti, L. *Nanotechnology* **2003**, *14*, 655.

(36) Andriotis, A. N.; Menon, M.; Froudakis, G. *Phys. Rev. Lett.* **2000**, *78*, 2393.

(37) Mann, D. J.; Halls, M. D.; Hase, W. L. *J. Phys. Chem. B* **2002**, *106*, 12418.

(38) Maruyama, S.; Shibuta, Y. *Mol. Cryst. Liq. Cryst.* **2002**, *387*, 311.

(39) Shibuta, Y.; Maruyama, S. *Physica B* **2002**, *323*, 187.

(40) Hernandez, E.; Ordejon, P.; Boustani, I.; Rubio, A.; Alonso, J. A. *J. Chem. Phys.* **2000**, *113*, 3814.

(41) Bolton, K.; Rosen, A. *Phys. Chem. Chem. Phys.* **2002**, *4*, 4481.

(42) Bernholc, J.; Rabec, C. B.; BuongiornoNardelli, M.; Maiti, A.; Roland, C.; Yakobson, B. I. *Appl. Phys. A* **1998**, *67*, 39.

(43) Roland, C.; Bernholc, J.; Brabec, C.; Nardelli, M. B.; Maiti, A. *Molecular Simulation* **2000**, *25*, 1.

(44) Charlier, J. C.; Blase, X.; Vita, A. D.; Car, R. *Appl. Phys. A* **1999**, *68*, 267.

(45) Erkoc, S.; Malcioglu, O. B. *Int. J. Mod. Phys. C* **2001**, *12*, 865.

(46) Maiti, A.; Brabec, C. J.; Roland, C.; Bernholc, J. *Physical Review B* **1995**, *52*, 14850.

(47) Yamaguchi, Y.; Maruyama, S. *Eur. Phys. J. D* **1999**, *9*, 385.

(48) Ding, F.; Bolton, K.; Rosen, A. *J. Phys. Chem. B* **2004**, *108*, 17369.

(49) Ding, F.; Rosen, A.; Bolton, K. *Chem. Phys. Lett.* **2004**, *393*, 309.

(50) Gavillet, J.; Loiseau, A.; Ducastelle, F.; Thair, S.; Bernier, P.; Stephan, O.; Thibault, J.; Charlier, J. C. *Carbon* **2002**, *40*, 1649.

(51) Fan, X.; Buczko, R.; Puretzky, A. A.; Geohegan, D. B.; Howe, J. Y.; Pantelides, S. T.; Pennycook, S. J. *Phys. Rev. Lett.* **2003**, *90*, Art. No. 145501.

(52) Alvarez, W. E.; Pompeo, F.; Herrera, J. E.; Balzano, L.; Resasco, D. E. *Chem. Mat.* **2002**, *14*, 1853.

(53) Hafner, J. H.; Bronikowski, M. J.; Azamian, B. R.; Nikolaev, P.; Rinzler, A. G.; Colbert, D. T.; Smith, K. A.; Smalley, R. E. *Chem. Phys. Lett.* **1998**, *296*, 195.

(54) Sutton, A. P.; Chen, J. *Phil. Mag. Lett.* **1990**, *61*, 139.

(55) Rafii-Tabar, H.; Sutton, A. P. *Phil. Mag. Lett.* **1991**, *63*, 217.

(56) Brenner, D. W. *Phys. Rev. B* **1990**, *42*, 9458.

(57) Brenner, D. W.; Shenderova, O. A.; Harrison, J. A.; Stuart, S.; Ni, B.; Sinnott, S. B. *J. Phys: Condens. Matter* **2002**, *14*, 783.

(58) Martinez-Limia, A.; Zhao, J.; Balbuena, P. B. *J. Molec. Modeling* **2007**, *13*, 595.

(59) Tersoff, J. *Phys. Rev. B* **1989**, *39*, 5566.

(60) Numakura, H.; Kashiwazaki, K.; Yokohama, H.; Koiwa, M. *J. Alloys and Compounds* **2000**, *310*, 344.

(61) Herrera, J. E.; Resasco, D. E. *J. Phys. Chem. B* **2003**, *107*, 3738.

(62) Allen, M. P.; Tildesley, D. J. *Computer Simulation of Liquids*; Oxford University Press: Oxford, 1990.

(63) Zhao, J.; Martinez-Limia, A.; Balbuena, P. B. *Nanotechnology* **2005**, *16*, S575.

(64) Huang, S.-P.; Balbuena, P. B. *Mol. Phys.* **2002**, *100*, 2165.

(65) Huang, S.-P.; Balbuena, P. B. *J. Phys. Chem. B* **2002**, *106*, 7225.

(66) Huang, S.-P.; Mainardi, D. S.; Balbuena, P. B. *Surf. Sci.* **2003**, *545*, 163.

(67) Lamas, E. J.; Balbuena, P. B. *J. Phys. Chem. B* **2003**, *107*, 11682.

(68) Gavillet, J.; Thibault, J.; Stephan, O.; Amara, H.; Loiseau, A.; Bichara, C.; Gaspard, J.-P.; Ducastelle, F. *J. Nanosci. Nanotech.* **2004**, *4*, 346.

(69) Moisala, A.; Nasibulin, A. G.; Kauppinen, E. I. *J. Phys. : Condens. Matter* **2003**, *15*, S3011.

(70) Kuznetsov, V. L.; Usol'tseva, A. N.; Butenko, Y. V. *Kinetics and Catalysis* **2003**, *44*, 726.

(71) Maruyama, S.; Yamaguchi, Y. *Chem. Phys. Lett.* **1998**, *286*, 343.

(72) Balbuena, P. B.; Zhao, J.; Huang, S.; Wang, Y.; Sakulchaicharoen, N.; Resasco, D. E. *Journal of Nanoscience and Nanotechnology* **2006**, *6*, 1247.

(73) Raty, J.; Gygi, F.; Galli, G. *Phys. Rev. Lett.* **2005**, *95*, 096103.

(74) Zhao, J.; Balbuena, P. B. *J. Phys. Chem. A* **2006**, *110*, 2771.

(75) Zhao, J.; Balbuena, P. B. *Journal of Physical Chemistry C* **2008**, *112*, 3482.

(76) Zhao, J.; Balbuena, P. B. *Journal of Physical Chemistry C* **2008**, *112*, 13175.

(77) Zurek, E.; Autschbach, J. *J. Am. Chem. Soc.* **2004**, *126*, 13079.

(78) Deng, W.-Q.; Xu, X.; Goddard, W. A., III. *Nano Letters* **2004**, *4*, 2331.

(79) Alekseev, N. I.; Dyuzhev, G. A. *Technical Physics* **2005**, *50*, 1504.

(80) Thaddeus B. Massalski, H. O., P.R. Subramanian, Linda Kacprzak *Binary Alloy Phase Diagrams*, 2nd ed.; ASM International: Materials Park, Ohio 1990.

(81) Kresse, G.; Hafner, J. *Physical Review B: Condensed Matter and Materials Physics* **1993**, *47*, 558.

(82) Kresse, G.; Hafner, J. *Physical Review B: Condensed Matter and Materials Physics* **1994**, *49*, 14251.

(83) Kresse, G.; Hafner, J. *Physical Review B: Condensed Matter and Materials Physics* **1993**, *48*, 13115.

(84) Kresse, G.; Furthmueller, J. *Physical Review B: Condensed Matter* **1996**, *54*, 11169.

(85) Kresse, G.; Furthmuller, J. *Computational Materials Science* **1996**, *6*, 15.

(86) Kresse, G.; Hafner, J. *Journal of Physics: Condensed Matter* **1994**, *6*, 8245.

(87) Perdew, J. P.; Burke, K.; Ernzerhof, M. *Physical Review Letters* **1996**, *77*, 3865.

VITA

Jin Zhao received her Bachelor of Science in chemical engineering from Tianjin University, Tianjin, China in 2000. She then continued her graduate study and received her Master of Science in chemical engineering at the same university in 2003.

In August 2003, she joined Dr. Balbuena's research group as a Ph.D. student in chemical engineering. Since then, she has worked in the area of computational simulations on material science. She received her Ph.D. in December 2008.

Ms. Zhao may be reached at 3122 TAMU, Department of Chemical Engineering, College Station, TX 77843. Her email address is jin.zhao@chemail.tamu.edu.